Sensitivity and Uncertainty Analysis of a Fixed Source Criticality Accident Alarm System Benchmark Experiment

A Dissertation presented for the
Doctor of Philosophy
Degree
The University of Tennessee, Knoxville

Kevin Howard Reynolds
May 2013

Dedication

This dissertation is dedicated to my loving wife Kimberly whose infinite patience has allowed me to pursue the completion of my life long dream of becoming Doctor Kevin Reynolds.

I also wish to dedicate this work to my parents who instilled in me the desire to learn and know all that I could at an early age.

Acknowledgements

I would first like to acknowledge Dr. Jerry McKamy and the DOE Nuclear Criticality Safety Program. Without the funding provided by Dr. McKamy and the Nuclear Criticality Safety Program these experiments would not have been conducted and the work in this dissertation would not have been possible.

I would also like to recognize Dr. Thomas Miller whose time and energy contributed to this effort were invaluable. Dr. Miller's patience and sense of humor made spending long hours of detail work seem like an adventure.

Dr. Laurence Miller has been my advisor and has also been my friend. His willingness to think outside the box allowed this research effort to come to fruition and I am forever thankful.

Finally, I would like to thank my employer, B&W Y-12 for their support of my graduate education. Their support via their Education Assistance Program and the granting of a full time research sabbatical have allowed me to finally achieve my goal of completing my PhD.

Abstract

The Department of Energy (DOE) Nuclear Criticality Safety Program (NCSP) funded the development of a criticality accident alarm system (CAAS) benchmark to be published by the International Criticality Safety Benchmark Evaluation Project (ICSBEP) in the International Handbook of Evaluated Criticality Safety Benchmark Experiments (handbook). While there are shielding related benchmark evaluations published in the handbook, the effort in this dissertation concerns a first of its kind experiment that has been conceived from the ground up as a pulsed critical fixed source benchmark.

The experiment was designed in conjunction with the French government and conducted at their SILENE reactor facility at the Commissariat a l Energie Atomique et aux Energies Alternatives (CEA) Valduc Laboratory. Oak Ridge National Laboratory (ORNL) was chosen as the lead organization for conducting and evaluating the experiment. This Doctoral research project (1) produced a High Fidelity 3-D computational model of pulse 1 from the experiment; (2) used this model to estimate neutron activation in foils and compare these results to measured activation, (3) used direct perturbation to reduce the complexity of the high fidelity model to an equivalent simplified model, and (4) used the simplified model to perform a sensitivity and uncertainty analysis of aspects of the computational model.

The computational code package chosen for this effort was the SCALE code package developed by ORNL. The new MAVRIC computational sequence was used to produce the computational estimates of neutron activation. The MAVRIC sequence uses new automated variance reduction techniques to accelerate the fixed source Monte Carlo calculation.

The high fidelity and simplified 3-D models both produced estimates of activation in good agreement with the experimental results. The ratio of computed to experimental (C/E) results ranged from 0.95 to 1.28. Computed sensitivity coefficients revealed that the model was most sensitive to the thickness of the activation foils. The MAVRIC sequence produced estimates of foil activation rates that were in excellent agreement with the measured activation. The overall uncertainty in the computed responses due to uncertainties in the input information was in all cases less than 10% and were the major driver of uncertainty in the final results.

Table of Contents

INTRODUCTION **1**

1. EXPERIMENTAL SETUP **6**
1.1 SILENE DESCRIPTION 6
1.2 RADIATION DETECTORS 8
1.3 SHIELDING MATERIALS 12
1.4 FINAL SETUP DESCRIPTION 18

2. THEORY **24**
2.1 FORWARD TRANSPORT EQUATION DERIVATION 24
2.2 ADJOINT TRANSPORT EQUATION DERIVATION 33
2.3 DETECTOR RESPONSES AND THE ADJOINT FLUX 39
2.4 CONSISTENT ADJOINT DRIVEN IMPORTANCE SAMPLING (CADIS) 41
2.5 FORWARD WEIGHTED CADIS (FW-CADIS) 44
2.6 SENSITIVITY AND UNCERTAINTY 47

3. COMPUTATIONAL TOOLS **49**

4. HIGH FIDELITY 3-D MODEL OF PULSE 1 ..... **54**
4.1 MODEL OVERVIEW 54
4.2 COMPONENT MODEL DESCRIPTIONS 55
4.3 COMPUTATIONAL MODEL MATERIALS 74
4.4 FINAL MODEL ASSEMBLY 89

5. RESULTS **91**
5.1 COMPARISON OF HIGH FIDELITY MODEL RESULTS TO FINAL DOSIMETRY 91
5.2 SIMPLIFICATION OF HIGH FIDELITY 3-D MODEL 96
5.3 SENSITIVITY COEFFICIENTS FOR SIMPLIFIED 3-D MODEL 104
5.4 SIMPLIFIED 3-D MODEL UNCERTAINTY 107
5.5 FINAL SUMMARY OF RESULTS 111

CONCLUSIONS AND FUTURE WORK **115**

WORKS CITED **117**

APPENDICES **120**
APPENDIX A 121
APPENDIX B 133
APPENDIX C 148

VITA **153**

List of Tables

TABLE 1: ACTIVATION FOIL NUCLEAR PROPERTIES 9
TABLE 2: ACTIVATION FOIL PHYSICAL CHARACTERISTICS 11
TABLE 3: LAYOUT OF PULSES 1-3 20
TABLE 4: ORIGINAL MATERIAL SPECIFICATION FOR REACTOR CELL CONCRETE 75
TABLE 5: BENCHMARK MATERIAL SPECIFICATION FOR REACTOR CELL CONCRETE 76
TABLE 6: ORIGINAL MATERIAL SPECIFICATION FOR S235JR STAINLESS STEEL 77
TABLE 7: BENCHMARK MATERIAL SPECIFICATION FOR S235JR STAINLESS STEEL 78
TABLE 8: ORIGINAL MATERIAL SPECIFICATION FOR Z3-CN-1810 STEEL 80
TABLE 9: BENCHMARK MATERIAL SPECIFICATION FOR Z3-CN-1810 STEEL 81
TABLE 10: BENCHMARK MATERIAL SPECIFICATION FOR A42 STEEL 82
TABLE 11: BENCHMARK MATERIAL SPECIFICATION FOR URANYL NITRATE FUEL 83
TABLE 12: BENCHMARK MATERIAL SPECIFICATION FOR LEAD 84
TABLE 13: BENCHMARK MATERIAL SPECIFICATION FOR PPB9 86
TABLE 14: ORIGINAL MATERIAL SPECIFICATION FOR AG3M ALUMINUM 87
TABLE 15: BENCHMARK MATERIAL SPECIFICATION FOR AG3M ALUMINUM 88
TABLE 16: PULSE ONE MEASURED DOSIMETRY RESULTS 92
TABLE 17: COMPARISON OF CALCULATED AND MEASURED RESULTS 93
TABLE 18: COMPARISON OF MEASURED GOLD FOIL RESULTS 95
TABLE 19: COMPARISON OF CALCULATED AND MEASURED THERMAL FOIL RESPONSES 99
TABLE 20: COMPARISON OF CALCULATED AND MEASURED THRESHOLD FOIL RESPONSES 102
TABLE 21: SENSITIVITY COEFFICIENTS FOR THERMAL FOIL REACTIONS 105
TABLE 22: BENCHMARK UNCERTAINTY VALUES FOR THERMAL FOIL REACTIONS 109
TABLE 23: FINAL RESULTS SUMMARY FOR ACTIVATION FOILS 113
TABLE 24: BENCHMARK MATERIAL SPECIFICATION FOR IRON FOIL 122
TABLE 25: BENCHMARK MATERIAL SPECIFICATION FOR MAGNESIUM FOIL 124
TABLE 26: BENCHMARK MATERIAL SPECIFICATION FOR COBALT FOIL 126
TABLE 27: BENCHMARK MATERIAL SPECIFICATION FOR NICKEL FOIL 128
TABLE 28: BENCHMARK MATERIAL SPECIFICATION FOR GOLD FOIL 130
TABLE 29: BENCHMARK MATERIAL SPECIFICATION FOR INDIUM FOIL 131
TABLE 30: GOLD FOIL THERMAL CALCULATED RESPONSE RESULTS 134
TABLE 31: IRON-56 THERMAL CALCULATED RESPONSE RESULTS 136
TABLE 32: COBALT FOIL THERMAL CALCULATED RESPONSE RESULTS 138
TABLE 33: INDIUM FOIL THERMAL CALCULATED RESPONSE RESULTS 140
TABLE 34: NICKEL FOIL THRESHOLD CALCULATED RESPONSE RESULTS 143
TABLE 35: IRON-54 FOIL THRESHOLD CALCULATED RESPONSE RESULTS 144
TABLE 36: IRON-56 FOIL THRESHOLD CALCULATED RESPONSE RESULTS 145
TABLE 37: MAGNESIUM FOIL THRESHOLD CALCULATED RESPONSE RESULTS 146
TABLE 38: INDIUM FOIL THRESHOLD CALCULATED RESPONSE RESULTS 147

List of Figures

FIGURE 1: SILENE REACTOR 7
FIGURE 2: COLLIMATOR BOX A (RIGHT) AND BOX B (LEFT) 13
FIGURE 3: TYPICAL CONCRETE SLAB 14
FIGURE 4: SCATTERING BOX 15
FIGURE 5: SILENE LEAD SHIELD 16
FIGURE 6: SILENE POLYETHYLENE SHIELD 17
FIGURE 7: BOROBOND SHIELDS 19
FIGURE 8: PULSE ONE LAYOUT 21
FIGURE 9: PULSE TWO LAYOUT 22
FIGURE 10: PULSE THREE LAYOUT 23
FIGURE 11: PHASE SPACE ELEMENT 26
FIGURE 12: PHASE SPACE ELEMENT NEUTRON BALANCE PICTORIAL REPRESENTATION 26
FIGURE 13: UNIT VECTORS FOR BTE DERIVATION 31
FIGURE 14: CSAS6 CONTROL MODULE SEQUENCE 51
FIGURE 15: MAVRIC CONTROL SEQUENCE 53
FIGURE 16: EXPERIMENTAL LAYOUT OF SILENE REACTOR CELL 56
FIGURE 17: TOP VIEW OF SILENE REACTOR CELL MODEL 58
FIGURE 18: SIDE VIEW OF SILENE REACTOR CELL MODEL (FROM REAR OF ROOM) 59
FIGURE 19: COMPUTATIONAL MODEL OF SILENE 60
FIGURE 20: 3-D VIEW OF COLLIMATOR BOX A MODEL 61
FIGURE 21: INTERIOR VIEW OF COLLIMATOR BOX A AND BOX B 62
FIGURE 22: COLLIMATOR BOX A MODEL 64
FIGURE 23: COLLIMATOR BOX B (PRIOR TO EXPERIMENT) 64
FIGURE 24: FRONT AND REAR VIEWS OF SCATTERING BOX 65
FIGURE 25: SCATTERING BOX MODEL FRONT AND REAR VIEWS 65
FIGURE 26: FREE FIELD STAND 66
FIGURE 27: CLOSE-UP VIEW OF ACTIVATION FOILS ON FREE FIELD STAND 67
FIGURE 28: DIAGNOSTIC STANDS A AND B 69
FIGURE 29: COMPUTATIONAL MODEL OF DIAGNOSTIC STANDS A AND B 70
FIGURE 30: ALUMINUM FRAME FOR ACTIVATION FOILS 71
FIGURE 31: CONCRETE SHIELD SLAB 72
FIGURE 32: ORNL TLD 73
FIGURE 33: Y-Z KENO-VI SOURCE TALLY PROFILE AT SILENE CENTER 90
FIGURE 34: COMPARISON OF CALCULATED THERMAL FOIL RESPONSES 100
FIGURE 35: COMPARISON OF CALCULATED THRESHOLD FOIL RESPONSES 103
FIGURE 36: FINAL C/E RATIO FOR ACTIVATION FOILS 114

Introduction

In the early 1990's the United States Department of Energy (DOE) recognized that as the number of facilities performing critical experiments had been declining for some time, having a central repository for data produced from past critical experiments was becoming more important. In 1992 the DOE established the Criticality Safety Benchmark Evaluation Project (CSBEP). (Briggs, 2012) The CSBEP was initially managed by the United States DOE at Idaho National Laboratory with input from experimentalists from around the DOE complex (Los Alamos National Laboratory, Lawrence Livermore National Laboratory, The Savannah River Site, Oak Ridge National Laboratory, the Y-12 National Security Complex and others). In 1994 the first international participants joined the CSBEP effort (United Kingdom, Japan, France, Hungary, and The Russian Federation) and it became the International Criticality Safety Benchmark Evaluation Project (ICSBEP) managed by the Organization for Economic Cooperation and Development (OECD) via the Nuclear Energy Agency's (NEA) Nuclear Science Committee. (Briggs, 2012)

The ICSBEP is essentially a knowledge preservation effort. Since there are fewer and fewer facilities performing critical experiments anywhere in the world the preservation of existing critical experiment data becomes paramount. The ICSBEP collects, peer reviews and publishes critical experiment data gathered from 20 different international partners. (Briggs, 2012)

The data contained in the handbook is intended to be used by criticality safety professionals to perform validations of the computational platforms used to perform nuclear criticality safety analyses such as the SCALE code package developed by Oak Ridge National Laboratory (ORNL) or the MCNP code package developed by Los Alamos National Laboratory (LANL). (Oak Ridge National Laboratory, June 2011), (X-5 Monte Carlo Team, 2/1/2008)

Currently the handbook contains 549 evaluations representing 4708 critical, near critical, subcritical, or k_∞ configurations, 24 criticality alarm placement configurations, and 200 other configurations that have been deemed important to criticality safety applications. (Briggs, 2012)

Volume VIII of the handbook contains the currently evaluated set of shielding/Criticality Accident Alarm System (CAAS) related benchmarks. There are 3 sets of evaluations identified as shielding related, there are 2 sets identified as labyrinth related, and there is 1 set identified as skyshine related. None of these benchmark evaluations were designed to provide criticality accident related shielding data. (Briggs, 2012)

The three evaluations described as shielding related were conducted in Russia in the 1980's. This set of three evaluated benchmarks were all created to measure the neutron and gamma spectrum emitted from a ^{252}Cf source either in air or when shielded by a lead or iron sphere of varying diameters. The dimensions of the spherical lead shields varied from a diameter of 20 cm to a diameter of 60 cm. The dimensions of the spherical iron shields varied from a diameter of 20 cm to a diameter of 70 cm. The measurements of the spectra were all conducted at a distance of 3 times the radius of the shield from the center of the experiment. (Briggs, 2012)

The two evaluations described as being labyrinth related were also conducted in Russia in the 1980's. These experiments were designed to measure the neutron flux at various points along a concrete labyrinth. The measurements were all done along the centerline of the hallway in the labyrinth. In most cases the measurements involved only concrete but in some of the cases evaluated there were plates of special materials present. These special materials were present as plates on the surface of the concrete walls (polyethylene, cadmium, and borated concrete) or as plates in the center of the hallway (polyethylene). (Briggs, 2012)

The one set of skyshine related benchmarks were derived from a set of experiments conducted in Russia in the late 1990's. These experiments were designed to map the neutron and gamma flux and dose rate at distances of up to 1500 meters away from a test reactor that was modified to be open to the atmosphere. The reactor was fueled with 90 percent enriched uranium carbide fuel assemblies surrounded by a zirconium hydride moderating region. The reactor was externally shielded by a blanket of graphite outside the reactor vessel and a region of beryllium inside the reactor vessel. (Briggs, 2012)

In examining the above described shielding benchmarks, none of them are designed to mimic the radiation field that would be expected to be present during a nuclear criticality accident. The skyshine and labyrinth experiments all use the spontaneous fission of ^{252}Cf to create a steady state radiation field. The skyshine experiment uses an experimental reactor to create its steady state radiation field. It is possible that a criticality accident may have a steady state radiation source over a portion of its lifetime but these sorts of accidents will usually involve fissile material in a liquid form and have a large thermal component to them. None of the aforementioned shielding evaluations could be considered similar to such an arrangement of materials. Further, most criticality accidents involving only dry fissile materials will occur as a single pulse which then terminates the accident and clearly none of these experiments are designed to reproduce such a source term.

In addition to none of the current benchmarks involving a source term similar to that seen in a criticality accident, none of the benchmarks were designed to determine if criticality accident alarm detector hardware would "see" an accident and to also map the radiation field "seen" by that hardware. In other words – the current benchmark evaluations were designed to map radiation fields after they had been altered in some way by shielding materials. None of the shielding benchmarks were designed to mimic the source term associated with a typical criticality accident nor were there any comparisons made of mapped values to measured values (CAAS detectors, activation foils, TLDs etc.)

In the shielding cases – the experiments were concerned with mapping a radiation field produced from a constant source that was then altered by a fairly thin layer of a single shielding material. The labyrinth cases were more complex in that they used a larger geometry and more materials but they were still only interested in mapping the open air radiation field after it was affected by these various materials. The skyshine experiments were similar in that they were only interested in mapping the radiation field scattered from open air at various distances from a steady state source.

In examining these benchmark evaluations, none of them can be said to be providing insight into situations that are related to the physics of a criticality accident. Because of this, in late 2009, the DOE Nuclear Criticality Safety Program (NCSP) decided to fund the design, conduct, and analysis of an experiment to produce a fixed source criticality accident related benchmark for publication in the handbook. (Miller & Reynolds, 2010 Criticality Accident Alarm System Benchmark Experiments at the CEA Valduc SILENE Facility, September 2011), (Miller & Reynolds, November 2011)

This experiment was designed to mimic the radiation field that would be seen from a criticality accident involving a single pulse of radiation. The experiment's main purpose was twofold – to determine if currently deployed criticality accident alarm system detectors would in fact detect the radiation from such a pulse under various bare and shielded conditions and to also map the radiation field precisely for the purposes of providing benchmark data for the nuclear criticality safety community. ORNL was selected as the lead agency to design the experiment, oversee its conduct and ultimately analyze and produce the experimental data as a fixed source benchmark for the handbook. (Miller & Reynolds, 2010 Criticality Accident Alarm System Benchmark Experiments at the CEA Valduc SILENE Facility, September 2011), (Miller & Reynolds, November 2011)

The experiments were conducted in October 2010 by DOE in cooperation with the French Commissariat a l Energie Atomique et aux Energies Alternatives (CEA) at the CEA Valduc SILENE facility. (Miller & Reynolds, 2010 Criticality Accident Alarm System Benchmark Experiments at the CEA Valduc SILENE Facility, September 2011), (Miller & Reynolds, November 2011) Three different pulses were conducted using various shielding materials, activation foil sets and detectors over the course of two weeks. During the experiments CAAS detectors were deployed to determine if they would function during the simulated accident conditions, Thermoluminescent Dosimeters (TLDs) were deployed to map the gamma radiation field and activation foils were deployed to map the neutron radiation field. The CEA Valduc staff provided measured dosimetry results for the TLDs and activation foils in pulse one to ORNL in 2011 and for the foils and TLDs from pulses two and three in 2012. (Chateauvieux & Piot, CAAS Test Dosimetry Report, Pulse 1, 6/16/2011) (Chateauvieux & Piot, CAAS Test Dosimetry Report, Pulse 2, 5/24/2012), (Chateauvieux & Piot, CAAS Test Dosimetry Report, Pulse 3, 5/31/2012)

In order to produce a benchmark for publication in the handbook, the experiment must be simulated using a nuclear simulation code capable of computing the reaction rates in the foils and the dose rates in the TLDs so that these computed reaction rates can then be compared with the measured reaction rates generated during the experiment. In the case of the work in this dissertation the SCALE code package from ORNL has been selected as the simulation code. (Oak Ridge National Laboratory, June 2011) There are many reasons for this selection but the primary reason is that the latest version of SCALE includes new automated variance reduction tools that will allow these experimental setups to be simulated and to obtain reasonable statistics with the final answers within a reasonable amount of computer time. (Oak Ridge National Laboratory, June 2011)

One of the first issues to be overcome in producing a benchmark quality evaluation in the case of a fixed source experiment is the size of the geometric model in the final simulation and being able to generate estimates with reasonable statistics. In the case of the experiments conducted at CEA Valduc, the reactor cell is 22 meters x 15 meters x 11.35 meters with SILENE being placed in the approximate center of the reactor cell and the experimental apparatus being spread radially from the reactor. (Piot, June 2011) The components associated with the experiment are large, complex in construction and spread over a large area. The code specification for the geometry in this instance can be overwhelming.

How do you choose what to model and what not to model and how do you choose the level of detail for that model as compared to the real piece of equipment? Some early investigations were performed to determine if it was possible to perform the simulations for this experiment using a 1-D discrete ordinates code. The thought was that given the external source that the responses in the foils could be computed with relative ease if the adjoint flux for the problem could be determined. Initially two codes were used to try and construct a 1-D model of the experiment – MCNP and XSDRN. (X-5 Monte Carlo Team, 2/1/2008), (Oak Ridge National Laboratory, June 2011)

The neutron activation in the foils was estimated using both MCNP and XSDRN models. (Oak Ridge National Laboratory, June 2011), (X-5 Monte Carlo Team, 2/1/2008) These two estimates of the response in the foils should have compared well with each other and the measured dosimetry if a 1-D model was able to adequately represent the experiment. The calculated responses obtained did not compare well with the measured dosimetry, and no corrections to the solid angle or leakage spectrum could be found to improve this comparison.

After failing to produce a reasonable computational model in 1-D it was decided that a high fidelity 3-D model had the best chance of producing estimates of the foil responses that would compare well with the measured dosimetry. A highly detailed (high fidelity) 3-D model of the experiment was generated using SCALE. (Oak Ridge National Laboratory, June 2011) The SCALE General Geometry Package (SGGP) was used to specify the problem geometry, the Material Information Processor Library (MIPLIB) was used to specify the problem materials. The CSAS6 sequence was used to estimate the source term from each pulse. The MAVRIC sequence was used to produce the final estimates of response in the activation foils. (Oak Ridge National Laboratory, June 2011) The SCALE code package and the computational modules used for this dissertation are discussed in more detail in Chapter 3.

Once the complete high fidelity 3-D model of the experiment had been constructed and produced results that agreed with the measurement dosimetry it was tested to determine which portions of the model were in fact contributing to the calculated estimates of response in the foils. If a particular portion of the high fidelity model was determined not to be contributing to the final estimate of response then it was removed from the model. This series of direct perturbations resulted in a simplified 3-D model of the experiment, which was then used to perform the sensitivity and uncertainty analysis of pulse 1.

The work in this dissertation advances the state of the art in shielding analysis associated with nuclear criticality safety. The large majority of the benchmarks currently contained in the handbook provide experimental data on the effective multiplication of fissile systems (549 evaluations out of a total of 555). This is the first time that an experiment has been designed, constructed and performed with the intent of constructing a fixed source benchmark model to be published for the broader nuclear safety community. None of the existing shielding benchmarks in the handbook have source terms that are representative of a nuclear criticality accident. None of the existing shielding benchmarks in the handbook use activation foils or TLDs to produce measured dosimetry for the radiation field involved in their respective benchmarks.

Second, while there are new experiments being conducted at a limited number of facilities around the world today none of those experimental efforts are designed to validate fixed source computational sequences. There are a variety of reasons for this lack of new data but mostly it has been due to the fact that the computational tools have not been sophisticated enough to produce statistically reasonable answers with reasonable run times. Obtaining computational results with reasonable accuracy and reasonable statistical uncertainties for experiments of this size has been near impossible before this effort without resorting to special versions of the code designed to run on large supercomputers in a parallel computing environment. This sort of computational power is generally not available to the nuclear safety practitioner. The work supporting this dissertation utilizes newly developed variance reduction techniques in the newly released version of SCALE to arrive at estimates of reaction rates in the activated foils. The size and complexity of this problem was such that previous versions of SCALE were simply not capable of running long enough to sample enough particles in the all the right locations to generate statistically reasonable answers. Finally, this work takes newly developed computational tools and ideas and extends them to provide insight and answers previously unavailable.

The reminder of this dissertation is laid out as follows: Chapter 1 discusses the experimental setup, Chapter 2 details some of the theory underlying the analysis performed, Chapter 3 describes the computational tools used in this dissertation, Chapter 4 discusses the development of the high fidelity 3-D model, Chapter 5 discusses the direct perturbation analysis performed to simplify the high fidelity 3-D model, compares the computational results to the measured dosimetry, and presents the sensitivity and uncertainty analysis performed on the simplified computational model. The final section provides some concluding remarks and suggestions for future work.

1. Experimental Setup

The experiments conducted were three different pulses of the SILENE reactor with various foils, detectors, and shields deployed. The following sections describe the reactor, the equipment deployed, and the final configuration of each pulse.

1.1 SILENE Description

SILENE is a liquid fueled experimental reactor located at the CEA Valduc Laboratory. It is a compact annular tank with an outer diameter of 36 cm and an inner diameter of 7 cm sitting atop a stand which places the fueled region of the reactor approximately 100 cm above the floor (see Figure 1). The fuel for SILENE is prepared in a laboratory located in the basement of the facility and pumped into the reactor when ready for use. The reactor is located approximately in the center of a large concrete room (also referred to as the reactor "cell"). (Piot, June 2011), (Barbry F. Y., 1993), (Barbry, Fouillaud, & Verrey, 1999)

The reactor can be run bare or shielded. The installed shields consist of either lead or polyethylene and are constructed to be tight fitting around the outside of the reactor. SILENE can be run in steady-state mode, free evolution mode, or pulse mode. (Barbry F. Y., 1993)

Free Evolution operation of the reactor is achieved by slowly removing the central cadmium control rod (speeds less than 2 cm/sec) and having an external source present. Excess reactivity in this mode usually does not exceed 4.0 dollars but may be as high as 7.0 dollars when conducting solution boiling experiments. This mode of operation is designed to emulate accidental criticality excursions. (Barbry F. Y., 1993)

Steady state operation of the reactor involves automatic control of the position of the cadmium rod with small displacement rates of approximately 2mm/sec in order to maintain the reactor at a pre-determined steady state power level. (Barbry F. Y., 1993)

Operation of the reactor in pulse mode is obtained by rapidly removing the cadmium control rod at speeds of 0.2 m/sec (no external source) or 2 m/sec (with external source). Peak powers obtained are approximately 1000 MW in a few milliseconds. Excess reactivity is limited to 3.0 dollars in this mode of operation. (Barbry F. Y., 1993)



Figure 1: SILENE Reactor

The experiments being analyzed in this dissertation operated SILENE in pulse mode. In general the reactor is operated as follows:

- The fissile solution of uranyl nitrate (93% enriched) is pumped into the core to a pre-determined supercritical height. A cadmium control rod is present in the center of the core to maintain sub-criticality during this phase.
- The power excursion (or pulse) is produced by rapidly ejecting the control rod at a speed of 0.2 m/sec (with no additional source) or 2.0 m/sec (with an additional source).
- Once the pulse is complete, typically after 5 – 10 seconds, the fissile solution containing the radioactive fission products is pumped to a dump tank located in a shielded room so as to allow quick access to the reactor cell. (Miller & Reynolds, 2010 Criticality Accident Alarm System Benchmark Experiments at the CEA Valduc SILENE Facility, September 2011), (Miller & Reynolds, November 2011), (Barbry F. Y., 1993)

1.2 Radiation Detectors

Several different types of detectors were deployed for these experiments in order to measure neutron activation, neutron dose rate, photon dose, photon dose rate, neutron spectrum, and photon spectrum. These detectors were deployed both inside the reactor cell and outside the reactor cell. The detectors used in the performance of the experiment were: (Piot, June 2011)

- Neutron activation foils
- Thermoluminescent detectors (TLDs)
- CAAS detectors
- Liquid scintillators

The benchmark evaluation for these experiments will only use the data from the TLDs and the neutron activation foils.

1.2.1. Neutron Activation Foils

The neutron activation foils selected for the experiment were chosen by the experimental staff at the SILENE facility. The foils chosen produce a mixture of activation products sensitive to low energy neutrons and activation products with "high" threshold energies. A list of the activation foils used is provided in Table 1. The foils were arranged in several different configurations around SILENE during each pulse: (Piot, June 2011)

- Free Field location (1 set of foils)
- Scattering box location (4 sets of foils)
- Collimator Box A, unshielded front (1 set of foils)
- Collimator Box B, shielded front (1 set of foils).

Table 1: Activation Foil Nuclear Properties

Foil	Reaction	Threshold Energy [keV]	Reaction product Half-Life	Gamma Ray Energy [keV]	Probability of Emission
Cobalt	$^{59}Co(n,\gamma)^{60}Co$	< 1.0	5.3 years	1173.20	99.85%
				1332.50	99.98%
Gold	$^{197}Au(n,\gamma)^{198}Au$	< 0.01	2.70 days	411.80	95.24%
Indium	$^{115}In(n,\gamma)^{116}In$	< 0.01	54.0 minutes	416.86	27.70%
				1097.30	56.20%
				1293.54	84.40%
Indium	$^{115}In(n,n',\gamma)^{115m}In$	320	4.50 hours	336.2	45.80%
Iron	$^{54}Fe(n,p)^{54}Mn$	853	312.5 days	834.80	99.97%
Iron	$^{56}Fe(n,p)^{56}Mn$	2913	2.60 hours	846.80	98.85%
				1810.70	26.90%
Magnesium	$^{24}Mg(n,p)^{24}Na$	4732	15.0 hours	1368.60	99.99%
Nickel	$^{58}Ni(n,p)^{58}Co$	402	70.8 days	810.80	99.45%

The location of the foils was consistent between all pulses. Table 2 describes some of the important physical characteristics of the foils and their locations for Pulse 1.

1.2.2. Thermoluminescent detectors (TLDs)

Three different types of TLDs were used during the experiments to measure photon doses. The first TLD was provided by CEA Valduc and used an Al_2O_3 powder inside a capsule of Aluminum. The second TLD was provided by ORNL and used a LiF powder, which was material TLD-700 (ORNL HBG TLD). (McMahan, April 2010) The third TLD was also provided by ORNL and also used a LiF powder but was material TLD-707H as the activator (ORNL DXT TLD). (McMahan, April 2010) A set of all three TLDs was placed inside each of the collimator boxes next to the neutron activation foils. A third set of all three TLDs was placed at the free field location adjacent to the neutron activation foils. Two more sets of all three TLDs and two additional CEA TLDs were used inside the scattering box. Finally, two sets of ORNL TLDs were used just outside the reactor cell. (Piot, June 2011), (Miller & Reynolds, 2010 Criticality Accident Alarm System Benchmark Experiments at the CEA Valduc SILENE Facility, September 2011), (Miller & Reynolds, November 2011)

1.2.3. CAAS detectors

Two different CAAS systems were used during the experiments. The first type was a modern Criticality Incident Detection and Alarm System (CIDAS) provided by Babcock International Group. (Hunter, August 2010), (Bellamy & Cooper, 2005) This system is currently deployed at the Y-12 National Security Complex (Y-12 NSC) in the newly Highly Enriched Uranium Materials Facility (HEUMF). The CIDAS system uses a Geiger-Meuller tube to measure photon dose and dose rate. The CIDAS system will alarm if 280 nGy is detected in less than 1 second or if the dose rate exceeds 1 mGy/hr for more than 1 second. Lawrence Livermore National Laboratory (LLNL) provided the second type of CAAS used during the experiments. These units had previously been in use at the Rocky Flats Plant (RFP, now decommissioned) in Denver, Colorado. (Kim & Heinrichs, June 2009) The RFP CAAS units use a ^{6}LiF disc to absorb neutrons adjacent to a silicon detector, which counts the charged particles released by the neutron absorption events. The RFP CAAS will alarm when the detected neutron flux exceeds 500 n/cm^2. (Piot, June 2011), (Miller & Reynolds, 2010 Criticality Accident Alarm System Benchmark Experiments at the CEA Valduc SILENE Facility, September 2011), (Miller & Reynolds, November 2011)

1.2.4. Liquid scintillators

The final type of radiation detector used was a pair of liquid scintillators, which were placed outside the primary reactor cell behind a set of lead shields to prevent detector saturation. They were BICRON BC-510A liquid scintillators and were right circular cylinders with dimensions of 1" diameter x 1" height and 2" diameter x 2" height. (Piot, June 2011), (Miller & Reynolds, 2010 Criticality Accident Alarm System Benchmark Experiments at the CEA Valduc SILENE Facility, September 2011), (Miller & Reynolds, November 2011)

Table 2: Activation Foil Physical Characteristics

Pulse 1	Reference Foil	Thickness[a] [mm]	Diameter[b] [mm]	Mass [g±0.2%]	Purity
Collimator Box A	Au05–A10	0.25	20	1.547	99.997%
	Ni011	2	20	5.808	99.68%
	In005	1	20	2.328	99.96%
	Fe021	3	20	7.286	99.58%
	Mg032	2	20	1.091	99.93%
	Co013	2	20	5.813	99.95%
Collimator Box B	Au08–A10	0.25	20	1.537	99.997%
	Ni029	2	20	5.769	99.68%
	In006	1	20	2.333	99.96%
	Fe029	3	20	7.294	99.58%
	Mg030	2	20	1.084	99.93%
	Co019	2	20	5.816	99.95%
Free Field	Au09–A10	0.25	20	1.543	99.997%
	Ni016	1	20	2.807	99.69%
	In008	1	20	2.335	99.96%
	Fe028	3	20	7.292	99.58%
	Mg029	2	20	1.089	99.93%
	Co016	2	20	5.813	99.95%
Scattering Box Location1 (SB1)	Au001	0.25	20	1.584	99.999%
	Ni018	2	20	5.754	99.68%
	In09-A10	1	20	2.448	99.999%
	Fe020	3	20	7.279	99.58%
	Mg006	2	20	1.082	99.93%
	Co023	2	20	5.807	99.95%
Scattering Box Location 2 (SB2)	Au07-A10	0.25	20	1.545	99.997%
	Ni013	2	20	5.788	99.68%
	Co026	2	20	5.810	99.95%
Scattering Box Location 3 (SB3)	Au10-A10	0.25	20	1.557	99.997%
	Ni015	2	20	5.801	99.68%
	Co022	2	20	5.814	99.95%
Scattering Box Location 4 (SB4)	Au03-A10	0.25	20	1.558	99.997%
	Ni024	2	20	5.780	99.68%
	Co009	2	20	5.791	99.95%

[a] All foils have 10% uncertainty on thickness.
[b] Foils with A10 in the name have an uncertainty on diameter of ±0.2mm, all others have an uncertainty on diameter of ±0.5mm.

1.3 Shielding Materials

Several different shields were used during the conduct of the experiments. Some of these were built into the collimator boxes, some of these were deployed in contact with the reactor, while others were slabs of material used in both the scattering box and in front of the collimator boxes. (Piot, June 2011), (Miller & Reynolds, 2010 Criticality Accident Alarm System Benchmark Experiments at the CEA Valduc SILENE Facility, September 2011), (Miller & Reynolds, November 2011)

1.3.1 Collimator Boxes

The collimator boxes (Box A and Box B) are boxes open only on a single side whose purpose is to absorb scattered radiation from the room before it reaches the detectors deployed inside the boxes. The walls of the boxes consist of stainless steel, copper, lead and a mixture called PPB9 which is a borated plaster created by adding colemanite, polyethylene beads and gypsum together to form a borated plaster. (Piot, June 2011) A photo of the two collimator boxes is shown in Figure 2.

1.3.2. Concrete Slabs

Several different slabs of concrete were used to construct both the scattering box and to shield the front face of Collimator Box B. The concrete slabs were standard concrete, barite concrete, or magnetite concrete. Each of the slabs is 1m x 1m x 20 cm. All of the slabs were created by CEA Saclay for previous work conducted at the SILENE facility. A photo of a single concrete slab is shown in Figure 3. The scattering box was constructed of two slabs of magnetite concrete (S1 and S2) and four slabs of standard concrete (S3 – S6). (Piot, June 2011) A photo of the scattering box as constructed for these experiments is shown in Figure 4.

1.3.3. Reactor Shields

Two shields have been constructed to fit flush around the SILENE reactor for previous experimental setups. Both of these shields were used during the conduct of these experiments. The first shield is constructed of lead (painted orange) and forms an annulus tight around SILENE by moving its two halves along tracks in the floor. The second shield is polyethylene and is also formed to fit flush around the reactor from two halves pushed together. (Piot, June 2011) Photos of the lead shield are included in Figure 5. The left view is of ½ of the shield prior to being installed. The right view is of the entire lead shield installed. Figure 6 contains views of the Polyethylene shield in its installed configuration (left view) and of ½ the shield prior to installation (right view).



Figure 2: Collimator Box A (right) and Box B (left)

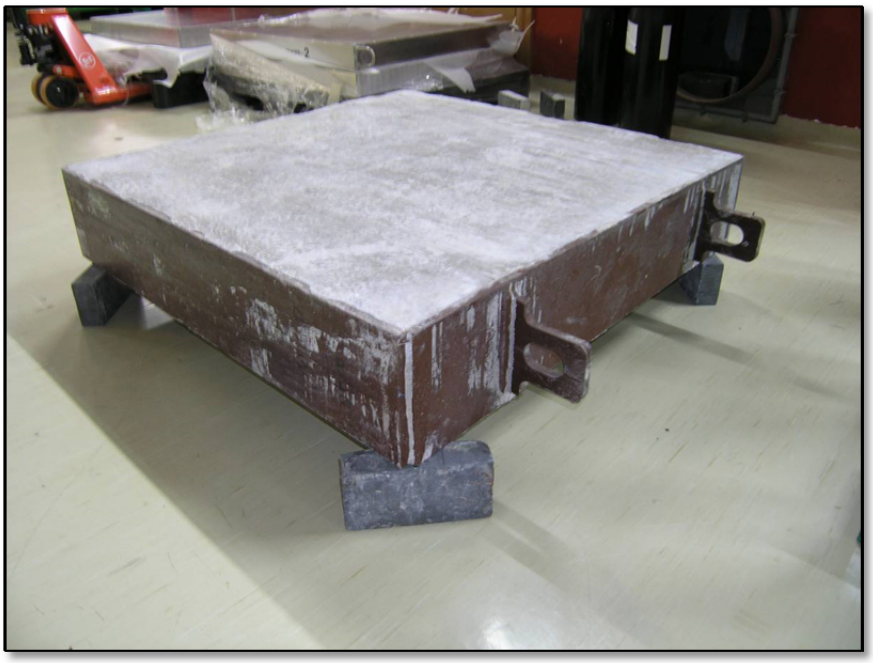


Figure 3: Typical Concrete Slab



Figure 4: Scattering Box



Figure 5: SILENE Lead Shield



Figure 6: SILENE Polyethylene Shield

1.3.4. Borobond

The final shield material is a specialty material provided by the Y-12 NSC. Borobond is a borated ceramic concrete material used in the HEUMF. Six slabs of borobond were manufactured in the United States by Ceradyne, Inc. and shipped to the SILENE facility for use in these experiments - Three slabs, which were 1m x 1m x 0.0254m thick, and three slabs that were 1m x 1m x 0.0508m thick. (Piot, June 2011) Figure 7 shows a view of one of the 0.0508cm thick borobond shields. One of the 0.0254cm thick borobond shields can also be seen in the background of the photo.

1.4 Final Setup Description

Each pulse of SILENE used a slightly different collection of shields in an effort to gather a broad spectrum of data for use in the ultimate verification and validation efforts for which this data is being collected. A brief description of the layout of each pulse is given in Table 3. (Piot, June 2011) Also, a pictorial layout of each pulse is included in Figures 8 through 10. (Piot, June 2011)

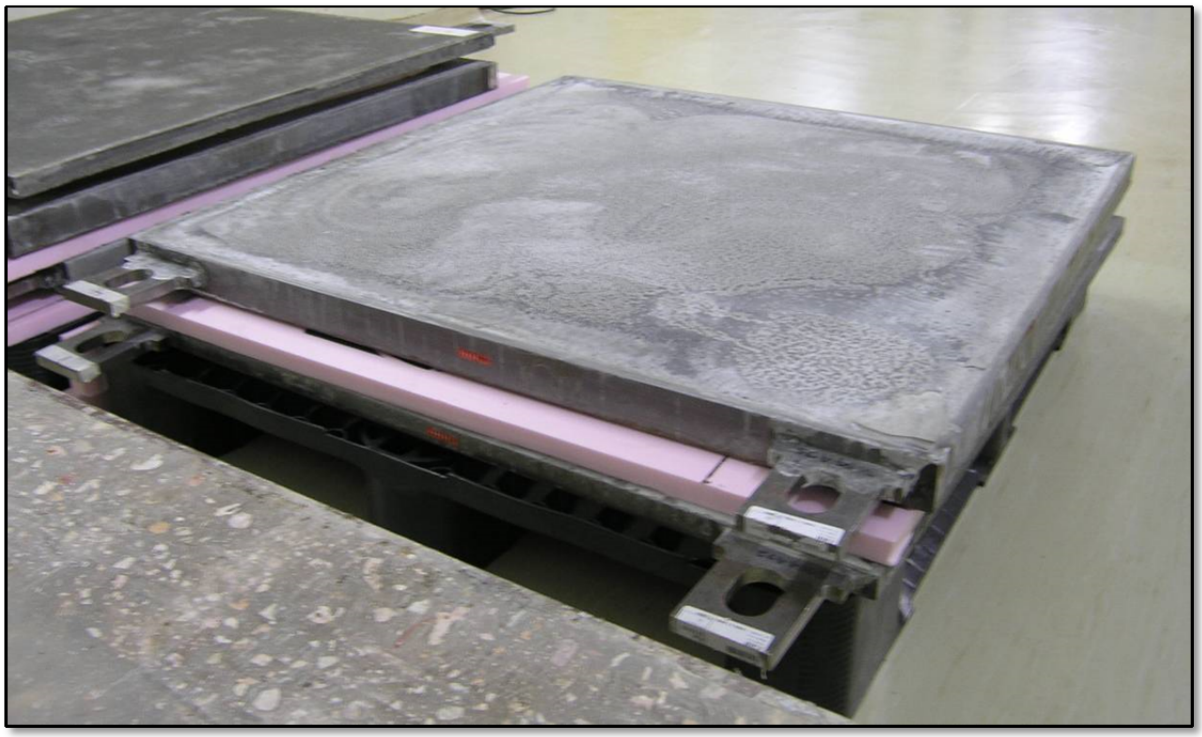


Figure 7: Borobond Shields

Table 3: Layout of Pulses 1-3

Pulse	SILENE	Collimator A	Collimator B	Free Field	Scattering Box
1	• Unshielded • No reflector	• Unshielded • Full Set of activation foils • One each of the three types of TLDs • One Rocky Flats CAAS	• 20cm Barite Concrete Shield • Full Set of activation foils • One each of the three types of TLDs • One Rocky Flats CAAS • One CIDAS CAAS	• Full Set of Activation foils • One each of the three types of TLDs	• Two 20cm magnetite concrete shields • Four 20cm Standard concrete shields • Full Set of Activation foils • Three partial sets of activation foils (Gold, Cobalt, Nickel) • Two of each ORNL TLD • Four VALDUC TLDs • One Rocky Flats CAAS • One CIDAS CAAS
2	• LEAD shielded	• Unshielded • Full Set of activation foils • One each of the three types of TLDs • One Rocky Flats CAAS	• 20cm Standard Concrete Shield • Full Set of activation foils • One each of the three types of TLDs • One Rocky Flats CAAS • One CIDAS CAAS	• Full Set of Activation foils • One each of the three types of TLDs	• Two 20cm magnetite concrete shields • Four 20cm Standard concrete shields • Full Set of Activation foils • Three partial sets of activation foils (Gold, Cobalt, Nickel) • Two of each ORNL TLD • Four VALDUC TLDs • One Rocky Flats CAAS • One CIDAS CAAS
3	• Polyethylene shielded	• Unshielded • Full Set of activation foils • One each of the three types of TLDs One Rocky Flats CAAS	• 7.62 cm Borobond Shield • Full Set of activation foils • One each of the three types of TLDs • One Rocky Flats CAAS • One CIDAS CAAS	• Full Set of Activation foils • One each of the three types of TLDs	• Two 20cm magnetite concrete shields • Four 20cm Standard concrete shields • Full Set of Activation foils • Three partial sets of activation foils (Gold, Cobalt, Nickel) • Two of each ORNL TLD • Four VALDUC TLDs • One Rocky Flats CAAS • One CIDAS CAAS

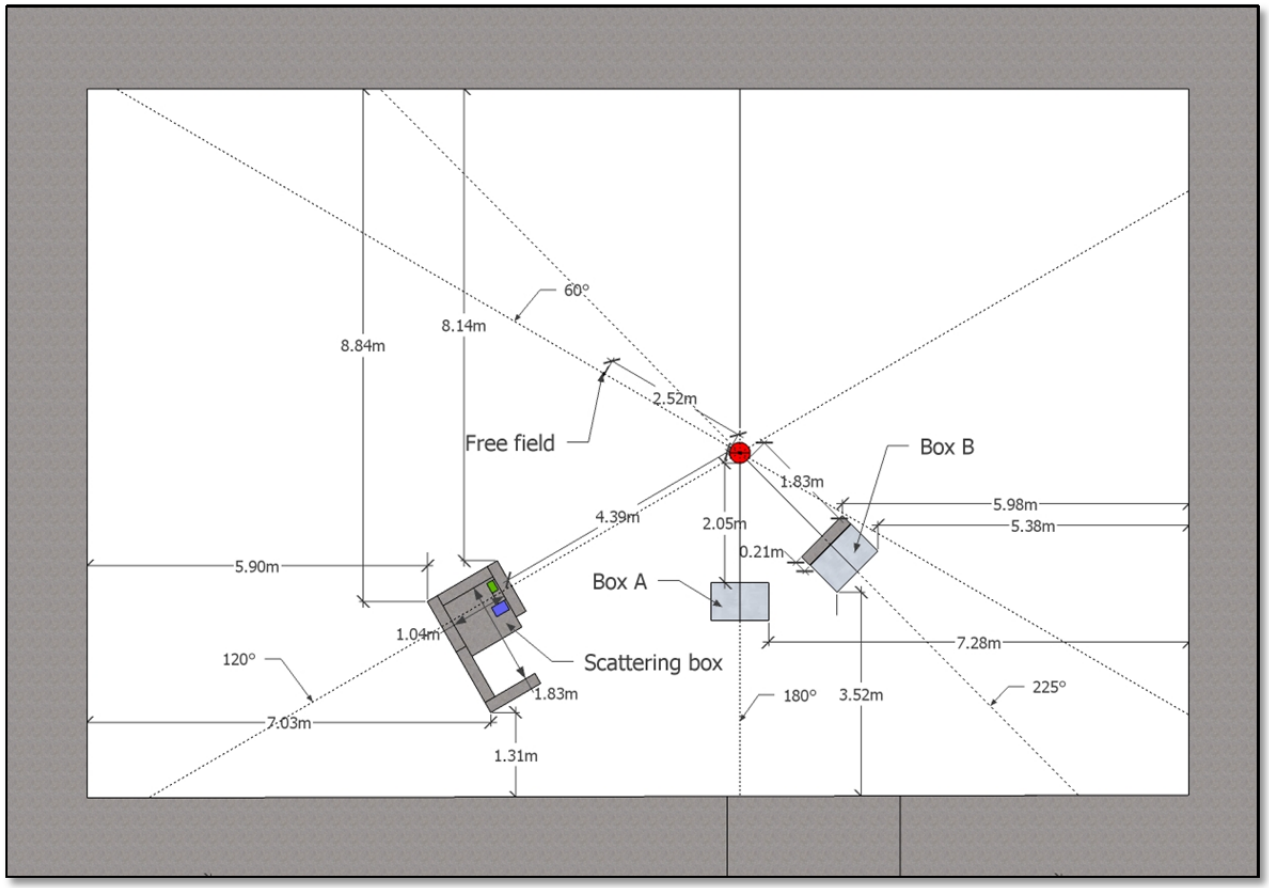


Figure 8: Pulse One Layout

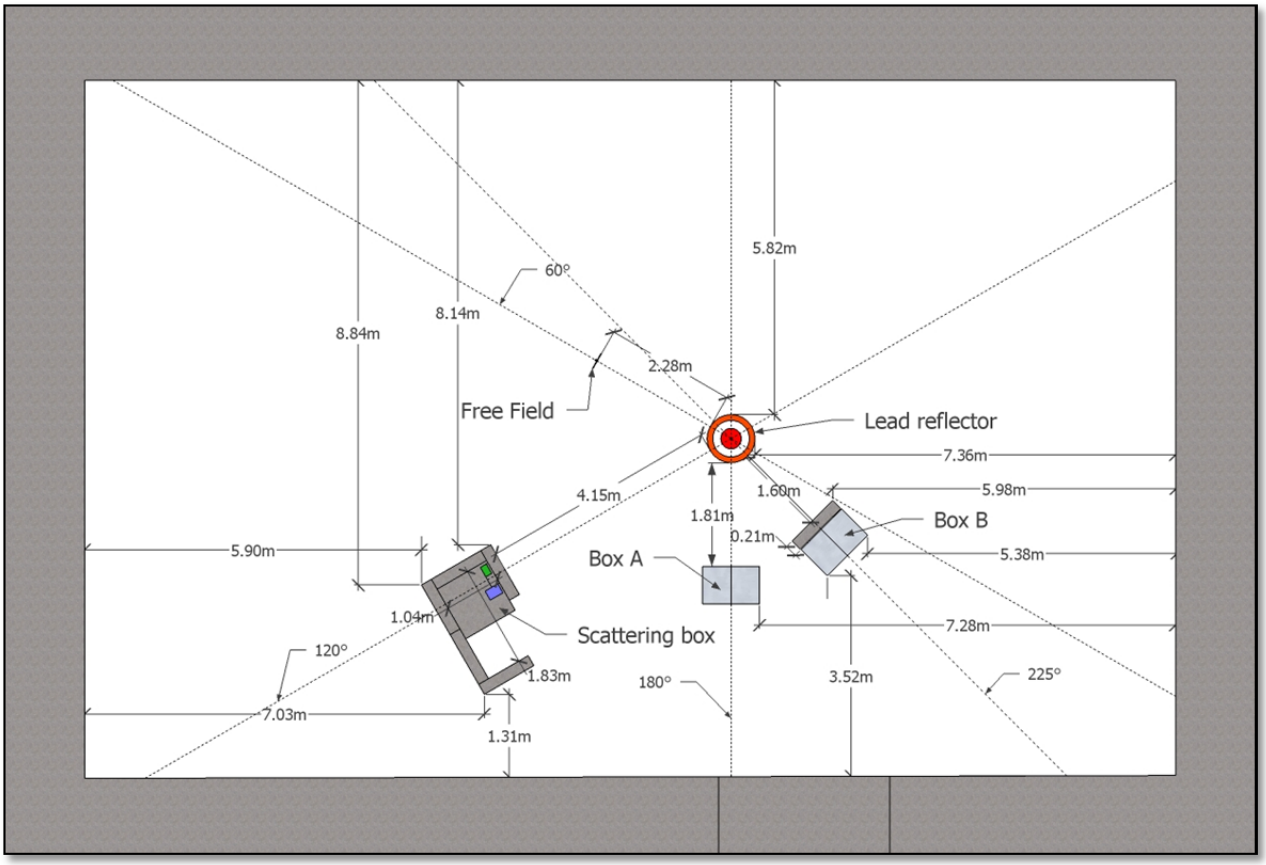


Figure 9: Pulse Two Layout

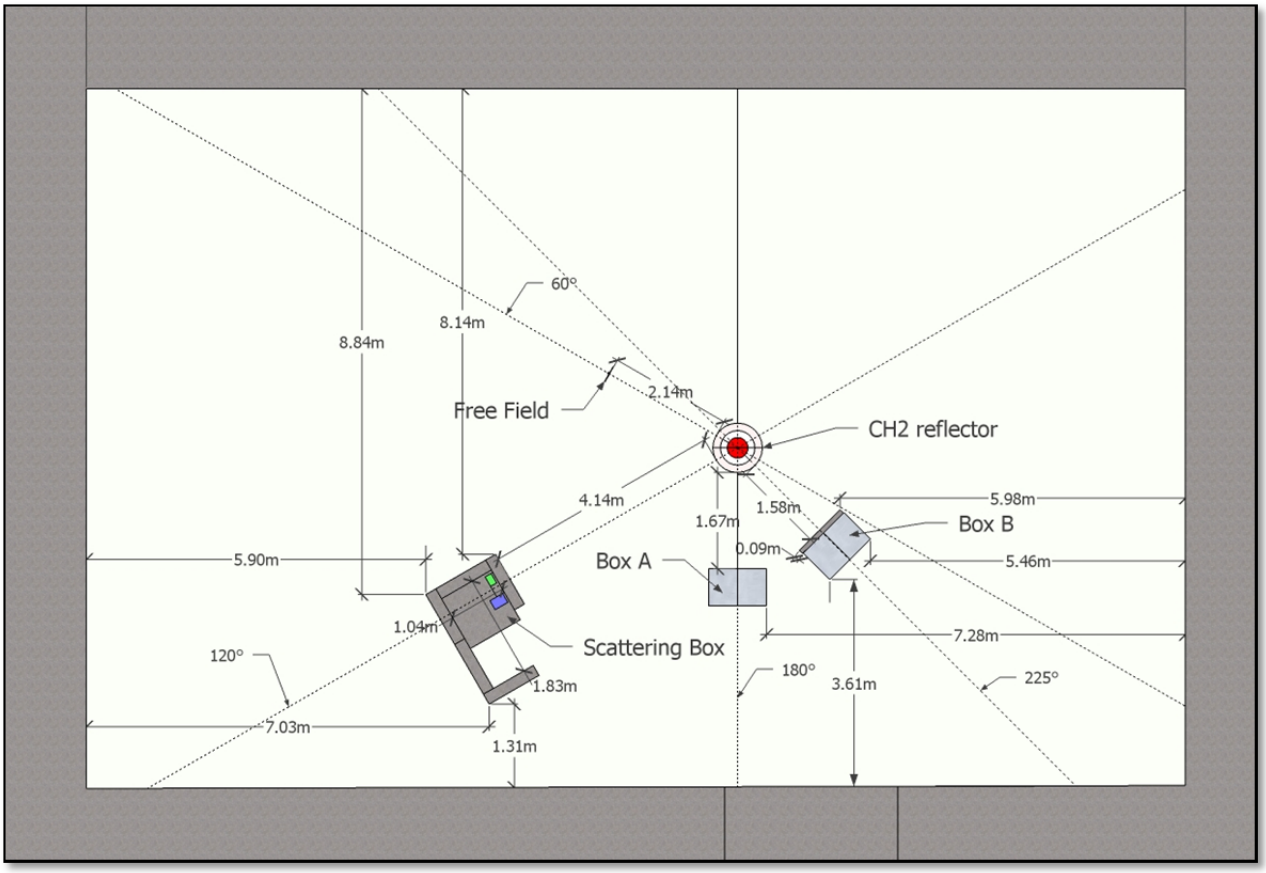


Figure 10: Pulse Three Layout

2. Theory

Before proceeding with a discussion of the computational tools used to perform the various calculations in this dissertation some discussion of the underlying theoretical constructs used in these tools is necessary.

2.1 Forward Transport Equation Derivation

The first step in any problem dealing with radiation is the development of a tool to track particles in the radiation field and to model the interactions of these particles with the matter around them. The Boltzmann Transport Equation (BTE) is the main theoretical construct used to perform this task. The development of the BTE starts with several assumptions and definitions. (Duderstadt & Hamilton, 1976), (Lewis & Miller, Jr., 1993), (Chilton, Shultis, & Faw, 1984), (Stacey, 2001)

2.1.1 Assumptions

- Particles are considered as points
- Particles travel in straight lines between collisions with a constant speed
- Particle-Particle interactions are ignored
- Collisions are considered instantaneous
- Material properties are isotropic
- Properties of nuclei and materials are known and time independent
- Only expected (mean) values of distributions are considered

2.1.2. Definitions

n= Particle Density, Number of Particles per unit volume.

$\nu(E)$ = Mean Number of Fission Neutrons produced in a fission event caused by a neutron with energy E.

$\chi(E)dE$ = probability that a fission neutron will have an energy E within the range dE.

$\tilde{\sigma}(E)$ = Microscopic Cross Section, Effective cross sectional area per nucleus seen by a particle in units of cm^2 or barns (b).

$\sigma(E) = n\tilde{\sigma}(E)$, Macroscopic Cross Section, $n\tilde{\sigma}(E)$, probability per unit path length that a particle interaction will occur.

Neutron Cross Sections

$\tilde{\sigma}_a(E)$ = Microscopic Neutron Absorption Cross Section (capture plus fission).
Capture is $(n,\gamma)$and fission is $(n,f)$with $\nu(E)$neutrons emitted with one or more gamma's.

$\tilde{\sigma}_s(E) = \tilde{\sigma}_{ES}(E) + \tilde{\sigma}_{IES}(E)$, Microscopic Neutron Scattering Cross Section
ES, Elastic Scatter, conservation of kinetic energy and momentum.
IES, Inelastic Scatter, Loss of kinetic energy and momentum to elevate energy state of the nucleus; gamma rays emitted as nucleus reverts to ground state.

$\tilde{\sigma}_t = \tilde{\sigma}_a(E) + \tilde{\sigma}_s(E)$, Microscopic Total Cross Section (all interactions)

Gamma Ray Cross Sections

$\tilde{\sigma}_{a\gamma}$ = Microscopic cross section for Gamma Ray Photoelectric Effect, Photoelectric effect is absorption of a gamma ray and emission of free electrons.

$\tilde{\sigma}_{s\gamma}$ = Microscopic Cross Section for Gamma Ray Scattering, includes both Pair Production and Compton Scattering

Particle Flux Definitions

$\psi(\vec{r},\hat{\Omega},E,t) = vN(\vec{r},\hat{\Omega},E,t)dVd\Omega dEdt$, Angular Flux, Total path length traveled by all particles in $dVd\Omega dE$ during time dt

$\phi(\vec{r},E,t) =$ Scalar Flux, $\int d\Omega\, \psi(\vec{r},\hat{\Omega},E,t)dVdEdt$

2.1.3. Derivation

Let's define a Phase Space Element as shown in Figure 11, now we can now perform a balance of all particles inside the phase space element as shown in Figure 12 using the following definitions:

- Term 1 = Number of particles "born" inside the Phase Space Element
- Term 2 = Number of particles streaming out of the Phase Space Element
- Term 3 = Number of particles leaving Phase Space Element due to collisions
- Term 4 = Increase in particles in Phase Space Element

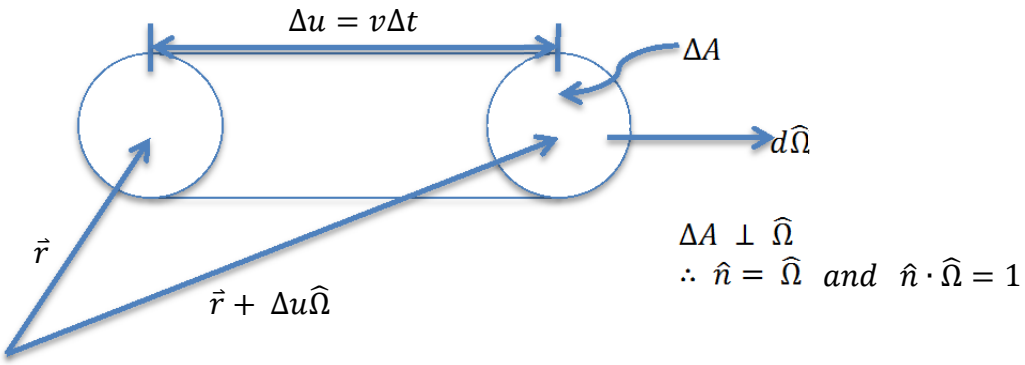


Figure 11: Phase Space Element

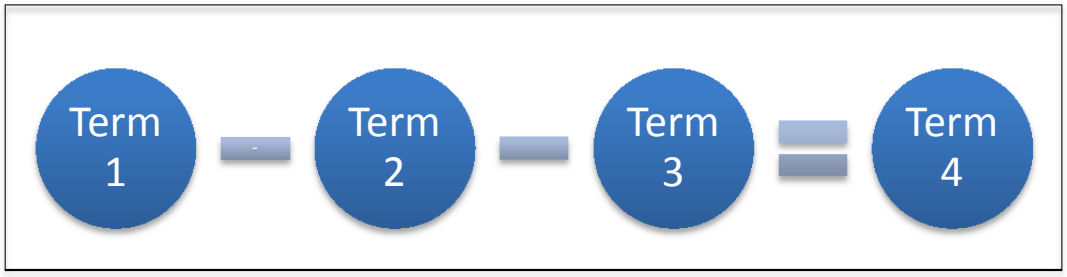


Figure 12: Phase Space Element Neutron Balance Pictorial Representation

Let's proceed term by term through the particle balance defined in Figure 12.

2.1.3.1. Term 1: Number Particles Born in the Phase Space Element

The number of particles "born" in the phase space element combines all external sources into a single term (Fixed, Fission, In-Scatter).

(2- 1)

$$T1 = q(\vec{r}, E, \hat{\Omega}, t)\Delta u \Delta A \Delta t d\Omega dE$$

2.1.3.2. Term 2: Number of Particles Streaming Out of the Phase Space Element

In order to determine the number of particles streaming out of the phase space element we must start by defining the directions that the particles may travel when leaving the phase space element. Recall that the unit vector defining the direction of travel, $\hat{\Omega}$, is aligned with the phase space element such that:

- Particles can cross into and out of the element only by crossing ΔA;
- $\hat{n} \cdot \hat{\Omega} = 1$

Recall that the number of particles Crossing ΔA is:

(2- 2)

$$\hat{n} \cdot \hat{\Omega}\psi(\vec{r}, E, \hat{\Omega}, t)d\Omega dE dA dt$$

If we take expression (2-2) and rewrite $\psi = vN$ and $dA = \Delta A$ and use these definitions when we take the difference between those particles crossing ΔA at $\vec{r}$ and those crossing ΔA at $\vec{r} + \Delta u$ we obtain:

(2- 3)

$$vN(\vec{r} + \Delta u\hat{\Omega}, E, \hat{\Omega}, t)\Delta A \Delta t d\Omega dE - vN(\vec{r}, E, \hat{\Omega}, t)\Delta A \Delta t d\Omega dE$$

We can factor out the particle velocity, v to obtain the expression for Term 2.

(2- 4)

$$T2 = v[N(\vec{r} + \Delta u\hat{\Omega}, E, \hat{\Omega}, t) - N(\vec{r}, E, \hat{\Omega}, t)]\Delta A\Delta t d\Omega dE$$

2.1.3.3. Term 3: Number of Particles Leaving Phase Space Element due to Collisions

If we assume that every particle interaction results in a change in either direction of travel ($\hat{\Omega}$), particle energy (E), or BOTH then we can express the number of particles leaving the phase space element through collisions in terms of the particle density in the phase space element and the volume of the phase space element.

(2- 5)

[#Particles crossing dA in time dt] = [Particle Density]*[Volume]

Revisiting the phase space definition in Figure 11 we can rewrite (2-5) as:

(2- 6)

$$= \{N(\vec{r}, E, \hat{\Omega}, t)d\Omega dE\} * \{(\hat{n} \cdot \hat{\Omega})dAvdt\}$$

Re-arranging terms we obtain:

(2- 7)

$$= (\hat{n} \cdot \hat{\Omega})vN(\vec{r}, E, \hat{\Omega}, t)d\Omega dE dA dt$$

Using our definition for flux, $\psi = vN$ and substituting it into equation (2-7) we obtain:

(2- 8)

$$T3 = (\hat{n} \cdot \hat{\Omega})\psi(\vec{r}, E, \hat{\Omega}, t)d\Omega dE dA dt$$

2.1.3.4. Term 4: net Change in Number of Particles in Phase Space Element

The expression for term 4 follows fairly quickly as follows, the number of interactions in time dt is equal to the total distance traveled by particles during time dt multiplied by the probability of interaction per unit path length or in mathematical terms:

(2- 9)

$$T4 = \left[vdtN\left(\vec{r}, E, \hat{\Omega}, t\right)dvdEd\Omega dt\right] * \left[\sigma_t(\vec{r}, E)\right]$$

2.1.3.5. Putting it All Together

Putting it all together as previously noted in Figure 12 and using the definitions from equations (2-1), (2-4), (2-8) and (2-9) we can write our phase space balance equation as follows:

(2- 10)

$$\mathrm{T4} = \mathrm{T1} - \mathrm{T2} - \mathrm{T3}$$

(2- 11)

$$\begin{aligned}\left[v\ dt\ N\left(\vec{r}, E, \hat{\Omega}, t\right)dv\ dE\ d\Omega\ dt\right] * \left[\sigma_t(\vec{r}, E)\right] \\ = q\left(\vec{r}, E, \hat{\Omega}, t\right)\Delta u\ \Delta A\ \Delta t\ d\Omega\ dE \\ - \ v\left[N\left(\vec{r} + \Delta u\hat{\Omega}, E, \hat{\Omega}, t\right) - \ N\left(\vec{r}, E, \hat{\Omega}, t\right)\right]\Delta A\ \Delta t\ d\Omega\ dE \\ - \ \left(\hat{n} \cdot \hat{\Omega}\right)\psi\left(\vec{r}, E, \hat{\Omega}, t\right)d\Omega\ dE\ dA\ dt\end{aligned}$$

Divide both sides in equation (2-11) by $\Delta u\Delta A\Delta t d\Omega dE$ and substitute $\psi\left(\vec{r}, E, \hat{\Omega}, t\right) = vN(\vec{r}, E, \hat{\Omega}, t)$ to obtain:

(2- 12)

$$\frac{1}{v}\left[\frac{\psi\left(\vec{r}, E, \hat{\Omega}, t + \Delta t\right) - \ \psi\left(\vec{r}, E, \hat{\Omega}, t\right)}{\Delta t}\right] + \left[\frac{\psi\left(\vec{r} + \Delta u\hat{\Omega}, E, \hat{\Omega}, t\right) - \psi\left(\vec{r}, E, \hat{\Omega}, t\right)}{\Delta u}\right] + \sigma_t\psi\left(\vec{r}, E, \hat{\Omega}, t\right) = q(\vec{r}, E, \hat{\Omega}, t)$$

If we take the limit as Δt and Δu go to zero in equation (2-12) we arrive at an expression for the Forward BTE:

(2- 13)

$$\frac{1}{v}\frac{\partial}{\partial t}\left[\psi(\vec{r}, E, \hat{\Omega}, t)\right] + \frac{d}{du}\left[\psi(\vec{r}, E, \hat{\Omega}, t)\right] + \sigma_t \psi(\vec{r}, E, \hat{\Omega}, t) = q(\vec{r}, E, \hat{\Omega}, t)$$

The next step in our derivation of the forward Boltzmann transport equation is to remove the dependence on u from the equation. Consider the unit vector definitions shown in Figure 13. Note that we have defined u as the direction of particle travel and $\vec{r} = (x, y, z)$ as the particle position in Cartesian coordinates. Using these definitions we can define the following:

(2- 14)

$$x(u) = (\hat{\Omega} \cdot \hat{\imath})u \qquad y(u) = (\hat{\Omega} \cdot \hat{\jmath})u \qquad z(u) = (\hat{\Omega} \cdot \hat{k})u$$

If we have a function F(u) defined as shown in equation (2-15) we can define its derivative as shown in equation (2-16).

(2- 15)

$$F(u) = \{x(u), y(u), z(u)\}$$

(2- 16)

$$\frac{\partial F}{\partial u} = \frac{\partial F}{\partial x}\frac{\partial x}{\partial u} + \frac{\partial F}{\partial y}\frac{\partial y}{\partial u} + \frac{\partial F}{\partial z}\frac{\partial z}{\partial u}$$

Recall that we can express the projection of u onto any of the major axes in terms of unit vectors in a dot product relationship as shown below in equation (2-17).

(2- 17)

$(\hat{\Omega} \cdot \hat{\imath})u$ = projection of u onto the x-axis
$(\hat{\Omega} \cdot \hat{\jmath})u$ = projection of u onto the y-axis
$(\hat{\Omega} \cdot \hat{k})u$ = projection of u onto the z-axis

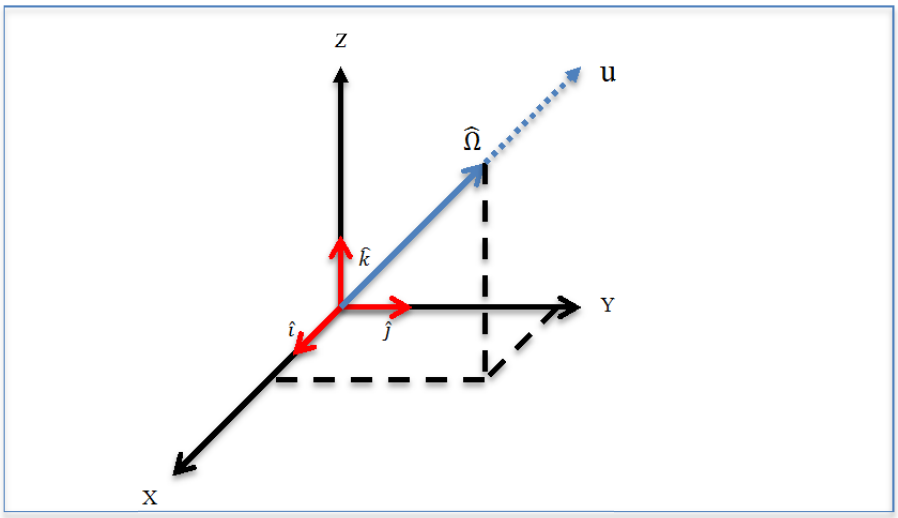


Figure 13: Unit Vectors for BTE Derivation

Using (2-17), the derivatives of the Cartesian coordinate functions in terms of u can now be re-written as:

(2- 18)

$$\left.\begin{aligned}\frac{\partial \mathrm{x}}{\partial \mathrm{u}} &= \left(\hat{\Omega}\cdot\hat{\imath}\right)\\ \frac{\partial \mathrm{y}}{\partial \mathrm{u}} &= \left(\hat{\Omega}\cdot\hat{\jmath}\right)\\ \frac{\partial \mathrm{z}}{\partial \mathrm{u}} &= \left(\hat{\Omega}\cdot\hat{\mathrm{k}}\right)\end{aligned}\right\}$$

If the angular flux, ψ, is substituted for F in equation (2-16) the following expression can be written:

(2- 19)

$$\frac{\partial \psi}{\partial \mathrm{u}} = \frac{\partial \psi}{\partial \mathrm{x}}\frac{\partial \mathrm{x}}{\partial \mathrm{u}} + \frac{\partial \psi}{\partial \mathrm{y}}\frac{\partial \mathrm{y}}{\partial \mathrm{u}} + \frac{\partial \psi}{\partial \mathrm{z}}\frac{\partial \mathrm{z}}{\partial \mathrm{u}}$$

The definitions for the derivatives of x, y, and z in terms of u from equation (2-18) can be substituted into equation (2-19) to obtain:

(2- 20)

$$\frac{\partial \psi}{\partial \mathrm{u}} = \frac{\partial \psi}{\partial \mathrm{x}}\left(\hat{\Omega}\cdot\hat{\imath}\right) + \frac{\partial \psi}{\partial \mathrm{y}}\left(\hat{\Omega}\cdot\hat{\jmath}\right) + \frac{\partial \psi}{\partial \mathrm{z}}\left(\hat{\Omega}\cdot\hat{\mathrm{k}}\right)$$

Recall that the definition of the Gradient in Cartesian coordinates is:

(2- 21)

$$\vec{\nabla} = \frac{\partial}{\partial \mathrm{x}}\hat{\imath} + \frac{\partial}{\partial \mathrm{y}}\hat{\jmath} + \frac{\partial}{\partial \mathrm{z}}\hat{\mathrm{k}}$$

Using the definition of the Gradient from equation (2-21) we can define the Gradient of the Angular Flux as follows:

(2- 22)

$$\vec{\nabla}\psi = \frac{\partial\psi}{\partial \mathrm{x}}\hat{\mathrm{i}} + \frac{\partial\psi}{\partial \mathrm{y}}\hat{\mathrm{j}} + \frac{\partial\psi}{\partial \mathrm{z}}\hat{\mathrm{k}}$$

Equation (2-22) can now be used in equation (2-20) to obtain $\frac{\partial\psi}{\partial \mathrm{u}} = \hat{\Omega} \cdot \vec{\nabla}\Psi$ which can be substituted into our earlier form of the BTE (Equation 2-13) to obtain the final expression for the time dependent, forward Boltzmann Transport Equation.

(2- 23)

$$\frac{1}{\mathrm{v}}\frac{\partial}{\partial \mathrm{t}}\left[\psi\left(\vec{\mathrm{r}}, \mathrm{E}, \hat{\Omega}, \mathrm{t}\right)\right] + \hat{\Omega} \cdot \vec{\nabla}\psi\left(\vec{\mathrm{r}}, \mathrm{E}, \hat{\Omega}, \mathrm{t}\right) + \sigma_{\mathrm{t}}\psi\left(\vec{\mathrm{r}}, \mathrm{E}, \hat{\Omega}, \mathrm{t}\right) = \mathrm{q}\left(\vec{\mathrm{r}}, \mathrm{E}, \hat{\Omega}, \mathrm{t}\right)$$

2.2 Adjoint Transport Equation Derivation

The forward BTE is the fundamental balance equation solved by the various computational tools discussed in the next chapter. This balance equation allows us to estimate the neutron flux everywhere which in turn is used to compute the reaction rates for the various activation reactions tallied by these tools. The adjoint BTE is another form of this balance equation also used by the computational tools discussed in the next chapter. The adjoint form of the BTE can be interpreted as mapping the importance of the particles being tracked in our simulations. This estimate of particle importance will be used to accelerate the fixed source transport simulations by forming particle importance maps and biased sources of particles to help drive particles to the most important regions of the problem geometries. The derivation of the adjoint form of the BTE follows below. (Lewis & Miller, Jr., 1993), (Duderstadt & Hamilton, 1976), (Stacey, 2001)

First let us define the bracket notation to be used in the adjoint derivation:

$$\langle \cdot \rangle \equiv \textit{Integration over all independent variables}$$

For a given mathematical operator, L, and functions a and b the adjoint operator L^* is defined as the operator that satisfies the following:

(2- 24)

$$\langle a, Lb \rangle = \langle b, L^* a \rangle$$

It should be noted that if $L = L^*$ then the operator is said to be "self-adjoint". Let's start with the Time Independent form of the BTE written out to include both scattering and fission sources:

(2- 25)

$$\begin{aligned} \hat{\Omega} \cdot \vec{\nabla}\psi(\vec{r}, E) + \sigma_t(\vec{r}, \mathrm{E})\psi(\vec{r}, E) \\ = \int dE' \int d\Omega' \, \sigma_s\left(\vec{r}, E' \to E, \hat{\Omega}' \cdot \hat{\Omega}\right)\psi\left(\vec{r}, E', \hat{\Omega}'\right) \\ + \chi(E) \int dE' \int d\Omega' \, \nu\sigma_f(\vec{r}, E')\psi(\vec{r}, E') \end{aligned}$$

We can define an operator L as follows:

(2- 26)

$$L = \hat{\Omega} \cdot \vec{\nabla} + \sigma_t(\vec{r}, \mathrm{E}) - \int dE' \int d\Omega' \, \sigma_s\left(\vec{r}, E' \to E, \hat{\Omega}' \cdot \hat{\Omega}\right) - \chi(E) \int dE' \int d\Omega' \, \nu\sigma_f(\vec{r}, E')$$

Each term can be individually labeled in order to work with each of them individually:

(2- 27)

$$\mathrm{L} = \mathrm{L}_1 + \mathrm{L}_2 - \mathrm{L}_3 - \mathrm{L}_4$$

Where we have used the following definitions.

$$L_1 = \hat{\Omega} \cdot \vec{\nabla} \tag{2- 28}$$

$$L_2 = \sigma_t(\vec{r}, \mathrm{E}) \tag{2- 29}$$

$$L_3 = \int dE' \int d\Omega' \, \sigma_s\left(\vec{r}, E' \rightarrow E, \hat{\Omega}' \cdot \hat{\Omega}\right) \tag{2- 30}$$

$$L_4 = \chi(E) \int dE' \int d\Omega' \, \nu\sigma_f(\vec{r}, E') \tag{2- 31}$$

Using our previously defined bracket notation we can write the following:

$$\langle a, Lb \rangle \equiv \int dE \int d\Omega \int dV \, a\left(\vec{r}, E, \hat{\Omega}\right) Lb(\vec{r}, E, \hat{\Omega}) \tag{2- 32}$$

The recipe for finding the adjoint of a defined operator is:

(1) Form $\langle a, Lb \rangle$
(2) Reverse the position of a and b in (1);
(3) Reverse the integrals if necessary;
(4) Form $\langle b, L^* a \rangle$

So let's work term by term through the BTE to find the adjoint versions of each term.

2.2.1. Term L_1: Streaming Term

$$L_1 = \hat{\Omega} \cdot \vec{\nabla} \tag{2- 33}$$

$$\langle a, Lb \rangle = \int dE \int d\Omega \int dV \, a\left(\vec{r}, E, \hat{\Omega}\right) \hat{\Omega} \cdot \vec{\nabla} b(\vec{r}, E, \hat{\Omega}) \tag{2- 34}$$

use:

(2- 35)

$$\vec{\nabla}(ab) = a\vec{\nabla}b + b\vec{\nabla}a \quad \Rightarrow \quad a\vec{\nabla}b = \vec{\nabla}(ab) - b\vec{\nabla}a$$

(2- 36)

$$\therefore \langle a, Lb\rangle = \int dE \int d\Omega \int dV\, \hat{\Omega}\cdot\vec{\nabla}\left[a(\vec{r},E,\hat{\Omega})b(\vec{r},E,\hat{\Omega})\right] - \int dE \int d\Omega \int dV\, b(\vec{r},E,\hat{\Omega})\hat{\Omega}\cdot\vec{\nabla}a(\vec{r},E,\hat{\Omega})$$

Define:

(2- 37)

$$a(\vec{r},E,\hat{\Omega}) = \psi(\vec{r},E,\hat{\Omega}) \qquad and \qquad b(\vec{r},E,\hat{\Omega}) = \psi^*(\vec{r},E,\hat{\Omega})$$

Recall:

(2- 38)

$$\int_V dV\ \hat{\Omega}\cdot\vec{\nabla} f = \int_S d\Gamma\, \hat{n}\cdot\hat{\Omega}\, f$$

So in our derivation for term L1 we have:

(2- 39)

$$\int_V dV\, \hat{\Omega}\cdot\vec{\nabla}\left[\psi(\vec{r},E,\hat{\Omega})\psi^*(\vec{r},E,\hat{\Omega})\right] = \int_S d\Gamma\, \hat{n}\cdot\hat{\Omega}\left[\psi(\vec{r},E,\hat{\Omega})\psi^*(\vec{r},E,\hat{\Omega})\right]$$

If a non-reentrant surface is specified then:

(2- 40)

$$\psi(\vec{r},E,\hat{\Omega}) = 0\ for\ \hat{n}\cdot\hat{\Omega} < 0\ \ and\ \ \psi^*(\vec{r},E,\hat{\Omega}) = 0\ for\ \hat{n}\cdot\hat{\Omega} > 0$$

(2- 41)

$$\therefore \langle b, L^*a\rangle = -\int_0^\infty dE \int d\Omega \int dV\ \ b(\vec{r},E,\hat{\Omega})\hat{\Omega}\cdot\vec{\nabla}\, a(\vec{r},E,\hat{\Omega})$$

(2- 42)

$$\Rightarrow \boxed{\mathrm{L}_1^* = -\hat{\Omega}\cdot\vec{\nabla}}$$

2.2.2. Term L_2: Collisions Term

(2- 43)

$$L_2 = \sigma_t(\vec{r}, \mathrm{E})$$

(2- 44)

$$\langle a, Lb \rangle = \int dE \int d\Omega \int dV \, a(\vec{r}, E, \hat{\Omega}) \, \sigma_t(\vec{r}, \mathrm{E}) \, b(\vec{r}, E, \hat{\Omega})$$

(2- 45)

$$= \int dE \int d\Omega \int dV \, b(\vec{r}, E, \hat{\Omega}) \, \sigma_t(\vec{r}, \mathrm{E}) \, a(\vec{r}, E, \hat{\Omega})$$

(2- 46)

$$\therefore \boxed{\mathrm{L}_2^* = \sigma_t(\vec{r}, \mathrm{E})}$$

2.2.3. Term L_3: Streaming Collisions Term

(2- 47)

$$L_3 = \int dE' \int d\Omega' \, \sigma_s(\vec{r}, E' \to E, \hat{\Omega} \cdot \hat{\Omega}')$$

(2- 48)

$$\langle a, Lb \rangle = \int dE \int d\Omega \int dV \, a(\vec{r}, E, \hat{\Omega}) \int dE' \int d\Omega' \, \sigma_s(\vec{r}, E' \to E, \hat{\Omega}' \cdot \hat{\Omega}) b(\vec{r}, E', \hat{\Omega}')$$

(2- 49)

$$= \int dV \int dE' \int d\Omega' \; b(\vec{r}, E', \hat{\Omega}') \int dE \int d\Omega \; \sigma_s(\vec{r}, E' \to E, \hat{\Omega}' \cdot \hat{\Omega}) a(\vec{r}, E, \hat{\Omega})$$

(2- 50)

$$= \int dV \int dE \int d\Omega \; b(\vec{r}, E, \hat{\Omega}) \int dE' \int d\Omega' \; \sigma_s(\vec{r}, E \to E', \hat{\Omega} \cdot \hat{\Omega}') \, a(\vec{r}, E', \hat{\Omega}')$$

(2- 51)

$$\therefore \boxed{\mathrm{L}_3^* = \int dE' \int d\Omega' \, \sigma_s(\vec{r}, E \to E', \hat{\Omega} \cdot \hat{\Omega}')}$$

2.2.4. Term L_4: External Fission Source Term

(2- 52)

$$L_4 = \mathcal{X}(E) \int dE' \int d\Omega' \, \nu\sigma_f(\vec{r}, E')$$

(2- 53)

$$\langle a, Lb \rangle = \int dE \int d\Omega \int dV \, a(\vec{r}, E, \hat{\Omega}) \mathcal{X}(E) \int dE' \int d\hat{\Omega}' \, \nu\sigma_f(\vec{r}, E') b(\vec{r}, E', \hat{\Omega}')$$

(2- 54)

$$= \int dV \int dE' \int d\Omega' \; b(\vec{r}, E', \hat{\Omega}') \, \nu\sigma_f(\vec{r}, E') \int dE \int d\Omega \; \mathcal{X}(E) \, a(\vec{r}, E, \hat{\Omega})$$

(2- 55)

$$= \int dV \int dE \int d\Omega \; b(\vec{r}, E, \hat{\Omega}) \, \nu\sigma_f(\vec{r}, E) \int dE' \int d\hat{\Omega}' \; \mathcal{X}(E') a(\vec{r}, E', \hat{\Omega}')$$

(2- 56)

$$\therefore \boxed{L_4^* = \nu\sigma_f(\vec{r}, E) \int dE' \int d\hat{\Omega}' \; \mathcal{X}(E')}$$

Now, Let's put it all together using (2-27):

(2- 57)

$$L^* = -\hat{\Omega} \cdot \vec{\nabla} + \sigma_t(\vec{r}, E) - \int dE' \int d\Omega' \, \sigma_s(\vec{r}, E \to E', \hat{\Omega} \cdot \hat{\Omega}') - \nu\sigma_f(\vec{r}, E) \int dE' \int d\hat{\Omega}' \, \mathcal{X}(E')$$

Therefore, the adjoint BTE is:

(2- 58)

$$\boxed{\begin{aligned} -\hat{\boldsymbol{\Omega}} \cdot \vec{\boldsymbol{\nabla}} \boldsymbol{\psi}^*(\vec{\boldsymbol{r}}, \mathbf{E}, \hat{\boldsymbol{\Omega}}) + \; & \boldsymbol{\sigma_t}(\vec{\boldsymbol{r}}, \mathbf{E}) \boldsymbol{\psi}^*(\vec{\boldsymbol{r}}, \mathbf{E}, \hat{\boldsymbol{\Omega}}) \\ & = \int \boldsymbol{dE'} \int \boldsymbol{d\Omega'} \, \boldsymbol{\sigma_s}(\vec{\boldsymbol{r}}, \boldsymbol{E} \to \boldsymbol{E'}, \hat{\boldsymbol{\Omega}} \cdot \hat{\boldsymbol{\Omega}}') \boldsymbol{\psi}^*(\vec{\boldsymbol{r}}, \mathbf{E'}, \hat{\boldsymbol{\Omega}}') \\ & - \boldsymbol{\nu\sigma_f}(\vec{\boldsymbol{r}}, \boldsymbol{E}) \int \boldsymbol{dE'} \int \boldsymbol{d\hat{\Omega}'} \; \boldsymbol{\mathcal{X}}(\boldsymbol{E'}) \boldsymbol{\psi}^*(\vec{\boldsymbol{r}}, \mathbf{E'}, \hat{\boldsymbol{\Omega}}') \end{aligned}}$$

2.3 Detector responses and the Adjoint Flux

Since one of the primary goals of this work is to simulate the SILENE benchmark experiment we need to be able to compute the response (activation rate) achieved in the foils after each of the pulses. (Chilton, Shultis, & Faw, 1984), (Lewis & Miller, Jr., 1993)

The traditional formulation of detector response (using the forward flux) is:

(2- 59)

$$\mathcal{R} = \int_0^\infty dE \int_{4\pi} d\Omega \int_{V_d} dV \; \mathcal{S}(\vec{r}_d, E, \hat{\Omega}) \phi(\vec{r}_d, E, \hat{\Omega})$$

where: $\mathcal{S}(\vec{r}_d, E, \hat{\Omega})$ is the detector response function
$\phi(\vec{r}_d, E, \hat{\Omega})$ is the scalar flux at the detector

Some of the more common formulations of the detector response function for analytic solutions to equation (2-59) are:

(1) Point detector at $\vec{r}_0$ collimated to respond to radiation with direction $\hat{\Omega}_0$.
$\mathcal{S}(\vec{r}_d, E, \hat{\Omega}) = \mathcal{S}(E)\delta(\vec{r}_d - \vec{r}_0)\delta(\hat{\Omega} - \hat{\Omega}_0)$

(2) Isotropic Point Detector at $\vec{r}_0$.
$\mathcal{S}(\vec{r}_d, E, \hat{\Omega}) = \mathcal{S}(E)\delta(\vec{r}_d - \vec{r}_0)$

(3) Isotropic, Energy Independent, Point Detector at $\vec{r}_0$.
$\mathcal{S}(\vec{r}_d, E, \hat{\Omega}) = \mathcal{S}\,\delta(\vec{r}_d - \vec{r}_0);\ \mathcal{S} \equiv constant$

We can also express the response in terms of the adjoint flux. In order to derive the adjoint response formulation let's start by defining the forward problem in terms of Operator notation. Suppose we formulate the neutron balance as $H\Psi = q_{external}$ for a fixed source transport problem.

We will note the following assumptions for this derivation:

(1) $\Psi(\vec{r}, \hat{\Omega}, E) = 0,\ \vec{r} \in \Gamma,\ \hat{n} \cdot \hat{\Omega} < 0$
(2) $\hat{\Omega} \cdot \vec{\nabla}\Psi(\vec{r}, \hat{\Omega}, E)$must be finite
(3) $\Psi(\vec{r}, \hat{\Omega}, E)$ must be continuous in direction of particle travel

We want to know the response, $\mathcal{R}$ (detector response in foil) for a material with total cross section σ_d and volume V_d at position $\vec{r}_d$:

(2- 60)

$$\mathcal{R} = V_d \int dE\, \sigma_d(E)\phi(\vec{r}_d, E)$$

The adjoint formulation is:

(2- 61)

$$H^{+}\Psi^{+} = \sigma_d \mathrm{V}_d \delta(\vec{r} - \vec{r}_d)$$

where we require:

(2- 62)

$$\Psi^{+}\left(\vec{r}, E, \hat{\Omega}\right) = 0\,, \qquad \vec{r} \in \Gamma,\ \hat{\Omega} \cdot \hat{n} \geq 0 \ \Rightarrow \ \int dV\ \Psi^{+}\,\hat{\Omega} \cdot \vec{\nabla}\Psi = -\int dV\ \Psi\,\hat{\Omega} \cdot \vec{\nabla}\,\Psi^{+}$$

If we multiply the original forward formulation by Ψ^{+} and integrate we get:

(2- 63)

$$\langle \Psi^{+}\mathrm{H}\Psi = \Psi^{+} q_{external} \rangle$$

If we multiply the adjoint formulation by Ψ and integrate we get:

(2- 64)

$$\langle \Psi \mathrm{H} \Psi^{+} = \Psi \sigma_d \mathrm{V}_d \delta(\vec{r} - \vec{r}_d) \rangle = \mathcal{R}$$

If we take the difference of the two equations we obtain:

(2- 65)

$$\langle \Psi^{+}\mathrm{H}\Psi \rangle - \langle \Psi \mathrm{H} \Psi^{+} \rangle = \langle \Psi^{+} q_{external} \rangle - \mathcal{R}$$

Recall that $\langle \Psi^{+}\mathrm{H}\Psi \rangle = \langle \Psi \mathrm{H} \Psi^{+} \rangle$ from our adjoint BTE derivation so the left hand side of the equation reduces to zero and we obtain equation (2-66).

(2- 66)

$$\therefore \boxed{\mathcal{R} = \langle \Psi^{+} q_{external} \rangle}$$

This means that once the adjoint flux for our problem has been determined (a single adjoint transport calculation) we can compute the response of interest with a single integration to fold the external source and adjoint flux together. Also, if the source changes for any reason we can still use the previously determined adjoint flux to compute a new response by integrating it with the new source.

2.4 Consistent Adjoint Driven Importance Sampling (CADIS)

The SCALE code package, used in this work, uses an adjoint discrete ordinates calculation to estimate the adjoint fluxes in a problem and then uses that information to generate a biased source distribution and an importance map to be used as variance reduction parameters during the final fixed source Monte Carlo calculation. (Oak Ridge National Laboratory, June 2011) The method is called Consistent Adjoint Driven Importance Sampling (CADIS) and a brief description of it is given below. (Kalos & Whitlock, 1986), (Haghighat & Wagner, 2003), (Peplow, Monte Carlo Shielding Analysis Capabilities with MAVRIC, 2011), (Peplow, Mosher, & Evans, Consistent Adjoint Driven Importance Sampling using Space, Energy, and Angle, August 2012)

Recall equation (2-66) and let's expand it as follows:

(2- 67)

$$\mathcal{R} = \int_{\vec{r},E,\widehat{\Omega}} \Psi^*(\vec{r},E,\widehat{\Omega}) q_{ext}(\vec{r},E,\widehat{\Omega}) d\vec{r}dEd\Omega$$

The normal Monte Carlo solution method would be to sample our independent variables from $q_{ext}(\vec{r},E,\widehat{\Omega})$ and fold them into the integration in equation (2-67). However, $q_{ext}(\vec{r},E,\widehat{\Omega})$ is not always the best pdf from which to sample. Importance theory tells us that an alternate pdf can be selected which will better minimize the variance in the calculated response, $\mathcal{R}$.

This alternate pdf can be introduced by multiplying the numerator and denominator of equation (2-67) by $\hat{q}(\vec{r},E,\widehat{\Omega})$. The resulting equation is:

(2- 68)

$$\mathcal{R} = \int_{\vec{r},E,\widehat{\Omega}} \left[\frac{\Psi^*(\vec{r},E,\widehat{\Omega}) q_{ext}(\vec{r},E,\widehat{\Omega})}{\hat{q}(\vec{r},E,\widehat{\Omega})}\right] \hat{q}(\vec{r},E,\widehat{\Omega}) d\vec{r}dEd\Omega$$

In order for equation (2-68) to be valid we require the following:

(2- 69)

$$\hat{q}(\vec{r},E,\widehat{\Omega}) \geq 0$$

(2- 70)

$$\int_{\vec{r},E,\widehat{\Omega}} \hat{q}(\vec{r},E,\widehat{\Omega})\, d\vec{r}dEd\Omega = 1$$

Solving equation (2-68) for $\hat{q}(\vec{r},E,\widehat{\Omega})$ yields the following equation:

(2- 71)

$$\hat{q}(\vec{r},E,\widehat{\Omega}) = \frac{\Psi^*(\vec{r},E,\widehat{\Omega}) q_{ext}(\vec{r},E,\widehat{\Omega})}{\int_{\vec{r},E,\widehat{\Omega}} \Psi^*(\vec{r},E,\widehat{\Omega}) q_{ext}(\vec{r},E,\widehat{\Omega}) d\vec{r}dEd\Omega}$$

Equation (2-71) is the biased source to be used in the CADIS method. Note that the numerator of equation (2-71) is the detector response for our phase space element $d\vec{r}dEd\Omega$ and the denominator is the total response. Therefore, equation (2-71) is a ratio representing the contribution of our element of phase space to the detector response and so our alternate pdf has a physical basis. Monte Carlo integration of equation (2-71) will yield a zero variance result if the response is known ahead of time. However, the response is not generally known ahead of time and so the particle transport will need to be simulated using the biased source from equation (2-71) in order to arrive at an estimate of the adjoint flux.

Because the source particles for our transport simulation are selected from a biased pdf the statistical weights of the particles must be adjusted so that the following balance relationship is still satisfied.

(2- 72)

$$w(\vec{r},E,\hat{\Omega})\hat{q}(\vec{r},E,\hat{\Omega}) = w_0(\vec{r},E,\hat{\Omega})q_{ext}(\vec{r},E,\hat{\Omega})$$

where $w_0(\vec{r},E,\hat{\Omega})$ is equal to 1.0.

If we substitute equation (2-71) into equation (2-72) we will obtain an expression for the statistical weights of the particles.

(2- 73)

$$w(\vec{r},E,\hat{\Omega}) = \frac{\int_{\vec{r},E,\hat{\Omega}} \Psi^*(\vec{r},E,\hat{\Omega})q_{ext}(\vec{r},E,\hat{\Omega})d\vec{r}dEd\Omega}{\Psi^*(\vec{r},E,\hat{\Omega})} = \frac{\mathcal{R}}{\Psi^*(\vec{r},E,\hat{\Omega})}$$

Returning to the our original balance equation, we can write the integral form of the Boltzmann equation as follows:

(2- 74)

$$\Psi(\vec{r},E,\hat{\Omega}) = \int K(\vec{r}',E',\hat{\Omega}' \rightarrow \vec{r},E,\hat{\Omega})\Psi(\vec{r}',E',\hat{\Omega}')d\vec{r}'\,dE'\,d\hat{\Omega}' + q(\vec{r},E,\hat{\Omega})$$

where $K(\vec{r}',E',\hat{\Omega}' \rightarrow \vec{r},E,\hat{\Omega})d\vec{r}\,dE'd\hat{\Omega}'$ is the expected number of particles emerging in $d\vec{r}\;dE\;d\hat{\Omega}$ about $\vec{r},E,\hat{\Omega}$ from events in $d\vec{r}'\,dE'\,d\hat{\Omega}'$ about $\vec{r}'\;E'\;\hat{\Omega}'$ and $q(\vec{r},E,\hat{\Omega})$ is the source density.

If we multiply (2-74) by $\frac{\Psi^*(\vec{r},E,\hat{\Omega})}{\mathcal{R}}$ we obtain an expression for the transport equation with a biased source (2-75).

(2- 75)

$$\hat{\Psi}(\vec{r},E,\hat{\Omega}) = \int K(\vec{r}',E',\hat{\Omega}' \rightarrow \vec{r},E,\hat{\Omega})\Psi\left(\overrightarrow{r'},E',\hat{\Omega}'\right)\frac{\Psi^*(\vec{r},E,\hat{\Omega})}{\mathcal{R}}d\overrightarrow{r'}\,dE'\,d\hat{\Omega}' + \hat{q}(\vec{r},E,\hat{\Omega})$$

where we have defined

(2- 76)

$$\hat{\Psi}(\vec{r},E,\hat{\Omega}) = \frac{\Psi^*(\vec{r},E,\hat{\Omega})\Psi(\vec{r},E,\hat{\Omega})}{\mathcal{R}}$$

and used equation (2-71) for the biased source, $\hat{q}(\vec{r},E,\hat{\Omega})$.

Substituting (2-76) into (2-75) and defining

(2- 77)

$$\hat{K}(\overrightarrow{r'},E',\hat{\Omega}' \rightarrow \vec{r},E,\hat{\Omega}) = K(\overrightarrow{r'},E',\hat{\Omega}' \rightarrow \vec{r},E,\hat{\Omega})\frac{\Psi^*(\vec{r},E,\hat{\Omega})}{\Psi^*(\overrightarrow{r'},E',\hat{\Omega}')}$$

yields

(2- 78)

$$\hat{\Psi}(\vec{r},E,\hat{\Omega}) = \int \hat{K}\left(\overrightarrow{r'},E',\hat{\Omega}' \rightarrow \vec{r},E,\hat{\Omega}\right)\hat{\Psi}\left(\overrightarrow{r'},E',\hat{\Omega}'\right)d\overrightarrow{r'},dE',d\hat{\Omega}' + \hat{q}(\vec{r},E,\hat{\Omega})$$

We are using the ratio of the adjoint importance functions to alter the transport kernel. In practice this alteration of the number of particles emerging in our phase space element can be accomplished by splitting or rouletting particles as follows:

(2- 79)

$$For\ \frac{\Psi^*(\vec{r},E,\hat{\Omega})}{\Psi^*\left(\overrightarrow{r'},E',\hat{\Omega}'\right)} > 1, particles\ are\ created\ (splitting)$$

and

(2- 80)

$$For\ \frac{\Psi^*(\vec{r},E,\hat{\Omega})}{\Psi^*\left(\overrightarrow{r'},E',\hat{\Omega}'\right)} < 1, particles\ are\ destroyed\ (roulette).$$

We must alter the statistical weights of the particles since we are altering the number of particles in order to conserve particle weight. The original particle weight conservation relation found in equation (2-72) can be re-written as:

(2- 81)

$$w(\vec{r},E,\hat{\Omega})K\left(\overrightarrow{r'},E',\hat{\Omega}'\rightarrow\vec{r},E,\hat{\Omega}\right)\left[\frac{\Psi^*\left(\overrightarrow{r'},E',\hat{\Omega}'\right)}{\Psi^*(\vec{r},E,\hat{\Omega})}\right]=w\left(\overrightarrow{r'},E',\hat{\Omega}'\right)K(\overrightarrow{r'},E',\hat{\Omega}'\rightarrow\vec{r},E,\hat{\Omega})$$

or

(2- 82)

$$w(\vec{r},E,\hat{\Omega})=w(\overrightarrow{r'},E',\hat{\Omega}')\left[\frac{\Psi^*\left(\overrightarrow{r'},E',\hat{\Omega}'\right)}{\Psi^*(\vec{r},E,\hat{\Omega})}\right]$$

Because the relationships for the particle statistical weights used in the source sampling and particle transport processes were derived from importance sampling in a consistent manner this method is called Consistent Adjoint Driven Importance Sampling (CADIS).

The relationships for the biased source and the particle weights are used to perform the Monte Carlo simulation of the fixed source transport once the adjoint flux has been estimated from the initial discrete ordinates calculation.

2.5 Forward Weighted CADIS (FW-CADIS)

The CADIS method uses the results from an adjoint discrete ordinates calculation to improve the efficiency of a forward Monte Carlo calculation by using biased source parameters and weight windows. (Peplow, Mosher, & Evans, Consistent Adjoint Driven Importance Sampling using Space, Energy, and Angle, August 2012) An extension of this methodology called Forward Weighted CADIS (FW-CADIS) has been developed to improved the efficiency of Monte Carlo calculations involving mesh tallies and problems involving multiple localized detectors. (Wagner, Peplow, & Mosher, 2013)

Recall that we can define our response in terms of either the forward or the adjoint flux.

(2- 83)

$$\mathcal{R} = \int_{\vec{r},E,\widehat{\Omega}} \Psi(\vec{r},E,\widehat{\Omega}) q^*(\vec{r},E,\widehat{\Omega}) d\vec{r}dEd\widehat{\Omega}$$

or

(2- 84)

$$\mathcal{R} = \int_{\vec{r},E,\widehat{\Omega}} \Psi^*(\vec{r},E,\widehat{\Omega}) q(\vec{r},E,\widehat{\Omega}) d\vec{r}dEd\widehat{\Omega}$$

In order to achieve uniform variance reduction over a large area such as the whole problem or a specific volume with several detectors present we can recast the response as follows.

(2- 85)

$$\mathcal{R}' = \int_{\vec{r},E,\widehat{\Omega}} \Psi(\vec{r},E,\widehat{\Omega}) \sigma_d(\vec{r},E,\widehat{\Omega})\, d\vec{r}dEd\widehat{\Omega}$$

The function $\sigma_d(\vec{r},E,\widehat{\Omega})$ is a function defined so that it converts particle flux to Monte Carlo particle density. In order to allow a large area and/or multiple tallies to converge with uniformly low statistical uncertainty the Monte Carlo particle density needs to be uniform.

Denote the physical particle density as $n(\vec{r},E,\widehat{\Omega})$ and the Monte Carlo particle density as $m(\vec{r},E,\widehat{\Omega})$. Using the fact that these two quantities are related by the average particle weight we can state the following:

(2- 86)

$$n(\vec{r},E,\widehat{\Omega}) \propto m(\vec{r},E,\widehat{\Omega})\overline{w}(\vec{r},E,\widehat{\Omega})$$

Recall also that the particle flux can be defined in terms of the particle density and the particle velocity as follows:

(2- 87)

$$\Psi(\vec{r},E,\widehat{\Omega}) = n(\vec{r},E,\widehat{\Omega})\mathrm{v}(\vec{r},E,\widehat{\Omega})$$

If we substitute (2-86) into (2-87) and rearrange terms we can solve for the Monte Carlo particle density.

(2- 88)

$$m(\vec{r}, E, \hat{\Omega}) = \left[\frac{\Psi(\vec{r}, E, \hat{\Omega})}{\overline{w}(\vec{r}, E, \hat{\Omega})\mathrm{v}(\vec{r}, E, \hat{\Omega})}\right]$$

If the average particle weight is proportional to the physical particle density then the Monte Carlo particle density will remain approximately constant – as desired.

(2- 89)

$$\text{for } m \approx constant$$
$$\overline{w} \propto n \text{ and } \overline{w}\mathrm{v} \propto \Psi$$

If we substitute $\Psi(\vec{r}, E, \hat{\Omega})$ for $[\overline{w}(\vec{r}, E, \hat{\Omega})\mathrm{v}(\vec{r}, E, \hat{\Omega})]$ in equation (2-88) and integrate over the independent variables we obtain a new expression for the response function.

(2- 90)

$$\mathcal{R}' \propto \int_{\vec{r},E,\hat{\Omega}} \Psi(\vec{r}, E, \hat{\Omega}) \left[\frac{1}{\Psi(\vec{r}, E, \hat{\Omega})}\right] d\vec{r}dEd\hat{\Omega}$$

Equating (2-90) and (2-83) we can define our adjoint importance function as follows:

(2- 91)

$$q^* = \frac{1}{\Psi(\vec{r}, E, \hat{\Omega})}$$

We have weighted the adjoint source with the inverse of the forward flux to ensure that the problem converges with approximately uniform statistical uncertainties. This new adjoint importance function is then used along with the standard CADIS methodology to produce the biased source parameters and weight windows as before.

2.6 Sensitivity and Uncertainty

Once the comparison of the measured dosimetric results to the computed estimates of the dosimetry is complete a sensitivity and uncertainty analysis of the various experimental parameters associated with the benchmark was conducted. The basic mathematical constructs used to perform this analysis are defined below. (Dean, September 2008)

First, the expected value (or mean) of a variable x is:

(2- 92)

$$\langle x \rangle = \bar{x} = \frac{1}{N}\sum_{i=1}^{N} x_i$$

The variance of x, which is a measure of the dispersion of the various estimates of x is defined as:

(2- 93)

$$\sigma^2 = \frac{1}{N}\sum_{i=1}^{N} (x_i - \overline{x})^2$$

The standard deviation of x is simply the square root of the variance of x or:

(2- 94)

$$\sigma = \sqrt{\frac{1}{N}\sum_{i=1}^{N} (x_i - \overline{x})^2}$$

The sensitivity coefficient for a variable provides a method for characterizing how sensitive one variable is to changes in another variable. For instance, the sensitivity of the response R (could be reaction rate) to changes in the parameter x (could be foil thickness) is defined as the sensitivity coefficient of R with respect to x and is given in equation form as:

(2- 95)

$$S_{R,x} = \frac{\partial R}{\partial x}$$

The uncertainty in the value of R due to the uncertainty in the parameter x can be found as:

(2- 96)

$$\sigma_{R,x} = S_{R,x}\sigma_x$$

The total standard uncertainty in the response R due to the various changes is the sum of the ΔR effects of the individual standard uncertainties in the N different experimental parameters:

(2- 97)

$$(\Delta R_{tot})^2 = \sum_{i=1}^{N}\left[\frac{\partial R}{\partial x_i}\right]^2 \sigma_i^2 + 2\sum_{i=1}^{N-1}\sum_{j=i+1}^{N}\frac{\partial R}{\partial x_i}\frac{\partial R}{\partial x_j} r_{i,j}\sigma_i\sigma_j$$

with the linear correlation coefficient $r_{x,y}$ defined as:

(2- 98)

$$r_{x,y} = \frac{\sigma_{x,y}^2}{\sigma_x\sigma_y}$$

and the covariance of two variables x and y defined as:

(2- 99)

$$\sigma_{x,y} = \frac{1}{N}\sum_{i=1}^{N}(x_i - \bar{x})(y_i - \bar{y})$$

The uncertainties computed in this dissertation are not correlated and so the correlation terms will be zero and the final combined uncertainty will be computed as follows:

(2- 100)

$$(\Delta R_{tot})^2 = \sum_{i=1}^{N}\left[\frac{\partial R}{\partial x_i}\right]^2 \sigma_i^2 = \sum_{i=1}^{N}(S_{R,x})^2\,\sigma_i^2$$

3. Computational Tools

As has been stated previously, one of the first steps in generating a computational benchmark is to choose the computational platform(s) that will be used to do the simulations and analysis. The code package chosen for the work in this dissertation was the SCALE code package developed at ORNL. (Oak Ridge National Laboratory, June 2011) There were two primary reasons for this selection. The first was the introduction of the new automated variance reduction tools (CADIS and FW-CADIS) in the latest version of SCALE. (Peplow, Monte Carlo Shielding Analysis Capabilities with MAVRIC, 2011), (Wagner, Peplow, & Mosher, 2013), (Oak Ridge National Laboratory, June 2011) These new variance reduction tools resulted in being able to compute reaction rate estimates for the selected activation foils within a reasonable amount of time whereas before the introduction of these tools it is likely that these reaction rates could not have been computed due to the size and complexity of the model involved. The second reason is the new CAAS analysis capability which uses KENO-VI to produce a mesh tally of the source which can then be converted to a mesh based source and used with MAVRIC to perform a fixed source calculation. (Peplow & Petrie, 2010), (Oak Ridge National Laboratory, June 2011)

The SCALE code package is a suite of codes that can be used to solve a variety of nuclear simulation and analysis problems in a variety of fields including criticality safety, reactor physics, radiation shielding, radioactive source term characterization, and sensitivity and uncertainty analysis. In addition to the computational modules used to solve the selected problem, the SCALE package includes current nuclear data libraries and processing tools for continuous energy and multi-group neutronics calculations. (Oak Ridge National Laboratory, June 2011)

SCALE uses a central driver to call individual executable programs (functional modules) to perform whatever computational task has been requested. SCALE uses standardized sequences to decide which code is used in what order during the process of solving a particular problem. User input for the various control modules is provided in text files, which make extensive use of keywords and engineering type input. (Oak Ridge National Laboratory, June 2011)

The Material Information Processor Library (MIPLIB) is a common set of subroutines used by SCALE that allow users to specify problem materials as individual nuclides, elements, mixtures, or solutions using easily remembered keywords. The user can use pre-defined mixtures and solutions or create their own using the arbitrary material keyword. The uranyl nitrate fuel for SILENE was modeled using the solution keyword feature of the MIPLIB while the activation foils were modeled using the arbitrary material keyword. The MIPLIB also uses keywords to take the user specified materials and prepare input for the subroutines that perform problem dependent cross section processing. (Oak Ridge National Laboratory, June 2011)

The work in this dissertation takes great advantage of the new CAAS analysis capability which has recently been added to SCALE. The CAAS analysis capability starts by using the CSAS6 control sequence in SCALE to perform a k_{eff} eigenvalue calculation using the user specified problem geometry and materials. The spatial and energy dependent source tally is created by setting the `CDS` parameter to "YES" and adding the grid geometry to the KENO input. Once the

calculation is finished the KENO source tally is converted to a MAVRIC mesh source using a new SCALE utility called MT2MSM. The final step in the analysis sequence is then to use the new mesh source and the MAVRIC control sequence to compute the foil responses (activation rates). Since the foils are measuring neutron activation only the `noSecondaries` keyword has been used in the MAVRIC input. Also, since fission has already been accounted for in the mesh source generation process the `noFissions` keyword has also been used. (Oak Ridge National Laboratory, June 2011), (Peplow & Petrie, 2010)

A pictorial representation of how the CSAS6 control sequence proceeds is shown in Figure 14. To produce the source mesh tally the Criticality Safety Analysis Sequence with KENO-VI (CSAS6) control module was used. The function of the CSAS6 control module is to perform a 3-D Monte Carlo calculation to estimate the effective multiplication of a system.

In the case of the eigenvalue calculations done for this dissertation, CSAS6 used BONAMI to perform resonance self shielding corrections on nuclides in the unresolved resonance range. The sequence then passed the corrected cross sections to WORKER, which created the problem dependent cross section library. WORKER then passed the problem dependent cross section library to the KENO-VI eigenvalue calculation, which calculated the system k_{eff} using a 3-D Monte Carlo method. (Oak Ridge National Laboratory, June 2011) Although KENO-VI estimated the system's effective neutron multiplication, it was in fact the mesh tally produced by KENO-VI that was needed. This mesh tally was converted to a mesh source using the MT2MSM utility. The mesh source was then used to represent the SILENE source term in the subsequent fixed source calculations. (Oak Ridge National Laboratory, June 2011), (Peplow & Petrie, 2010)

The fixed source simulations used both the CADIS and the FW-CADIS options to more effectively converge the reaction rate estimates in the foils. As has been discussed earlier, the CADIS methodology as implemented in SCALE uses an adjoint discrete ordinates calculation to estimate the adjoint flux everywhere in the problem. The adjoint fluxes are then used to construct an importance map and a biased source to be used together to preferentially track particles in those areas of the problem which are important to the final tally estimates. The FW-CADIS methodology simply allows the fixed source calculation to converge more than one tally more efficiently by ensuring that they all have approximately the same relative uncertainty in their estimates, which otherwise are likely all different and therefore will require differing amounts of cpu time to converge to a common level of confidence.

In the case of Collimator Box A there were 6 different foils representing 9 different reactions (4 thermal and 5 threshold), so the use of the FW-CADIS option to allow better convergence of several tallies simultaneously was an appropriate choice for these simulations.

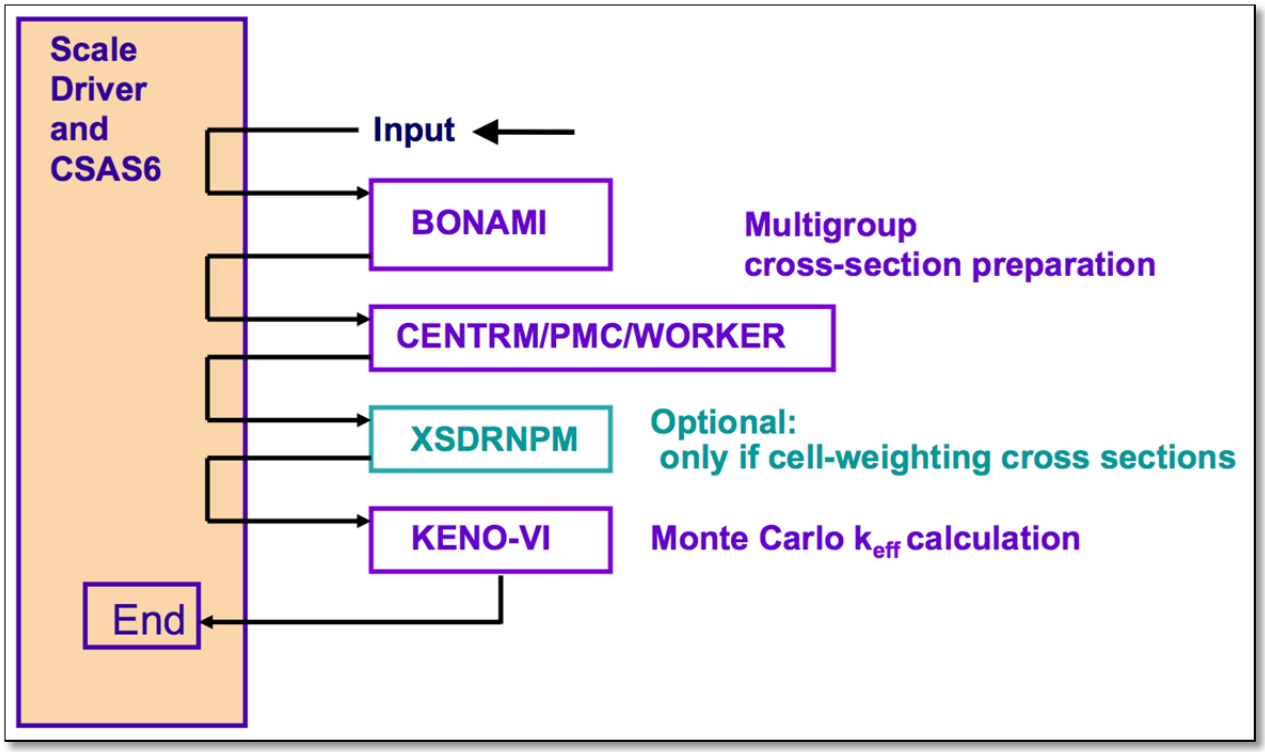


Figure 14: CSAS6 Control Module Sequence

The fixed source calculations were done using the MAVRIC sequence from the SCALE code package. Figure 15 shows a graphical representation of this computational sequence. The computational sequence starts the same way that the CSAS6 sequence started, BONAMI was used to correct the cross sections that had Bondarenko data in the unresolved resonance region and WORKER was used to create a problem dependent cross section library to be used in the remainder of the simulation. (Oak Ridge National Laboratory, June 2011)

ICE is a code designed to produce a set of mixed cross sections for the materials specified in the input file in a format usable by a subsequent computational modules. DENOVO is a new module in the current version of SCALE. DENOVO is a 3-Dimensional discrete ordinates code used to generate forward and adjoint fluxes to be used in the CADIS and FW-CADIS methods used in the MAVRIC sequence. MONACO uses Monte Carlo to perform 3-Dimensional fixed source, multigroup transport simulations for shielding and criticality accident alarm applications. (Oak Ridge National Laboratory, June 2011)

The MAVRIC sequence executes these codes in the sequence shown in Figure 15 generating an output from each computational module that is then saved and passed to the next computational module until the final estimates of flux or reaction rate are obtained at which point the sequence terminates and writes the final output. (Oak Ridge National Laboratory, June 2011)

More complete descriptions of the SCALE code package and of the various computational modules and sequences used in this work can be found in the SCALE users manual. (Oak Ridge National Laboratory, June 2011)

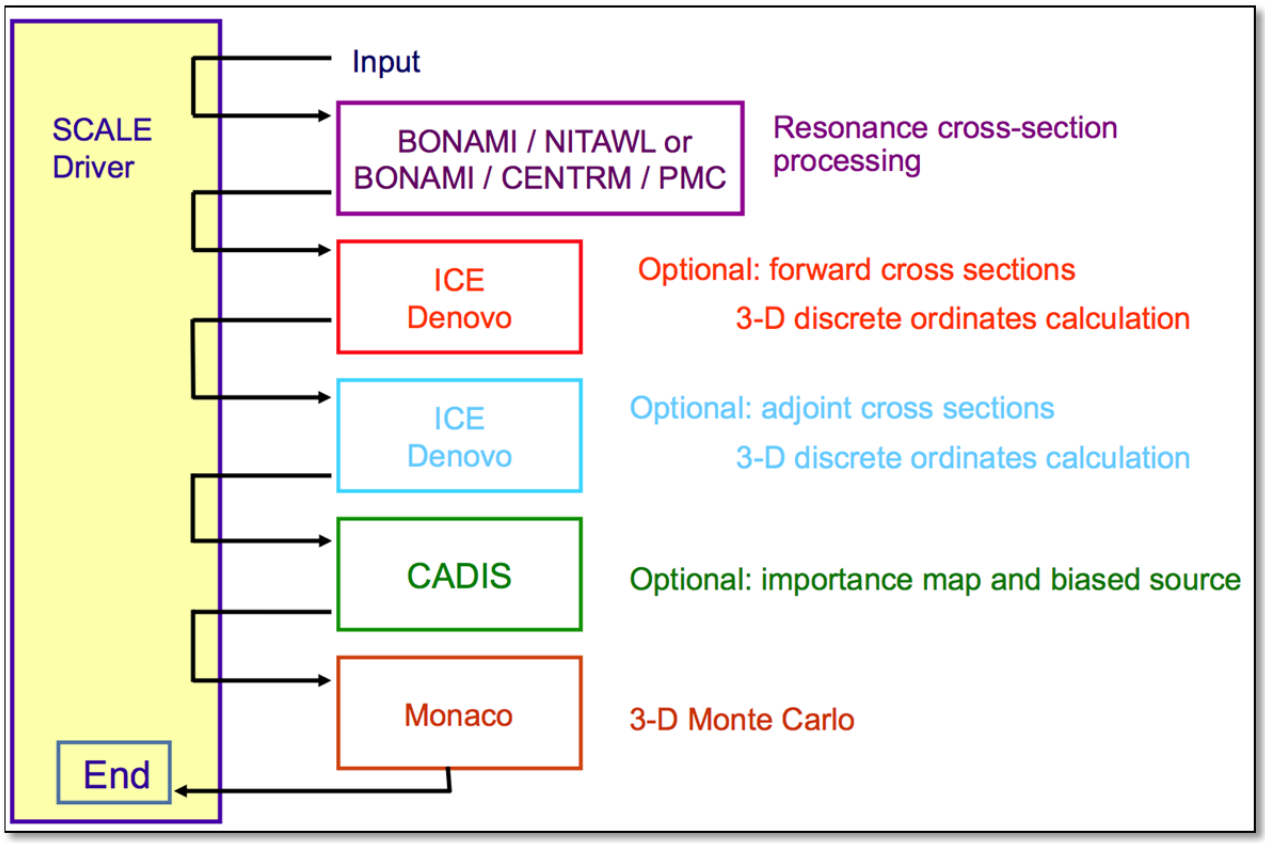


Figure 15: MAVRIC Control Sequence

4. High Fidelity 3-D Model of Pulse 1

The goal of this experimental effort is to publish a fixed source benchmark that practitioners can use to validate their computational platforms. To that end the dosimetry personnel at the CEA Valduc facility provided data detailing the activated reaction rates in all of the deployed foils and TLDs. (Chateauvieux & Piot, CAAS Test Dosimetry Report, Pulse 1, 6/16/2011), (Chateauvieux & Piot, CAAS Test Dosimetry Report, Pulse 2, 5/24/2012), (Chateauvieux & Piot, CAAS Test Dosimetry Report, Pulse 3, 5/31/2012) This dissertation attempts to model the experimental setup in two ways. First, a so called "high fidelity" 3-D model of the experiment has been constructed which includes as much detail as possible with respect to the construction of the SILENE reactor and the associated major experimental equipment (scattering box, collimator boxes, diagnostic stands and the free field location). Further the detailed model has included computational models for each of the detectors employed through out the experiment (the TLDs and the CAAS detectors). References [5] and [24] were the primary technical references for producing the computational model of the experiment. (Chateauvieux & Piot, CAAS Test Dosimetry Report, Pulse 1, 6/16/2011), (Piot, June 2011)

The SCALE package developed by ORNL has been selected as the primary computational tool due to its recent implementation of the CADIS automated variance reduction technique and the CAAS analysis methodology. Specifically, the geometry will be simulated using the KENO-VI geometry package and the fixed source calculations will be simulated using a new code sequence called MAVRIC that has been added to the SCALE toolbox. (Oak Ridge National Laboratory, June 2011)

4.1 Model Overview

The model for the pulse was constructed as a series of modules which were then inserted using the HOLE feature of KENO. The major components modeled were:

- The SILENE Reactor
- Collimator Box A
- Collimator Box B
- Scattering Box
- Free Field Location
- Diagnostic Stand A
- Diagnostic Stand B

The SILENE reactor cell was modeled as the global unit in the geometry and each of the above modules was inserted as a hole into that global room specification. This makes the sensitivity analysis to be done later much easier in that an entire piece of equipment can be eliminated from the computer model by simply commenting out one line of input. Modeling the experiment in this way is also computationally more efficient due to the complexity of the problem. If the geometry was modeled as one large series of units then every time a location needed to be calculated KENO would need to check every single surface in the problem. By inserting units as holes this location check is made simpler in that KENO will determine which hole it is in before it starts checking surfaces to determine a specific location.

The criticality accident alarm system (CAAS) detectors used in the experiment were of two different origins: (Piot, June 2011)

- Rocky Flats
- Babcock International (CIDAS)

These detectors were built and inserted into the major model pieces above using the hole option of KENO.

Also, two different TLDs were used in the experiment: (Piot, June 2011)

- HBG TLD provided by ORNL (called the ORNL TLD in the model)
- CEA TLD provided by CEA Valduc

The activation foils used were: (Piot, June 2011)

- Gold
- Iron
- Magnesium
- Cobalt
- Indium
- Nickel
- Titanium (included even though no dosimetry data has been collected)

A brief discussion of each of the major model pieces is given in the following sections along with images derived from the model.

4.2 Component Model Descriptions

4.2.1. SILENE and Reactor Cell (Room, doors, walls, etc.)

The geometry included in this model is primarily that which is contained within the SILENE reactor cell. The model extends a short distance beyond the rear wall of the cell to include the large concrete shield doors but terminates shortly thereafter. The model extends up to include the ceiling of the reactor cell including the concrete rail system for the overhead cranes. None of the miscellaneous room items (such as ladders, hand rails, door knobs, etc.) have been included in the model as they were judged to be inconsequential to the final answer.

Annex I from reference [24] provides most of the detail used to construct the global room model. (Piot, June 2011) Figure 16 shows a photograph of the reactor cell taken during the experiment. Note that a concrete shield is installed in the front of Collimator Box B. Also note the large doors directly behind Collimator Box A. The global room model extends just beyond these doors to include the large concrete shields behind them. The track in the center of the reactor cell is used to move the lead shield into and out of place. One half of the lead shield is visible on the far left side of the photograph in its “removed” position.



Figure 16: Experimental Layout of SILENE Reactor Cell

Figure 17 shows a plan view of the high fidelity computational model. When compared to the photo in Figure 16 the major pieces of equipment can be easily identified – the SILENE reactor, Collimator Box A and Box B, the Scattering Box, the Free Field Location and the two diagnostic stands. Figure 18 shows an elevation view of the global room model. This view is taken as if the viewer is standing directly in front of the large doors shown in Figure 16. The concrete structure in the top of the room to allow the cranes to operate is modeled according to the details given in Annex I of reference 24. (Piot, June 2011)

The computational model for SILENE is shown in Figure 19. Figure 16 shows SILENE in the center of the reactor cell. Recall from previous descriptions in Chapter 1 that the uranyl nitrate fuel is located in an annular region 100 cm above the floor of the reactor cell. (Piot, June 2011) The reactor sits on a steel plate, which is attached to the floor of the reactor cell. There is a small lead shield – called the lower lead shield - located 30 cm above the floor. Inside the annular fuel region is a cadmium control rod, which is pulled up out of the fuel region during the critical excursion. (Piot, June 2011)

4.2.2. Collimator Boxes

There are two collimator boxes in the final experimental setup. In all of the pulses one of the collimator boxes was unshielded (i.e. open face) and one box had a shield in front of the opening. Figure 2 shows the collimator boxes in the reactor cell with Collimator Box B on the left and Collimator Box A on the right. Annex XVI from reference [24] was the primary reference for the details of the geometry of the collimator boxes. (Piot, June 2011)

The collimator box model is constructed of several smaller modules – the support frame, the collimator box and then any detectors or foils placed inside the box. Figure 20 shows the collimator box A computational model without its frame. Note that the interior of the collimator box includes a RFP CAAS unit, an ORNL TLD, a CEA TLD and a set of activation foils. Each of these elements was modeled as a separate unit and inserted into the box using the KENO hole function. Figure 21 shows photographs of the interior of the Collimator Boxes during the experiment for comparison. The photograph of Box A is on the left and the photo of Box B is on the right.

The interior and exterior of the collimator boxes are sheathed in a 2 mm thick layer of stainless steel. Underneath the interior stainless steel layer is a 5 mm thick layer of copper followed by a 10 mm thick layer of lead. (Piot, June 2011) The remainder of the interior of the collimator boxes is occupied by a material called PPB9. PPB9 is borated plaster with polyethylene beads, but its exact composition is discussed in section 4.3.3. The total effect of these separate material regions is to collimate the radiation field from SILENE so that scattering from other equipment in the room is not a primary contributor to the radiation seen by the activation foils.

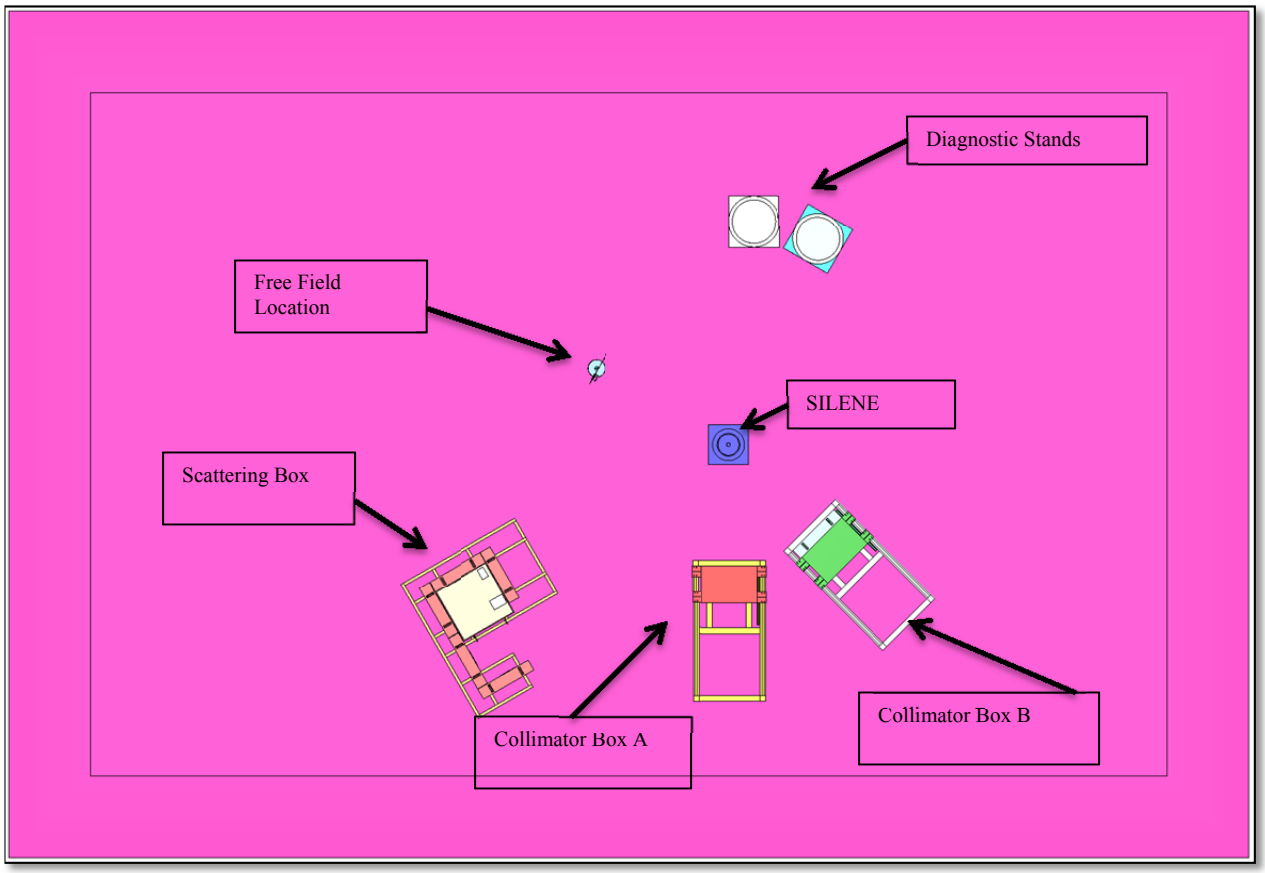


Figure 17: Top View of SILENE Reactor Cell Model

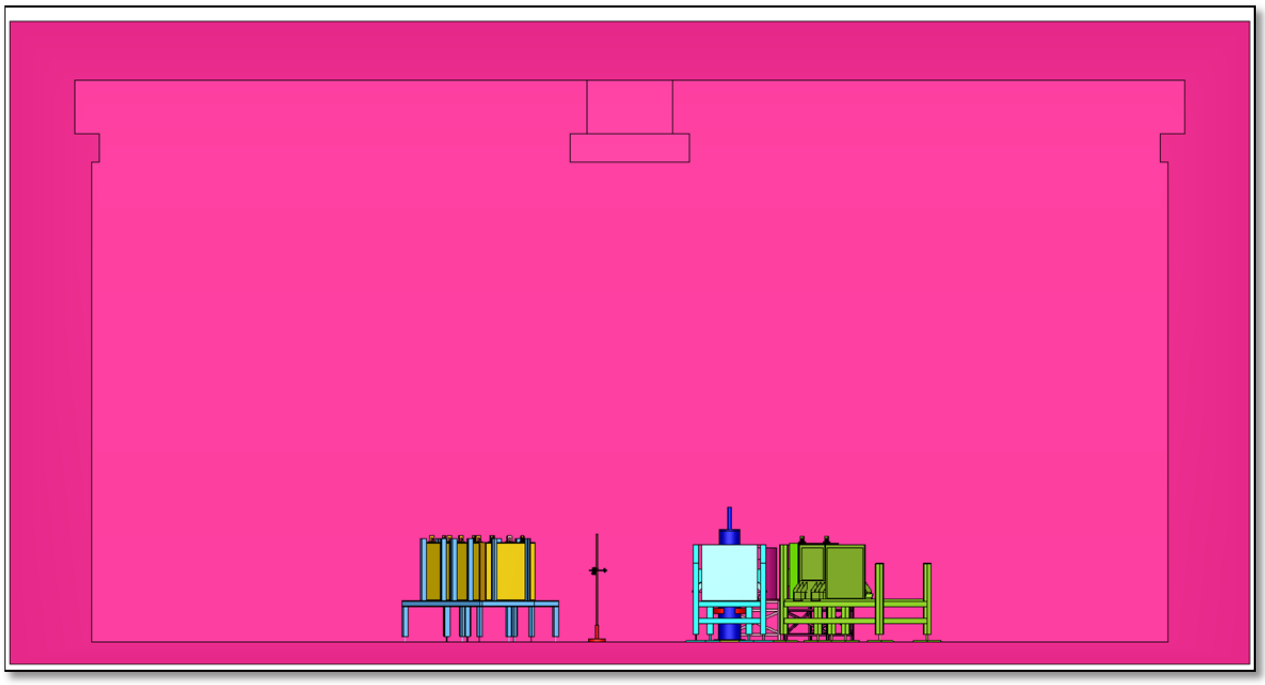


Figure 18: Side View of SILENE Reactor Cell Model (From Rear of Room)

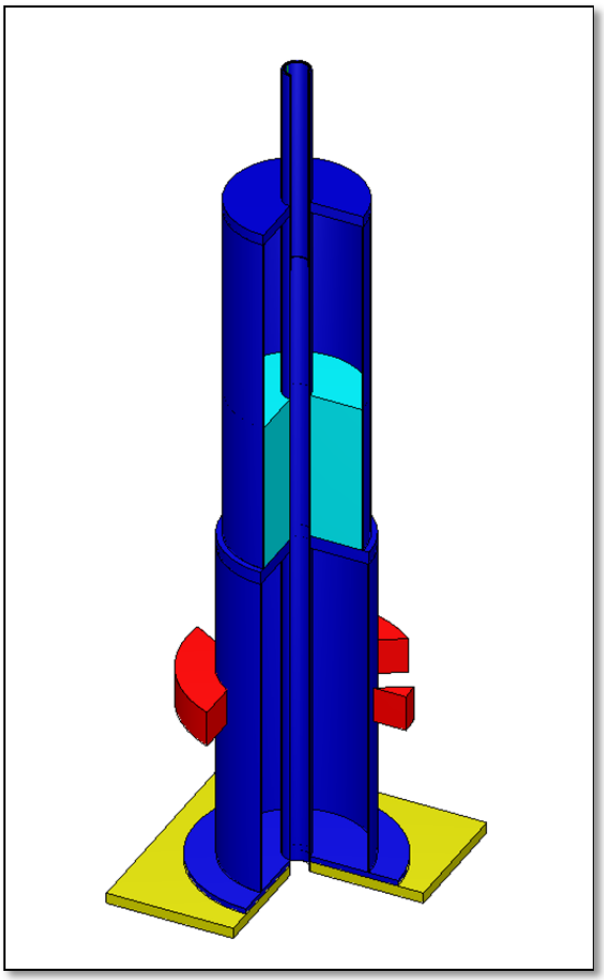


Figure 19: Computational Model of SILENE

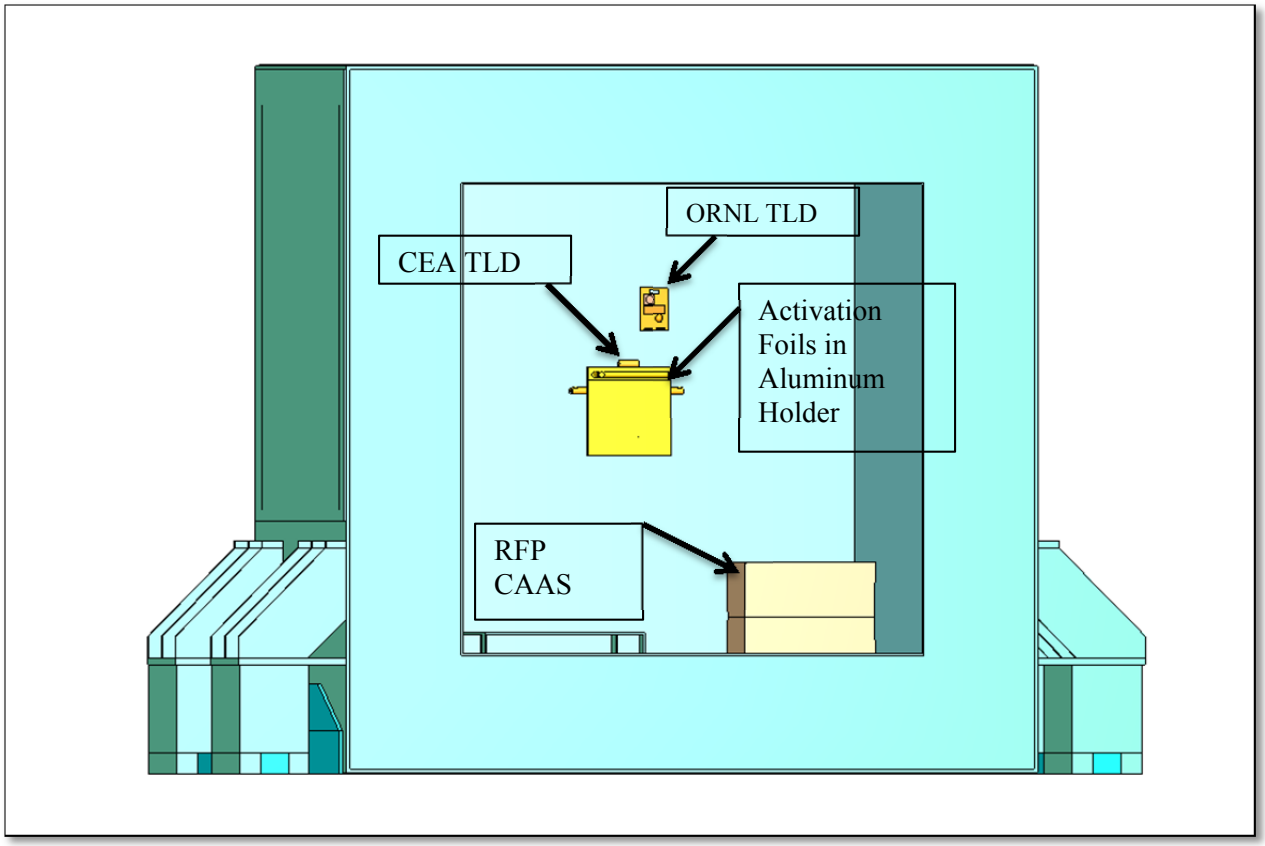


Figure 20: 3-D View of Collimator Box A Model



Figure 21: Interior View of Collimator Box A and Box B

Once the components are inserted into the box and the box has been placed onto the frame, we arrive at the computational model shown in figure 22 for Collimator Box A. Figure 23 shows a photograph of Collimator Box B in its pre-experiment configuration for comparison. Note that the high fidelity model for the collimator boxes includes such details as the wheel housing that allows the box to roll forward and backwards on its frame, the rail frame itself, the steel plates underneath the feet of each of the legs of the frame, the angle iron used to attach the wheel assembly to each collimator box and the small plates attached to the front of the frame used to prevent the box from moving forward past the front of the frame.

The computational model for Collimator Box B is not shown due to its similarity to the computational model for Collimator Box A. The only difference between the two is the presence of the CIDAS CAAS detector on the interior of Collimator Box B during the pulses and the shielding located on the frame between the reactor and the interior of Collimator Box B.

4.2.3. Scattering Box

Multiple annexes from reference [24] were used to construct the computational model for the scattering box. (Piot, June 2011) The scattering box is a series of concrete shields sitting on a steel support frame and situated in the reactor cell so that the primary radiation contributor to some of the foil activation is scattered. The model for the scattering box was assembled in a manner similar to the collimator boxes – the smaller components were defined as units and inserted into the larger model components as holes.

Figure 24 shows photographs of the front and back of the scattering box taken during the experiment. Figure 25 shows similar views of the computational model. The box is constructed of six shield blocks of concrete assembled on a steel frame. Inside the scattering box is a CIDAS CAAS detector, an RFP CAAS Detector, four sets of activation foils (1 full set and 3 partial sets), and several ORNL and CEA TLDs. (Piot, June 2011)

4.2.4. Free Field Location

The Free Field location is an aluminum stand placed in a stainless steel base filled with concrete designed to allow activation foils and TLDs to be placed in the radiation field with no shielding present between the activation foils and the reactor. During each of the pulses conducted during these experiments there was a complete set of activation foils, an ORNL TLD and a CEA TLD on the stand. (Piot, June 2011) Figure 26 shows a comparison of a photograph of the free field stand taken during the experiment and the computational model of the free field stand. Figure 27 shows a close-up of the activation foils and TLDs on the stand prior to pulse 1.

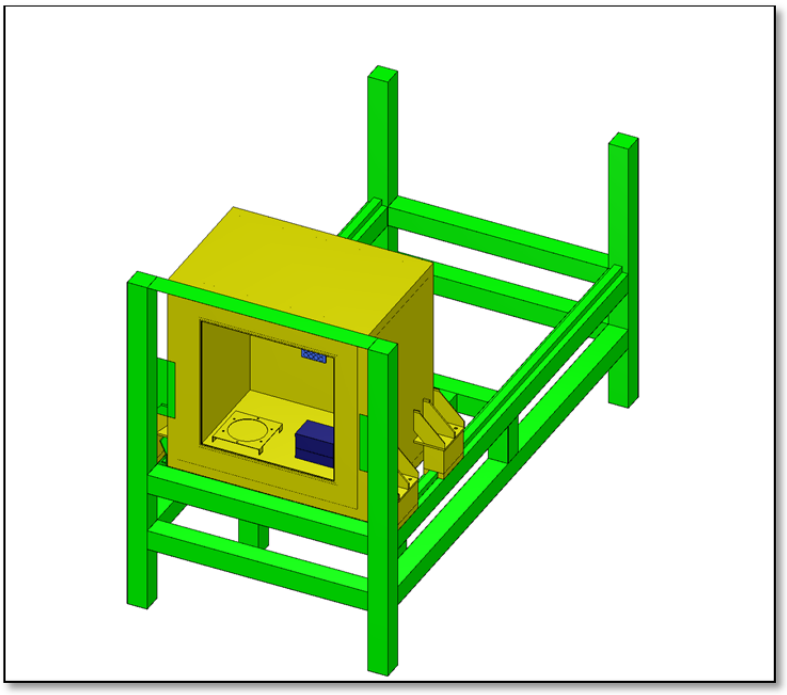


Figure 22: Collimator Box A Model



Figure 23: Collimator Box B (prior to experiment)

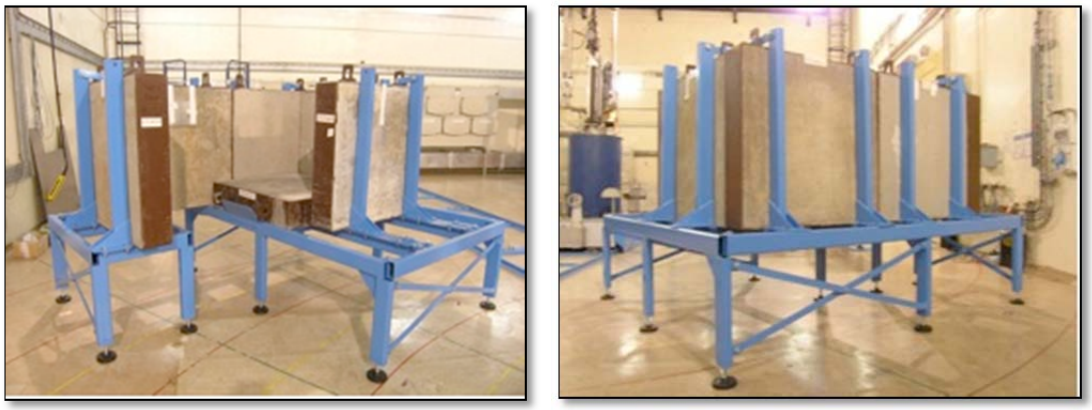


Figure 24: Front and Rear Views of Scattering Box

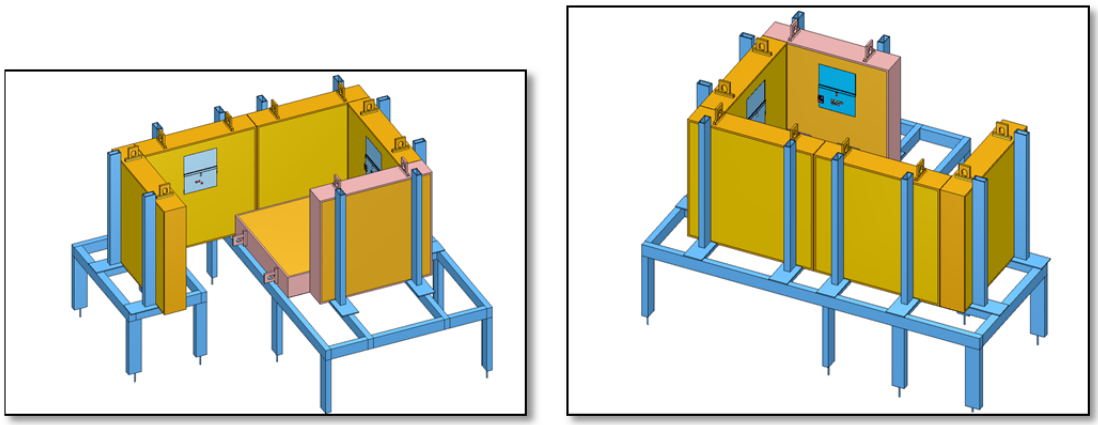


Figure 25: Scattering Box Model Front and Rear Views

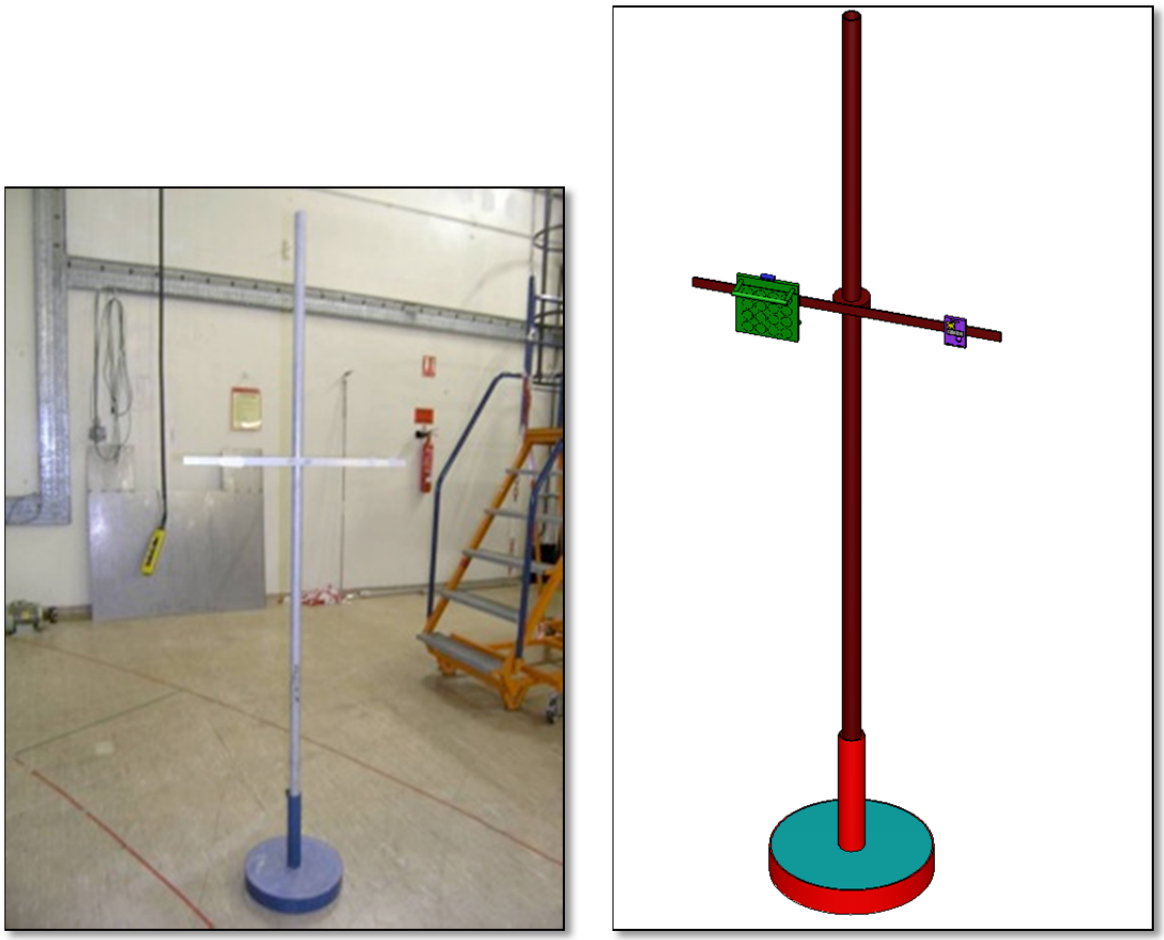


Figure 26: Free Field Stand



Figure 27: Close-Up View of Activation Foils on Free Field Stand

4.2.5. Diagnostic Stands

The diagnostic stands contain the instrumentation for operating and monitoring the reactor. The instrumentation is contained in a large polyethylene cylinder sitting on the top of a steel frame and is situated in the reactor cell as shown previously. (Piot, June 2011) Figure 28 shows a photograph of both diagnostic stands inside the reactor cell. Figure 29 shows the computational model used for the stands.

4.2.6. Activation Foils, Shields and TLDs

The activation foils for this experiment were represented as simple right, circular cylinders of material. The foils were placed in the various experiment locations in one of two ways. First, the foils were placed in Collimator Box A, Collimator Box B and the Free Field Location inside an aluminum frame. Figure 30 shows a typical frame used during the experiment side by side with the computational representation used in the model. Second, the foils were placed in the scattering box by taping them to an aluminum plate and hanging the plate from the shield block (see Figures 24 and 25).

The concrete shields used to construct the scattering box and used to block the opening of Collimator Box B were all 1m x 1m x 20 cm thick slabs of concrete contained in a steel frame with lifting points to allow their movement around the reactor cell. (Piot, June 2011) Figure 31 shows a photograph of a typical shield and the computational representation used in the model.

TLDs were supplied by ORNL and CEA Valduc for this experimental effort. A typical ORNL TLD is shown below in Figure 32 along with the computational model used. A typical CEA TLD is shown in its installed position on top of the aluminum frame for the activation foils in Figure 30.

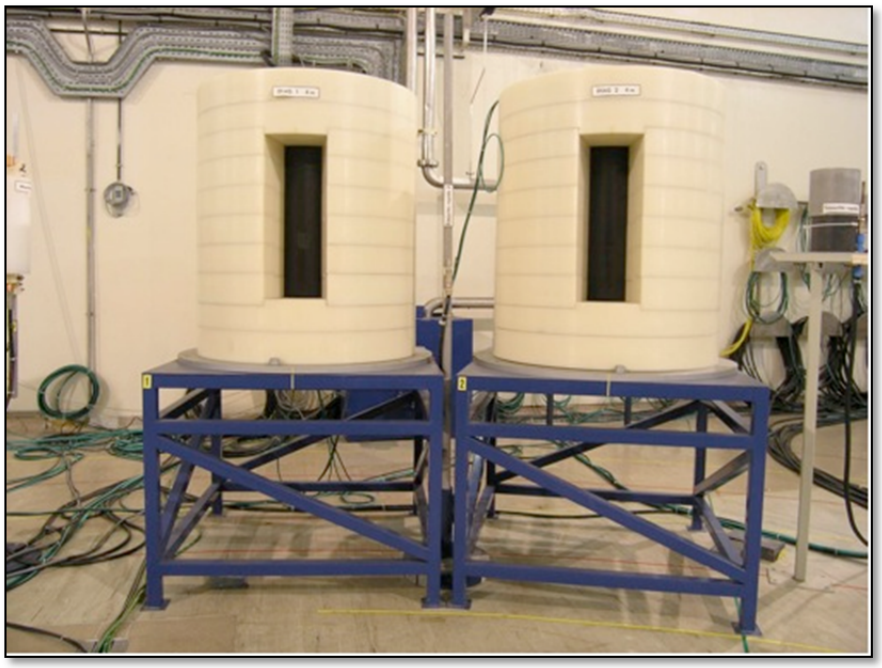


Figure 28: Diagnostic Stands A and B

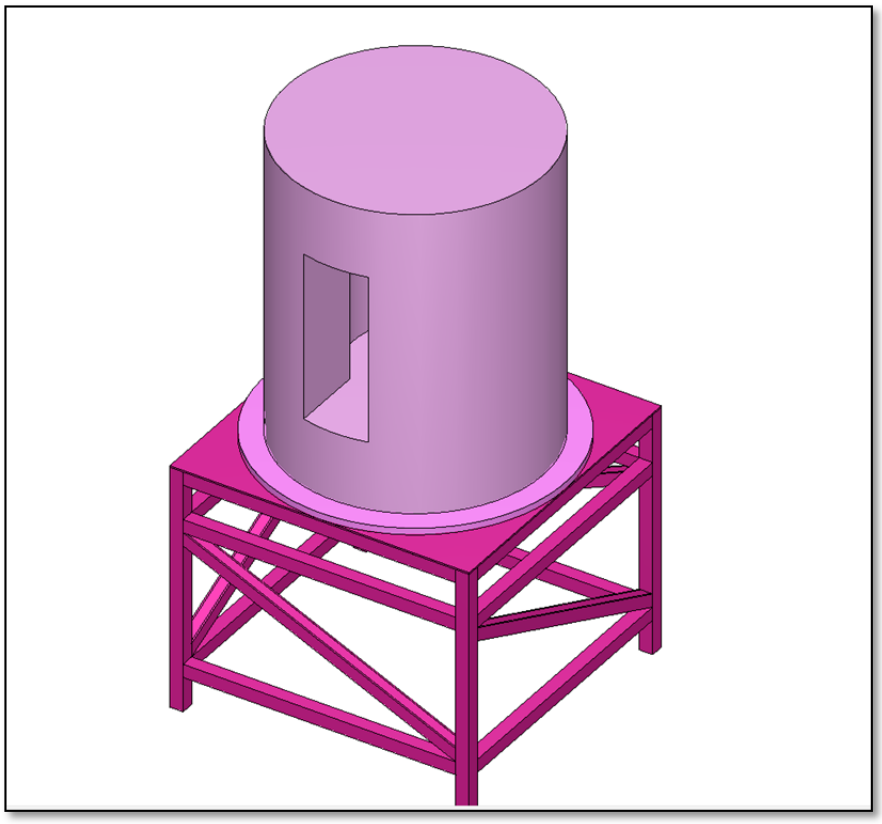


Figure 29: Computational Model of Diagnostic Stands A and B



Figure 30: Aluminum Frame for Activation Foils

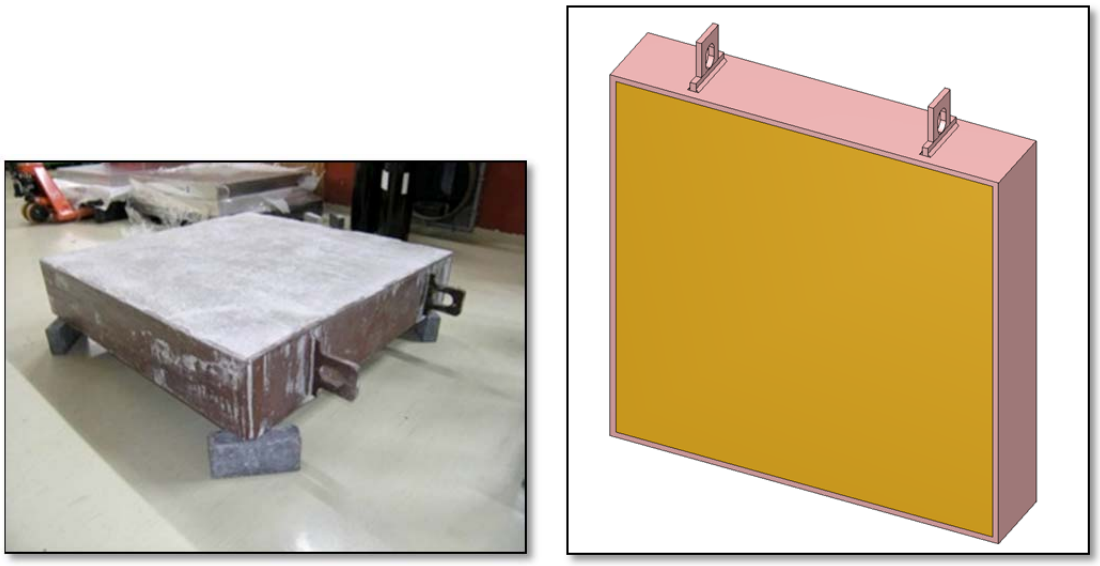


Figure 31: Concrete Shield Slab

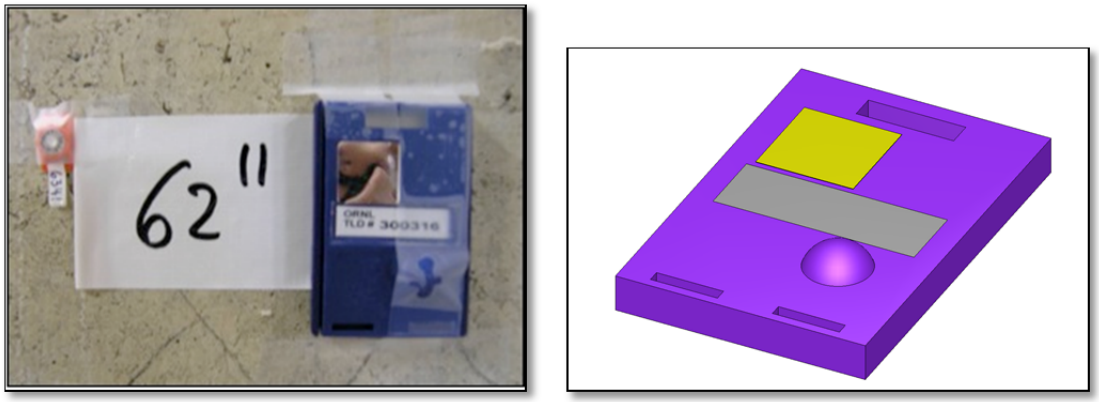


Figure 32: ORNL TLD

4.3 Computational Model Materials

Once the geometry for the computational model had been developed the material specifications for each of the geometry regions needed to be specified. Reference [24] was the primary technical reference for developing the material specifications used in the benchmark models. (Piot, June 2011) The sections that follow discuss the materials used in each of the major computational units of the final model.

4.3.1. Reactor Cell

The floor, walls, and ceiling of the SILENE reactor cell are made of concrete whose specification is given in reference [24] and is shown in Table 4 with a material density of 2.38 g/cm^3. (Piot, June 2011) The resulting benchmark model material description for the concrete is shown in Table 5.

The details of the room geometry are provided in Annex I and Annex II in reference [24]. (Piot, June 2011) The exit door is constructed of sheets of S235JR Stainless Steel (0.2 cm thick) sandwiched around a 4.6 cm thick air gap simulating the hollow core door. There are two of these doors – one on the interior of the room and one of the exterior of the 1.45 m thick reactor cell wall. There are two heavy concrete shields on a track system that are rolled in front of the exit doors when reactor operations are conducted. These have been modeled using the same concrete as was specified for the walls and ceiling of the reactor cell. The global room model has its outer boundary just beyond these large concrete shields. The material specification for the S235JR Stainless Steel was provided in reference [24] as shown in Table 6 with a material density of 7.85 g/cm^3. (Piot, June 2011)

Notice that the weight percent values for the constituents other than iron are given as a MAX which means that there could be a range of values for these making up different "recipes" for the iron and it still be called S235JR Stainless Steel. This forced a choice on how much of a particular constituent should be included in the benchmark model. When materials were modeled for this problem they used the MAX value when it was given and if a range of possible concentrations was given for an isotope then the mid-range value of the given range was used in the benchmark model.

In the case of the S235JR Stainless Steel, the resulting benchmark material specification is shown in Table 7.

Table 4: Original Material Specification for Reactor Cell Concrete

Element	ZAID	Weight %
H	1001	0.722
B10	5010	0.001
O	8016	48.090
Al	13000	2.916
Si	14000	27.518
Ca	20000	17.810
Fe	26000	2.943

Table 5: Benchmark Material Specification for Reactor Cell Concrete

Element	ZAID	Number Density [atoms/b-cm]	Element	ZAID	Number Density [atoms/b-cm]
H-1	1001	1.026545E-02	Ca-42	20042	4.120879E-05
H-2	1002	1.180663E-06	Ca-43	20043	8.598434E-06
B-10	5010	1.431418E-06	Ca-44	20044	1.328617E-04
O-16	8016	4.309243E-02	Ca-46	20046	2.547684E-07
Al-27	13027	1.548990E-03	Ca-48	20048	1.191042E-05
Si-28	14028	1.295096E-02	Fe-54	26054	4.414864E-05
Si-29	14029	6.579186E-04	Fe-56	26056	6.930392E-04
Si-30	14030	4.342123E-04	Fe-57	26057	1.600530E-05
Ca-40	20040	6.174376E-03	Fe-58	26058	2.130011E-06

Table 6: Original Material Specification for S235JR Stainless Steel

Element	Weight %
C	0.17 MAX
Mn	1.4 MAX
P	0.035 MAX
S	0.035 MAX
N	0.012 MAX
Cu	0.55 MAX
Fe	Balance

Table 7: Benchmark Material Specification for S235JR Stainless Steel

Element	ZAID	Number Density [atoms/b-cm]	Element	ZAID	Number Density [atoms/b-cm]
fe-54	26054	4.838934E-03	s-32	16032	4.901604E-05
fe-56	26056	7.596091E-02	s-33	16033	3.870095E-07
fe-57	26057	1.754269E-03	s-34	16034	2.193054E-06
fe-58	26058	2.334610E-04	s-36	16036	5.160127E-09
c	6000	6.691158E-04	n-14	7014	4.035361E-05
mn-55	25055	1.204690E-03	n-15	7015	1.474237E-07
p-31	15031	5.341888E-05	cu-63	29063	2.829352E-04
cu-65	29065	1.262263E-04			

4.3.2. SILENE

The details for the geometry of the SILENE reactor are provided in Annex II and Annex III of reference [24]. (Piot, June 2011) The reactor is a annular tank sitting 100 cm above the floor of the reactor cell. It is fueled with 93.5 weight percent enriched uranyl nitrate and has a cadmium control rod inserted in the center of the annulus. (Piot, June 2011)

The walls of the reactor are constructed of Z3-CN-1810 Stainless Steel whose material specification was given as shown in Table 8 with a density of 7.9 g/cm^3. (Piot, June 2011) Using the same methodology as previously described for the reactor room material specifications the final benchmark specification for the reactor steel is shown in Table 9.

The support plate for the reactor is identified as A42 steel. (Piot, June 2011) Determining the A42 material specification was made more complicated by the fact that there are four different recipes given in reference [24] that are all identified as A42 steel (page 29). (Piot, June 2011) The benchmark material specification was derived from these recipes by using the maximum weight percentage for each of the alloying elements present. The resulting benchmark model for A42 Steel at the given density of 7.85 g/cm^3 is shown in Table 10.

The fuel used in the reactor was modeled as a solution of uranyl nitrate at a uranium enrichment of 93.26857 weight percent ^{235}U and a concentration of 70.36 g U/liter. The details of the fuel composition were taken from Annex IV in reference [24]. (Piot, June 2011) It is noted in the reference that the actual concentration of the fuel for pulse 1 is not exactly known since a lab analysis was not performed until after pulse 2 had been conducted. The benchmark model used the value of concentration taken from the lab analysis performed just prior to pulse 1 and since the safety license for the reactor limits the maximum concentration to 71.0 g U/l the potential difference between the modeled concentration and the actual concentration is small. (Piot, June 2011) The benchmark model fuel specification is given in Table 11.

Lead was present around the outside of the reactor in pulse 1 in the lower lead shield. (Piot, June 2011) The benchmark model specification for the lead was taken from Annex III of reference [24]. (Piot, June 2011) Two lab samples from the lead shield were taken and given. The benchmark model used an average of the two lab samples for each of the isotopic constituents in the lead shield and also used the given density of 11.19 g/cm^3. The final benchmark material specification for the lead is given in Table 12.

The cadmium control rod was modeled using the standard composition for cadmium from the SCALE Standard Composition Library which uses that natural isotopic abundances and has a density of 8.642 g/cm^3. (Oak Ridge National Laboratory, June 2011)

Table 8: Original Material Specification for Z3-CN-1810 Steel

Element	Weight %
C	0.03 (max)
Mn	2 (max)
P	0.04
S	0.03
Si	1
Ni	9 – 11
Cr	17 – 19
Fe	Balance

Table 9: Benchmark Material Specification for Z3-CN-1810 Steel

Element	ZAID	Number Density [atoms/b-cm]
si-28	14028	1.562195E-03
si-29	14029	7.936070E-05
si-30	14030	5.237637E-05
fe-54	26054	3.430808E-03
fe-56	26056	5.385635E-02
fe-57	26057	1.243778E-03
fe-58	26058	1.655240E-04
c	6000	1.188313E-04
mn-55	25055	1.731948E-03
p-31	15031	6.143900E-05
s-32	16032	4.228135E-05
s-33	16033	3.338353E-07
s-34	16034	1.891734E-06
s-36	16036	4.451137E-09
ni-58	28058	5.518092E-03
ni-60	28060	2.125559E-03
ni-61	28061	9.239659E-05
ni-62	28062	2.946008E-04
ni-64	28064	7.502614E-05
cr-50	24050	7.155983E-04
cr-52	24052	1.379960E-02
cr-53	24053	1.564764E-03
cr-54	24054	3.895029E-04

Table 10: Benchmark Material Specification for A42 Steel

Element	ZAID	Number Density [atoms/b-cm]
fe-54	26054	4.928293E-03
fe-56	25056	7.736365E-02
fe-57	26057	1.786664E-03
fe-58	26058	2.377722E-04
c	6000	9.839938E-04
p-31	15031	1.144690E-04
s-32	16032	8.682842E-05
s-33	16033	6.855598E-07
s-34	16034	3.884839E-06
s-36	16036	9.140796E-09
n-14	7014	3.026521E-05
n-15	7015	1.105678E-07

Table 11: Benchmark Material Specification for Uranyl Nitrate Fuel

Element	ZAID	Number Density [atoms/b-cm]
h-1	1001	6.238135E-02
o-16	8016	3.559861E-02
u-234	92234	1.061105E-06
u-235	92235	1.669503E-04
u-236	92236	4.537933E-07
u-238	92238	1.166008E-05
n-14	7014	1.547022E-03

Table 12: Benchmark Material Specification for Lead

Element	ZAID	Number Density [atoms/b-cm]	Element	ZAID	Number Density [atoms/b-cm]
b-10	5010	6.202074E-10	b-11	5011	2.496413E-09
al-27	13027	1.998041E-08	ca-40	20040	1.629980E-09
ca-42	20042	1.087875E-11	ca-43	20043	2.269910E-12
ca-44	20044	3.507430E-11	ca-46	20046	6.725658E-14
ca-48	20048	3.144245E-12	fe-54	26054	2.010134E-09
fe-56	26056	3.155480E-08	fe-57	26057	7.287380E-10
fe-58	26058	9.698165E-11	mn-55	25055	1.226614E-10
ni-58	28058	5.901179E-08	ni-60	28060	2.273124E-08
ni-61	28061	9.881113E-10	ni-62	28062	3.150531E-09
ni-64	28064	8.023474E-10	cr-50	24050	9.854572E-11
cr-52	24052	1.900356E-09	cr-53	24053	2.154852E-10
cr-54	24054	5.363882E-11	cd-106	48106	3.746710E-11
cd-108	48108	2.667658E-11	cd-110	48110	3.743713E-10
cd-111	48111	3.836631E-10	cd-112	48112	7.232649E-10
cd-113	48113	3.662784E-10	cd-114	48114	8.611438E-10
cd-116	48116	2.245028E-10	mg-24	12024	1.095032E-09
mg-25	12025	1.386291E-10	mg-26	12026	1.526307E-10
ti-46	22046	5.807257E-11	ti-47	22047	5.237091E-11
ti-48	22048	5.189224E-10	ti-49	22049	3.808152E-11
ti-50	22050	3.646253E-11	v	23000	1.322846E-10
co-59	27059	5.717301E-10	cu-63	29063	2.823225E-07
cu-65	29065	1.259530E-07	zn	30000	1.030709E-09
as-75	33075	4.497219E-10	zr-90	40090	1.900330E-10
zr-91	40091	4.144159E-11	zr-92	40092	6.334433E-11
zr-94	40094	6.419384E-11	zr-96	40096	1.034193E-11
mo-92	42092	5.187317E-11	mo-94	42094	3.241634E-11
mo-95	42095	5.584179E-11	mo-96	42096	5.858120E-11
mo-97	42097	3.357532E-11	mo-98	42098	8.495680E-11
mo-100	42100	3.396164E-11	ag-107	47107	4.857757E-07
ag-109	47109	4.513096E-07	sn-112	50112	2.753183E-11
sn-114	50114	1.873300E-11	sn-115	50115	9.650333E-12
sn-116	50116	4.126936E-10	sn-117	50117	2.179840E-10
sn-118	50118	6.874443E-10	sn-119	50119	2.438128E-10
sn-120	50120	9.247290E-10	sn-122	50122	1.314148E-10
sn-124	50124	1.643395E-10	sb-121	51121	3.324593E-09
sb-123	51123	2.486616E-09	ba-130	56130	2.600766E-13
ba-132	56132	2.478089E-13	ba-134	56134	5.930239E-12
ba-135	56135	1.617382E-11	ba-136	56136	1.927021E-11
ba-137	56137	2.755831E-11	ba-138	56138	1.759149E-10
bi-209	83209	6.610425E-06	pb-204	82204	4.551832E-04
pb-206	82206	7.835653E-03	pb-207	82207	7.185391E-03
pb-208	82208	1.703685E-02			

4.3.3 Collimator Boxes

The stainless steel sheeting used to cover the exterior surfaces of the collimator boxes is made from Z3-CN-1810 stainless steel according to the benchmark material specification given in Table 9. (Piot, June 2011)

The lead and copper sheets on the interior of the collimator boxes were modeled using the compositions from the SCALE Standard Composition Library with densities of 11.344 g/cm^3 and 8.92 g/cm^3 respectively. (Oak Ridge National Laboratory, June 2011) The borated polyethylene (PPB9) is a borated plaster created by combining colemanite, polyethylene beads and gypsum. (Piot, June 2011) The final report on the materials contained in the PPB9 states that there is 1.29 weight percent of "other" materials as part of the final material specification. (Piot, June 2011) However, no information is given on what the "other" materials are so they were ignored in the benchmark model and the remaining weight percent distributions were re-normalized to 100 percent. The final benchmark material specification for PPB9 at a density of 1.02 g/cm3 is given in Table 13.

A detailed lab analysis of each of the activation foils used in the experiments was conducted and the results of this lab analysis are contained in reference [24]. (Piot, June 2011) The resulting benchmark material specifications for each of the foils is given in Tables 24 through 29 which are shown in Appendix A.

The frame holding the activation foils in the collimator boxes and on the free field stand is specified as AG3M Aluminum at a density of 2.68 g/cm^3. (Piot, June 2011) The original material specification for AG3M Aluminum is given in Table 14. The final benchmark specification for the AG3M Aluminum used in the foil holders was derived using the same choice methodology as previously discussed for other materials. The final benchmark specification is given in Table 15 and uses the specified density of 2.68 g/cm^3.

The materials discussed in the above sections were also used to construct the remaining major pieces of equipment used in the experiment (scattering box, free field stand and diagnostic stands). There are materials used in the high fidelity 3-D model that are not discussed in detail in this chapter due primarily to the fact that these materials did not advance to being present in the simplified model (see discussion in following chapter). The technical refereneces cited at the end of this dissertation contain all of the information necessary to construct reasonable material specifications for these materials. (Piot, June 2011)

Table 13: Benchmark Material Specification for PPB9

Element	ZAID	Number Density [atoms/b-cm]
h-1	1001	5.036765E-02
h-2	1002	5.792945E-06
b-10	5010	1.307085E-04
b-11	5011	5.261180E-04
o-16	8016	1.145205E-02
ca-40	20040	1.740333E-03
ca-42	20042	1.161527E-05
ca-43	20043	2.423588E-06
ca-44	20044	3.744892E-05
ca-46	20046	7.181001E-08
ca-48	20048	3.357118E-06
c	6000	2.140892E-02
s-32	16032	1.485526E-03
s-33	16033	1.172907E-05
s-34	16034	6.646473E-05
s-36	16036	1.563876E-07

Table 14: Original Material Specification for AG3M Aluminum

Element	Weight %
Al	Balance
Mg	2.6 – 3.6
Cr	< 0.3
Ti	< 0.15
Zn	< 0.2
Mn	< 0.5
Cu	< 0.1
Si	< 0.4
Fe	< 0.4

Table 15: Benchmark Material Specification for AG3M Aluminum

Element	ZAID	Number Density [atoms/b-cm]	Element	ZAID	Number Density [atoms/b-cm]
al-27	13027	5.673570E-02	si-28	14028	2.119839E-04
si-29	14029	1.076895E-05	si-30	14030	7.107275E-06
fe-54	26054	6.756860E-06	fe-56	26056	1.060682E-04
fe-57	26057	2.449578E-06	fe-58	26058	3.259939E-07
mn-55	25055	1.468867E-04	cr-50	24050	4.045999E-06
cr-52	24052	7.802306E-05	cr-53	24053	8.847190E-06
cr-54	24054	2.202253E-06	mg-24	12024	1.626009E-03
mg-25	12025	2.058500E-04	mg-26	12026	2.266409E-04
ti-46	22046	4.172507E-06	ti-47	22047	3.762843E-06
ti-48	22048	3.728451E-05	ti-49	22049	2.736153E-06
ti-50	22050	2.619828E-06	cu-63	29063	1.756263E-05
cu-65	29065	7.835243E-06	zn	30000	4.937089E-05

4.4 Final Model Assembly

The desired result of constructing the high fidelity 3-D model of the experiment was to compute activation rates in the foils and then to compare those computational results with measured dosimetry provided by the experimentalists.

Once the computational models for the problem geometry and materials were complete that information was combined into an input deck for the final High Fidelity 3-D model. This model was used as the starting point for the CAAS Analysis methodology described earlier in this dissertation. The fixed source transport portion of the calculation requires a spatial and energy dependent source specification which is obtained in the first step of the CAAS analysis methodology by overlaying a rectangular mesh on the fuel geometry portion of the problem and performing an eigenvalue calculation. The grid used was 36 x 36 x 42 for a total of 54,432 voxels each with a volume of ~1 cm^3. To ensure that the statistical error associated with the source tally in each voxel was acceptably low, the eigenvalue calculation was executed using 100 million particle histories. Figure 33 shows a Y-Z view of the resultant source tally at the center of the SILENE computational model.

The source tally shown in Figure 33 was then converted to a mesh source for the final MAVRIC calculation using the MT2MSM MAVRIC utility. The final estimates of reaction rates in the activation foils were obtained using the MAVRIC sequence in conjunction with the mesh source to execute the final fixed source transport. The results obtained using the High Fidelity 3-D model are discussed in the next chapter.

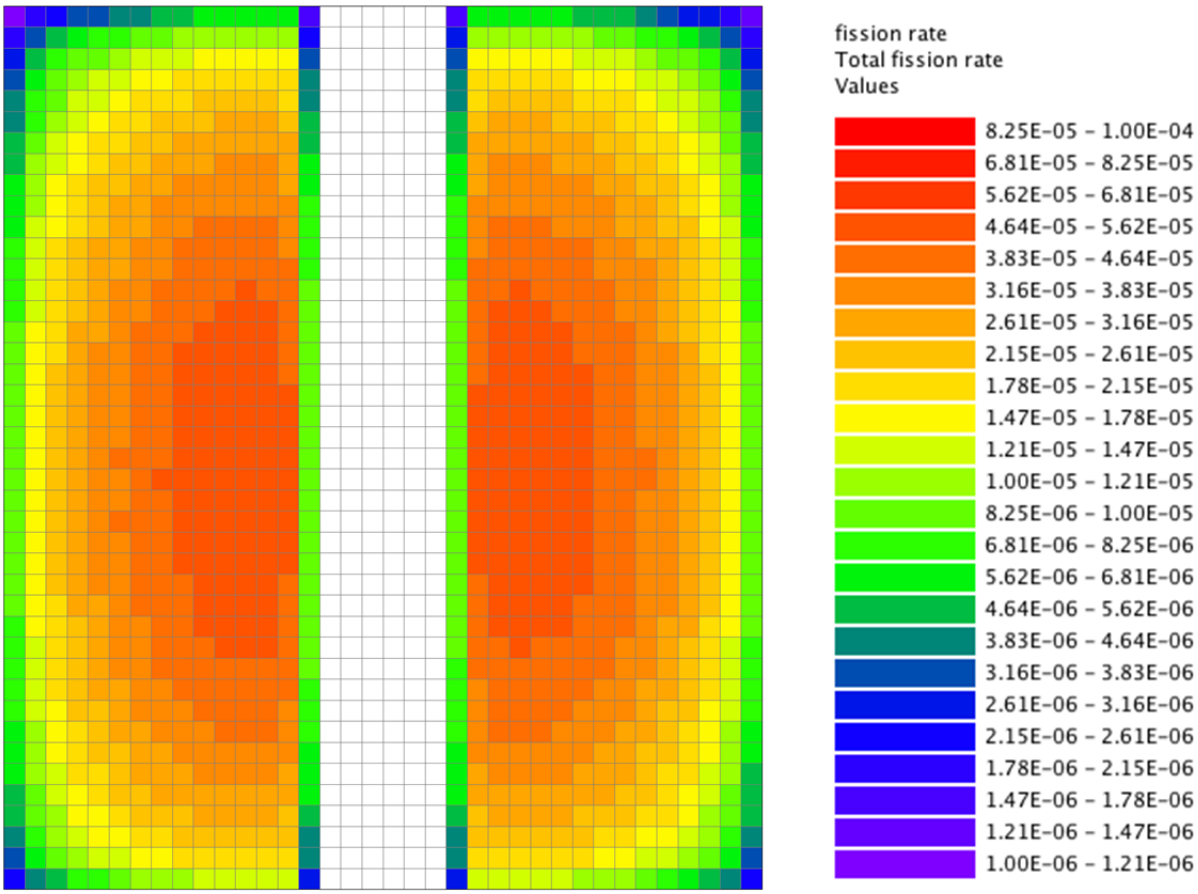


Figure 33: Y-Z KENO-VI Source Tally Profile at SILENE center

5. Results

5.1 Comparison of High Fidelity Model Results to Final Dosimetry

The primary objective of the fixed source benchmark to be published from these experiments is to provide data that can then be used to determine whether or not an end user's code is modeling reality correctly. The high fidelity 3-D model constructed for this dissertation has been used to provide a computational comparison of foil activity for the foils contained inside collimator box A as a result of being exposed during pulse 1. As has been noted in previous discussion there were many sets of foils and other radiation measuring devices (TLDs, etc.) deployed around the experiment and a complete dosimetry report for all three pulses is available (Chateauvieux & Piot, CAAS Test Dosimetry Report, Pulse 1, 6/16/2011), (Chateauvieux & Piot, CAAS Test Dosimetry Report, Pulse 2, 5/24/2012), (Chateauvieux & Piot, CAAS Test Dosimetry Report, Pulse 3, 5/31/2012) however, the results given in Table 16 are only for the foils exposed in Collimator Box A during pulse one. (Chateauvieux & Piot, CAAS Test Dosimetry Report, Pulse 1, 6/16/2011)

Two computational models have been developed in order to simulate the resultant activation of all of the foils in Collimator Box A. Recall from the information in Table 1 that the activation reactions being measured can be broken into two categories – threshold reactions and thermal reactions. The threshold reactions have all been included in a single simulation while the thermal reactions have all been included in a separate simulation. Both of these simulations were run every time a model change was being examined for its impact on the final estimate of reaction rate – except in those cases where it was obvious (either from previous results or by inspection) that the change being examined would have no impact upon the final answer.

Table 17 compares the pulse one computational results for the high fidelity 3-D model to the measured dosimetry results for the activation foils in Collimator Box A. The computed uncertainties shown are Monte Carlo uncertainties only. Also, the C/E values are not final because the total uncertainty for the computational results is not yet known. The C/E ratios shown in Table 17 are used to judge the performance of the computational model and will be updated later in this chapter.

The first result of note in Table 17 is for the iron foil. The reaction for ^{56}Fe activation is looking for the presence of ^{56}Mn and it turns out that in addition to the threshold (n,p) iron reaction generating this product there is a thermal (n,γ) reaction producing ^{56}Mn. The Manganese makes up 0.3 percent of the material in the foil but accounts for almost 95 percent of the response seen in the foil so properly accounting for this reaction turned out to be important to the computed response estimates aligning with the measured responses. The computed ^{56}Fe activation compares very well when both of these components are accounted for in the simulation (C/E = 1.0055).

An examination of the ratio of the computed to measured values (C/E) for each of the remaining reactions shows good agreement between the high fidelity computed results and the measured results in all but two instances.

Table 16: Pulse One Measured Dosimetry Results

Reference Foil	Measured Reaction	Activity [Bq/g]	Uncertainty (± σ) [Bq/g]	Relative Uncertainty [%]
Au05–A10	$^{197}Au(n,\gamma)^{198}Au$	$1.812x10^{5}$	2850.0	1.5728
Ni011	$^{58}Ni(n,p)^{58}Co$	14.36	0.22	1.5320
In005	$^{115}In(n,n',\gamma)^{115m}In$	8030.0	125.0	1.5567
In005	$^{115}In(n,\gamma)^{116}In$	$9.11x10^{6}$	$1.75x10^{5}$	1.9210
Fe021	$^{54}Fe(n,p)^{54}Mn$	0.2062	0.0041	1.9884
Fe021	$^{56}Fe(n,p)^{56}Mn$	2310.0	30.5	1.3203
Mg032	$^{24}Mg(n,p)^{24}Na$	61.1	1.15	1.8822
Co013	$^{59}Co(n,\gamma)^{60}Co$	66.1	0.85	1.2859

Table 17: Comparison of Calculated and Measured Results

Foil	Reaction	Computed Response [Bq/g]	Computed Uncertainty (± σ)	Computed Relative Uncertainty (± %σ)	Measured Response [Bq/g]	Measured Uncertainty (± σ)	Measured Relative Uncertainty (± %σ)	Ratio of Computed to Measured Response (C/E)
Threshold Reactions								
Ni	$^{58}Ni(n,p)^{58}Co$	13.592	0.121	0.8902	14.36	0.22	1.5320	0.9465
Fe	$^{54}Fe(n,p)^{54}Mn$	0.20415	0.002	0.9797	0.2062	0.0041	1.9884	0.9901
Fe[1]	$^{56}Fe(n,p)^{56}Mn$	120.30	1.395	1.1596	N/A	N/A	N/A	N/A
Mg	$^{24}Mg(n,p)^{24}Na$	66.780	0.7095	1.0624	61.1	1.15	1.8822	1.0930
In	$^{115}In(n,n',\gamma)^{115m}In$	7592.00	88.000	1.1591	8030	125.0	1.5567	0.9455
Thermal Reactions								
Au	$^{197}Au(n,\gamma)^{198}Au$	76491.0	804.50	1.0518	$1.812x10^5$	2850.0	1.5728	0.4221
Fe[2]	$^{55}Mn(n,\gamma)^{56}Mn$	2202.30	25.10	1.1397	N/A	N/A	N/A	N/A
Co	$^{59}Co(n,\gamma)^{60}Co$	71.0130	0.715	1.0069	66.1	0.85	1.2859	1.0743
In	$^{115}In(n,\gamma)^{116}In$	$1.17200x10^7$	$1.19500x10^5$	1.0196	$9.11x10^6$	$1.75x10^5$	1.9210	1.2865
Threshold + Thermal Reactions								
Fe	1 + 2	2322.6	25.1387	1.0824	2310	30.5	1.3203	1.0055

First, the computed activation of the gold foil does not compare to the measured value very closely. The discrepancy in the two values could be due to bad nuclear data being used by the SCALE simulation, an error in the computational model, or due to the reported measurement result being incorrect. Given that the remaining computed thermal foil reactions are all in good agreement with their measured results it was judged to be unlikely that the computational model was incorrect. It was further judged unlikely that the nuclear data for the gold reaction being simulated was incorrect because this is a commonly used activation foil reaction.

In an effort to determine if the measurement for the gold foil activation in Collimator Box A for pulse 1 was bad, the measured gold activation data from all three pulses was examined. Table 18 shows the measured dosimetry data for the gold activation foil for all three pulses in collimator box A, the free field location and scattering box locations 3 and 4. (Chateauvieux & Piot, CAAS Test Dosimetry Report, Pulse 1, 6/16/2011), (Chateauvieux & Piot, CAAS Test Dosimetry Report, Pulse 2, 5/24/2012), (Chateauvieux & Piot, CAAS Test Dosimetry Report, Pulse 3, 5/31/2012) These four locations were chosen to be compared to each other due to the fact that the measured activation rates at each of these locations should be fairly similar and so ratios of their activation rates should be about one in most cases.

In comparing the free field location to the scattering box locations, it can be seen that the ratios are in fact all reasonably close to one for all three pulses. The free field location has the higher activation rate in all cases, which can be attributed to the scattering box locations being further away from the reactor.

The results seen when comparing the free field location to the scattering box locations should also be seen when comparing the collimator box A activation rates to the scattering box rates. Examining Table 18 reveals that for pulses 2 and 3 this is in fact true. However, the pulse one values do not compare well – rather than being close to one the ratios are more on the order of 4.5 to 5.

Finally, the free field activation and the activation at the collimator box should be essentially identical due to the fact that they are spaced the same distance from the reactor. Table 18 shows that for pulses 2 and 3 the rations for the free field and collimator box locations are almost exactly 1.0. The value for pulse 1 however results in a ratio of 2.6.

All of these comparisons seem to indicate that the measured value for the gold foil activation rate for pulse 1 in collimator box A is incorrect. Therefore there should be no expectation that the C/E for this location would be close to 1.0 and in fact it is not.

The second disagreement noted in the comparison of measured to calculated results from the high fidelity model in Table 17 was the thermal indium reaction. The C/E for this reaction is 1.2865. In an effort to determine if this difference could be considered acceptable or not for a benchmark evaluation, the shielding benchmarks currently in the handbook (and discussed in Chapter 1) were re-visited. A review of these benchmarks reveals that errors between measured and computed values of up to 30% are not uncommon and they are all still considered as acceptable for use as shielding benchmarks. (Briggs, 2012) Therefore, the indium result obtained in this benchmark will be considered acceptable for use.

Table 18: Comparison of Measured Gold Foil Results

Select Measured Dosimetry for Gold Activation Foil [Bq/gram]					
Pulse	Coll A	Free Field		SB3	SB4
1	1.81E+05	6.95E+04		4.46E+04	3.87E+04
2	6.88E+04	6.43E+04		4.37E+04	3.90E+04
3	6.51E+03	5.55E+03		3.91E+03	3.67E+03
Comparisons of Measured Dosimetry					
Pulse	A/FF	A/SB3	A/SB4	FF/SB3	FF/SB4
1	2.60	4.06	4.68	1.56	1.80
2	1.07	1.57	1.76	1.47	1.65
3	1.17	1.66	1.77	1.42	1.51

5.2 Simplification of High Fidelity 3-D Model

The results obtained with the high fidelity 3-D model compare with the measured results quite well. The next step in determining the "best" benchmark model was to systematically evaluate the detail in the high fidelity model to determine if it was contributing to the final computed answer.

The method employed was to remove portions of the geometry from the computational model, re-run the simulation and compare the new computed results to the high fidelity results. If the new results were statistically equivalent to the high fidelity results then it was determined that the portion of the geometry removed was not contributing to the final estimate of activation and was eliminated. The final result was a simplified model for the thermal and threshold simulations.

5.2.1. Thermal Reactions

The first attempt at simplifying the high fidelity 3-D model was to take everything out of the model geometry except for SILENE and Collimator Box A. The computed result for all of the thermal reactions was far less than the high fidelity model.

The next step was to evaluate the contribution of scattering from various portions of the model. First, the floor of the model was added back in and the results compared to the high fidelity results. While the new computed estimate was much closer to the high fidelity result it still was not statistically the same answer.

The next progression of simulations sought to evaluate whether or not the scattering box, collimator box B, the free field location, the diagnostic stands, the room ceiling, or the room rear wall (opposite from collimator box A) were major contributors to the final estimate. These components were added back into two different ways and new simulations were run. First, the case with only SILENE and collimator box A was re-run with each of the pieces of equipment individually added back into the problem geometry. The computed estimate of activation rate for all reactions was not statistically different from the case with only SILENE and collimator box A indicating that none of the evaluated model components were significant individual contributors to the final estimate of response. Second, the case with SILENE, collimator box A and the entire floor was re-run with each piece of equipment added back into the problem geometry. Again, the computed estimates of reaction rate were not statistically different from the case with SILENE, collimator box A and the floor alone confirming that the evaluated model components were not significant individual contributors to the final estimate of response. Based on the results of these comparisons, the Diagnostic Stands, the Scattering Box, and Collimator Box B were all removed from the computational model of Pulse 1. Although the room ceiling and rear wall were indicated to be unimportant individual contributors these components were not removed from the computational model. It was judged that their contribution to the estimate of response could be significant when included as part of the whole room. In other words, when the entire room is modeled (floor, ceiling and walls) its contribution to the final estimate of response could be significant and at this point has not yet been evaluated.

At this point in the simplification process the computational model included Collimator Box A, SILENE, and the floor of the reactor cell. Although the ceiling and the rear wall of the reactor cell are not by themselves significant individual contributors to the final estimate of response (based on the comparisons discussed above), the effect of adding them in as part of having the entire reactor cell present in the model (floor, walls and ceiling) was not known and therefore one additional case was run with SILENE, collimator box A and the entire reactor cell modeled. The computed estimate of response from this simulation was statistically the same as the high fidelity model indicating that room scatter was an important contributor to the final estimate of thermal response.

The fact that scattering from the walls and ceiling was important was somewhat unexpected. Scattering from the floor or ceiling directly in between SILENE and collimator box A being a contributor was quite intuitive. Scattering from the walls, floor and ceiling that was not directly between SILENE and collimator box A being a significant contributor was surprising.

At this point in the simplification process the geometry model includes SILENE, collimator box A, and the room (walls, floor and ceiling). The next simplification examined was the detail associated with the collimator box. The support frame was removed from underneath collimator box A and the simulation was re-run with the results being statistically the same as the simulation that included the frame indicating that the frame could be removed from the computational model. Next the equipment from the interior of the collimator box (CAAS detectors, stands, TLDs) was removed leaving only the foils inside their aluminum frame on the interior wall. This result was again statistically the same indicating that these components could be removed from the computational model.

The final simplified model includes the reactor cell in a simplified sense. The details of the overhead crane rail system and the exit doors in the rear wall of the room were removed in the final model. The room was included as a simple concrete cuboid using the benchmark material specification of the room concrete. In total, the final simplified model for the thermal reactions includes SILENE, the box portion of collimator box A, the activation foils inside their aluminum frame, and the reactor cell ceiling, floor and walls.

Finally, once all of the model simplifications were known, a final input deck was created using the simplified model geometry and the benchmark material specifications. This final input deck was then tested to ensure that it was in fact producing consistent results by running it in three different sequences. First, the simplified model was used with the mesh source and importance map developed with the high fidelity model. Second, the simplified model was used to create a new source but still used the detailed importance map. And finally, the simplified model was used to create a simplified mesh source and importance map. In all three cases the computed response was statistically equivalent to the high fidelity computed response and confirmed that the simplified computational model specifications were correct.

Table 19 shows a comparison of the results obtained with the thermal high fidelity model, the final simplified thermal model and the measured results. The C/E values shown compare the simplified result to the measured result. Comparing the high fidelity C/E in table 17 to the simplified C/E in Table 19 shows that the simplified model is a reasonable approximation to the high fidelity model. Figure 34 shows a visual comparison of select direct perturbation results as discussed above. In order to present all of the thermal foil perturbation results on the same scale some of the computed results needed a scaling factor to be applied. The scaling factors applied were 1/1000 for the gold foil results, 1/100 for the iron-56 foil results and 1/100,000 for the indium foil results. The scaling factor applied is shown on the horizontal axis title for each foil. The complete computational results for the thermal foil reactions are given in Appendix B.

Table 19: Comparison of Calculated and Measured Thermal Foil Responses

Foil	High Fidelity Model Calculated Response [Bq/g]	Computed Uncertainty (± σ)	Computed Relative Uncertainty (± %σ)	Simplified Model Calculated Response [Bq/g]	Computed Uncertainty (± σ)	Computed Relative Uncertainty (± %σ)	Measured Response [Bq/g]	Measured Uncertainty (± σ)	Measured Relative Uncertainty (± %σ)	Simplified C/E
Gold	7.6491×10^{4}	804.50	1.0518	7.7183×10^{4}	867.00	1.1233	1.812×10^{5}	2850.0	1.5728	0.426
Cobalt	71.013	0.715	1.0069	69.614	0.64	0.9194	66.1	0.85	1.2859	1.0532
Indium	1.172×10^{7}	1.195×10^{5}	1.0196	1.1708×10^{7}	1.1×10^{5}	0.9395	9.11×10^{6}	1.75×10^{5}	1.9210	1.2852
Iron-56	2.2023×10^{3}	25.10	1.1397	2.2501×10^{3}	24.05	1.0688	N/A	N/A	N/A	N/A

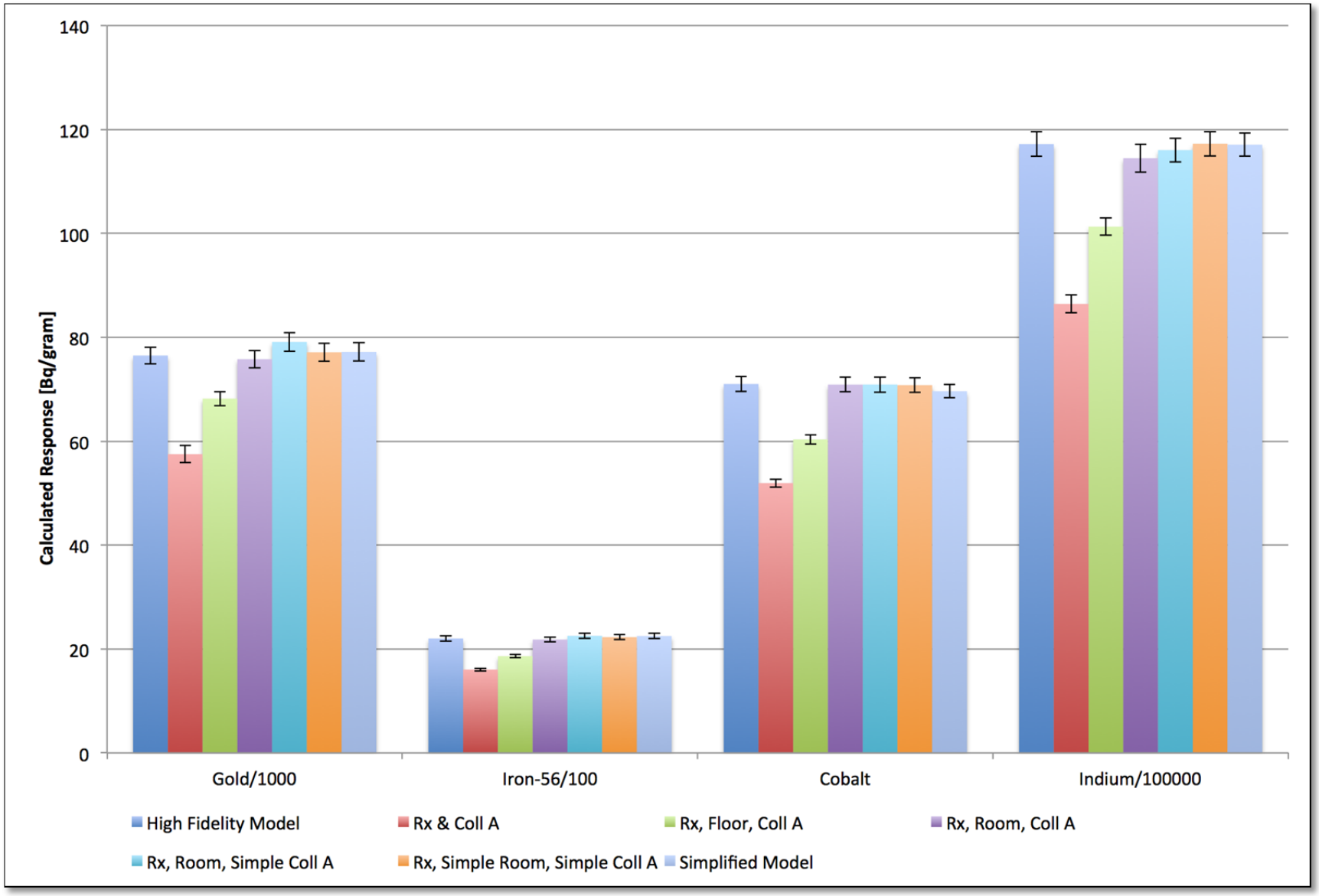


Figure 34: Comparison of Calculated Thermal Foil Responses

5.2.2. Threshold Reactions

The simplification of the threshold reactions model began in the same way as the thermal model simplification – by removing all portions of the model except SILENE and collimator box A. Re-running the simulations with these simplifications implemented gave results that were statistically the same as the high fidelity model in some cases (Iron foil and Magnesium foil) and statistically different in other cases (Nickel foil and Indium foil).

The next progression of simplifications proceeded in a slightly different manner than the simplifications for the thermal reactions. The major model components were individually added back to the simplified case and the simulation was re-run. All of the computed results were statistically the same as the simplified model. The conclusion was that the scattering box, the diagnostic stands, collimator box B, and the free field location could be eliminated from the high fidelity computational model. Next, the effect of removing the support frame and the internal equipment (CAAS, TLDs, etc.) from collimator box A was studied. These computed results were again statistically the same as the high fidelity model and justified removing these model components from the high fidelity model.

The simplified model for the threshold reactions at this point included SILENE and a simplified model of collimator box A. It was decided that having dissimilar models for the thermal and the threshold reactions would not be ideal even if the computational results supported that decision and so the effect of adding the room back to the simplified model one surface at a time was also studied in a series of simulations. The computational results were again statistically the same as the simplified case indicating that the surfaces were not major contributors to the final estimate of response when considered individually.

The final simulation added the room to the model containing SILENE and the simplified collimator box A model. The result was statistically the same as the high fidelity result and so it was decided that the simplified computational model for the threshold reactions would consist of the same geometry as the computational model for the thermal reactions – SILENE, the simplified collimator box A and the simplified room model.

The simplified model for the threshold reactions was tested in exactly the same manner as was the thermal simplified model. It was used in conjunction with the detailed importance map and source, it was used to produce a simplified mesh source which was used with the original detailed importance map, and finally a new simplified mesh source and a new simplified importance map were generated. In all cases the simulation results were statistically the same.

Table 20 shows a comparison of the results obtained with the threshold high fidelity model, the final simplified threshold model and the measured results. Again, the C/E compares the computed result obtained from the simplified model to the measured result and again the C/E values are similar to those obtained with the high fidelity model indicating that the simplified model is a reasonable approximation. Figure 35 shows a visual presentation of the perturbation studies done for the threshold reactions. Note that scaling factors have been applied here just as for the thermal results figure to allow comparison on a single scale. Finally, appendix B gives the complete set of computed threshold foil results.

Table 20: Comparison of Calculated and Measured Threshold Foil Responses

Foil	High Fidelity Model Calculated Response [Bq/g]	Computed Uncertainty (± σ)	Computed Relative Uncertainty (± %σ)	Final Simplified Calculated Response [Bq/g]	Computed Uncertainty (± σ)	Computed Relative Uncertainty (± %σ)	Measured Response [Bq/g]	Measured Uncertainty (± σ)	Measured Relative Uncertainty (± %σ)	Simplified C/E
Nickel	13.592	0.121	0.8902	13.325	0.1205	0.9094	14.360	0.22	1.5320	0.9279
Iron-54	0.2042	0.002	0.9794	0.2039	0.001895	0.9294	0.2062	0.0041	1.9884	0.9888
Iron-56	120.30	1.395	1.1596	122.57	1.38	1.1259	N/A	N/A	N/A	
Iron-56 (total)	2322.60	25.1387	1.0824	2372.67	24.0896	1.0153	2310.00	30.5	1.3203	1.0271
Magnesium	66.780	0.7095	1.0624	66.134	0.684	1.0343	61.100	1.15	1.8822	1.0824
Indium	7592.00	88.0	1.1591	7402.1	82.85	1.1193	8030	125.0	1.5567	0.9218

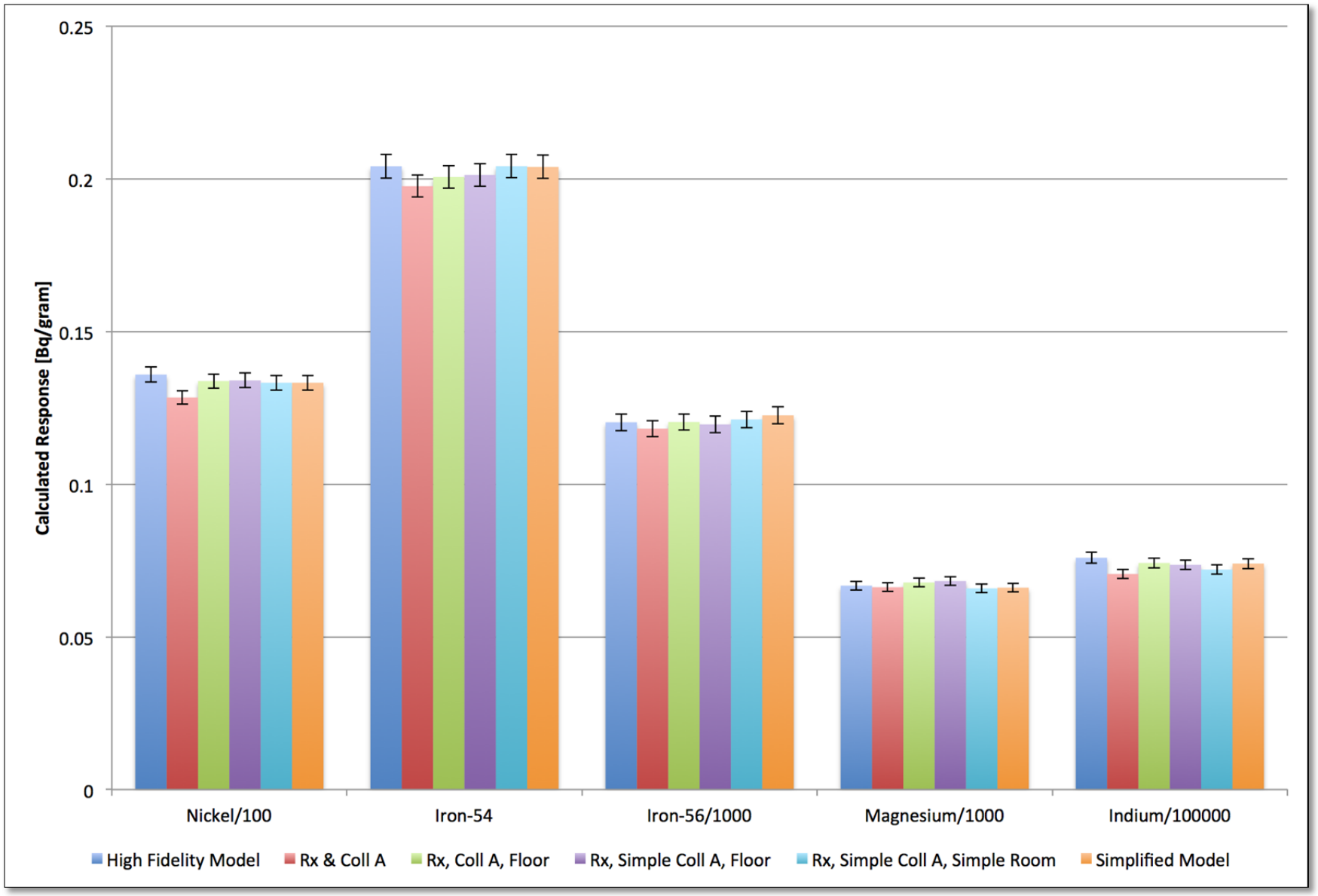


Figure 35: Comparison of Calculated Threshold Foil Responses

5.3 Sensitivity Coefficients for Simplified 3-D Model

Once the simplified model for computing the activation rates in the foils had been determined the next step in the benchmark process was to determine sensitivity coefficients for important parts the models. The French technical report (Piot, June 2011) noted items in the experimental setup that had uncertainties associated with them. These known uncertainties need to be evaluated to determine if the computational model is in any way sensitive to the known variations in the input parameters. The complete list of known uncertainties is shown in Appendix C.

It was decided that the uncertainties associated with parameters that could affect the activation foils directly were the best candidates to be studied for model sensitivities and those parameters were identified as follows:

- The thickness of the activation foil
- The number density of ^{235}U in the uranyl nitrate fuel
- The density of the PPB9 polyethylene in the collimator boxes
- The amount of impurities contained in the activation foils
- Composition and Density of Reactor Cell concrete (walls, floor, and ceiling)

The remaining uncertainties listed in Appendix C were not studied because they impacted aspects of the computational model that had already been eliminated by this point in the study, the given uncertainties were so small that their variations would have no discernable impact on the computed response, or the uncertainty associated with the parameter was simply unknown (as was the case for the composition and density of the concrete in the reactor cell).

The method for determining the sensitivity coefficient for each of the above identified model parameters was to start with the simplified model and change the identified parameter with a large enough perturbation to see a statistically different computed response in the foil. Using the simplified model result as the zero change point the resulting response was plotted versus the amount of parameter change, a straight line was fitted to the data points and the slope of the fitted line was the sensitivity of the identified parameter change. The results are shown in Table 21. Note that the uncertainty in the final computed response was propagated into the estimates of the sensitivity coefficient. Also note that the sensitivity coefficients shown in Table 21 have been normalized so that the values are more easily comparable. The sensitivity coefficients, S, reported in Table 21 are defined as $\frac{\Delta R/R}{\Delta x/x}$ (percent change in response R for a given 1 percent change in parameter x) rather than the un-normalized form shown in equation (2-95).

Finally, it is worth noting that no sensitivity coefficients were computed for the threshold foil reactions. The simplified model for the threshold foils was changed as described above for each of the listed parameters. The results indicated that the threshold foils were insensitive to changes in these parameters and so no sensitivity coefficient could be computed. As has been previously stated, the remaining known uncertainties were not studied because they either did not affect the foils located in collimator box A or had associated uncertainties that were so small as to render the potential range of real changes too small to generate a sensitivity coefficient. The complete list of computational results for the threshold foils is given in Appendix B.

Table 21: Sensitivity Coefficients for Thermal Foil Reactions

Parameter	S	σ_s	$\%\sigma_s$	n	R^2
Gold Foil					
Foil Thickness	0.6816	0.0099	1.45%	3	0.9925
^{235}U Number Density	-0.2099	0.0290	13.83%	3	0.9899
PPB9 Density	-0.2152	0.0319	14.80%	2	1.0000
Cobalt Foil					
Foil Thickness	0.7497	0.0112	1.49%	3	0.9952
^{235}U Number Density	-0.3282	0.0295	8.98%	4	0.8714
PPB9 Density	-0.2664	0.0280	10.52%	3	0.9630
Indium Foil					
Foil Thickness	0.4290	0.0064	1.49%	3	0.9648
^{235}U Number Density	-0.2207	0.0272	12.34%	3	1.0000
PPB9 Density	-0.0948	0.0280	29.53%	2	1.0000
Iron Foil (Iron-56)					
Foil Thickness	Not Sensitive				
^{235}U Number Density	-0.3598	0.0351	9.76%	3	0.9975
PPB9 Density	-0.1307	0.0474	36.28%	2	1.0000

In looking at the results in Table 21 it is clear that none of the parameters studied were overly sensitive to change as indicated by the fact that all of the computed sensitivity coefficients are less than 1.0. In other words, none of the examined parameters cause more than a 1 percent change in the activation foil response when the parameter underwent a one percent change.

The thickness of the activation foil was the most sensitive parameter studied for all of the thermal reactions. This study was done by changing the thickness of the foil in the simplified model and re-running the simulation. For the Iron-56 reaction, since the iron foil was 0.3 cm thick (which occupied almost all of the 0.33 cm available in the frame holder) the perturbations examined were all in the negative direction – in other words the thickness of the foil was decreased several times to obtain multiple data points. The cobalt foil exhibited the highest sensitivity of the four foils examined with a sensitivity coefficient of 0.7497, which means that for a 1 percent change in the thickness of the cobalt foil the activation will experience a change of 0.7497 percent. The gold foil was next with a sensitivity coefficient of 0.6816 and the Indium foil was next with a coefficient of 0.4290. The thermal iron-56 reaction showed no statistically significant differences in the computed response for changes in thickness ranging from 2 percent to 50 percent of the foil thickness and so no sensitivity coefficient was computed.

Changing the number density of the ^{235}U present in the uranyl nitrate fuel by 1 percent did not produce significant changes in the computed response as indicated by the results shown in Table 21. The simplified models were modified by increasing and decreasing the number density of the ^{235}U present in the computational model of the fuel and re-running the simulation. In this case since the source term of the fixed source calculation was potentially being altered by the change in the amount of fissile material present, the first step was to re-run the eigenvalue calculation to produce a new mesh source. The new mesh source was then used in a new MAVRIC calculation to obtain the new computed response values. In all cases the change seen in the computed response for a given 1 percent change in the ^{235}U number density was small and in the negative direction. In other words, for a one percent decrease in the ^{235}U number density the computed response for each of the thermal reactions will increase slightly.

The results for the density of the PPB9 are similar to those obtained for the ^{235}U number density. The simplified model was the starting point for all studies. The density of the PPB9 was increased and decreased and the simulations were re-run to determine if there was an affect on the computed response. None of the foils exhibited a statistically significant change in computed response when the density of the PPB9 was increased. This remained true for all of the increases studied which ranged from 5 percent to 100 percent. None of the foils were overly sensitive to decreasing the density of the PPB9. The cobalt foil experienced the largest percentage change for a given 1 percent decrease in the PPB9 density of 0.2664 percent. The sensitivity coefficient for Indium was the smallest at -0.0948. The sensitivity coefficients associated with changing the density of the PPB9 are all negative indicating that as the density of the PPB9 decreases the computed response increases slightly.

The final study done was to examine the effect of impurities in the activation foils on the computed response and to examine the effect of impurities in the aluminum frame surrounding the foils on the computed response. The benchmark material specifications for the activation

foils were altered by removing all impurities from the material specifications. The only exception was the iron foil, the ^{55}Mn was retained in the material specification due to it being important to the final estimate of response. The benchmark material specification for the aluminum frame was altered to use the SCALE standard composition for natural aluminum. Once the material specifications in the final simplified model had been altered, the simulations were re-run to obtain new estimates of response. In all cases the computed response was statistically identical to the original case with all of the impurities present. These results indicate that the computational models are not sensitive to small amounts of impurities being present in the material models for the activation foils or for the aluminum frame holding the foils.

5.4 Simplified 3-D Model Uncertainty

The final step in the sensitivity and uncertainty analysis of the computational model for this portion of pulse 1 is to use the computed sensitivity coefficients to compute the uncertainty in the computed estimates for each of the parameters studied. Recall that the sensitivity coefficients calculated and shown in Table 21 were normalized to enable comparisons amongst the parameters being studied. In order to calculated the parameter uncertainties, $S_{R,x}$, the sensitivity in response $\mathcal{R}$ due to parameter x needs to be multiplied by the ratio of the nominal response to the nominal value of the parameter as shown in equation (5-1).

(5- 1)

$$S_{R,x} = S * \frac{R}{x} = \frac{\Delta R/R}{\Delta x/x} * \frac{R}{x}$$

Once the individual sensitivity coefficients have been obtained, we can compute the uncertainty in the response due to uncertainty in the parameter using equation (2-96). If the uncertainty in a particular parameter is expressed as a percentage rather than as absolute uncertainty then σ_x can be computed as follows:

(5- 2)

$$\sigma_x = \sigma * x$$

where σ is the uncertainty expressed as a percentage and x is the nominal value of the parameter.

If we substitute (5-2) into (2-96) we will obtain an expression for computing the uncertainty in response $\mathcal{R}$ due to parameter x.

(5- 3)

$$\sigma_{\mathcal{R},x} = S_{\mathcal{R}} \cdot \sigma \cdot x$$

The individual uncertainties associated with each parameter can be combined into a total uncertainty estimate for each parameter by taking the square root of the sum of the squares of the individual estimates as shown in equation (5-4) where we have assumed that the evaluated uncertainties are uncorrelated.

(5- 4)

$$\Delta R_{total} = \sqrt{\sum_{i=1}^{N} \left(S_{R,x_i} \cdot \sigma_i \cdot x_i\right)^2}$$

Recall from the known uncertainties given in Appendix C that the uncertainty associated with the ^{235}U enrichment was 0.02% (or 0.0002). Reference 24 stated that the uncertainty on the thickness of the foils was 10% (or 0.1). (Piot, June 2011) The uncertainty associated with the density of the PPB9 is a little more difficult to determine. Examining Annex XIII from reference 24 we find that the density of the PPB9 ranges from a high of 1.2 g/cm^3 to a low of 0.96 g/cm^3. The difference between the high value and the nominal value is 17.48 percent of the nominal value while the difference between the lower value and the nominal value is 7.29 percent of the nominal value. These values represent the maximum and minimum uncertainty on the value of the PPB9 density. A value of 10% uncertainty was selected for this analysis since no value was indicated as preferred over another. These values of uncertainty were multiplied by the parameter in question to arrive at the uncertainty on each parameter σ_x. Table 22 shows the computed uncertainty on the response due to uncertainty in parameter x as both an absolute value, $\sigma_{R,x}$ and as a relative percentage of the computed response, $\%\sigma_{R,x}$ for each of the thermal foils.

The total number of fissions reported for pulse 1 was reported as having an associated uncertainty of 4 percent. (Hamon, 2004) The results obtained from MAVRIC used the reported value of total fissions to convert the results from a per fission basis to a total number of particles basis by multiplying the computed MAVRIC result by the total number of fissions. Propagation of error could have been used to propagate this uncertainty into all of the computed MAVRIC results. However, it was felt that doing this would obscure the Monte Carlo uncertainty associated with the results. Therefore, the uncertainty on the total number of fissions has been reported as one more aspect of the model unknowns contributing to the model uncertainty in Table 22 for the thermal foil reactions. The 4% uncertainty also applies to each of the threshold foil reactions and will be reported in the final results tabulation. The uncertainties reported with all of the computed results up to this point are the Monte Carlo uncertainties associated with the computation itself.

Table 22: Benchmark Uncertainty Values for Thermal Foil Reactions

Parameter	S	R	x	σ_x	$\sigma_{R,x}$	% $\sigma_{R,x}$
Gold Foil						
Foil Thickness	0.6816	7.7183E04	0.025 cm	2.5E-03	5.2608E03	6.816
^{235}U Number Density	-0.2099	7.7183E04	1.669503E-04 at/b-cm	3.3390E-08	-3.2401	4.1979E-03
PPB9 Density	-0.2152	7.7183E04	1.02 g/cm^3	0.102	-1.6610E03	2.152
Total Fissions					7.520E15	4.0
				Total		**8.1908**
Cobalt Foil						
Foil Thickness	0.7497	6.9614E01	0.2 cm	2.0E-02	5.2190	7.4971
^{235}U Number Density	-0.3282	6.9614E01	1.669503E-04 at/b-cm	3.3390E-08	-4.5694E-03	6.5639E-03
PPB9 Density	-0.2664	6.9614E01	1.02 g/cm^3	0.102	-1.8546	2.6641
Total Fissions					7.520E15	4.0
				Total		**8.9053**
Indium Foil						
Foil Thickness	0.4290	1.1708E07	0.1 cm	1E-02	5.0227E05	4.2900
^{235}U Number Density	-0.2207	1.1708E07	1.669503E-04 at/b-cm	3.3390E-08	-5.1678E02	4.4139E-03
PPB9 Density	-0.0948	1.1708E07	1.02 g/cm^3	0.102	-1.1091E05	0.9473
Total Fissions					7.520E15	4.0
				Total		**5.9415**
Iron Foil (Iron-56)						
Foil Thickness	Not Sensitive					
^{235}U Number Density	-0.3598	2.2501E03	1.669503E-04 at/b-cm	3.3390E-08	-1.6192E-01	7.1961E-03
PPB9 Density	-0.1307	2.2501E03	1.02 g/cm^3	0.102	-2.9409E01	1.3070
Total Fissions					7.520E15	4.0
				Total		**4.2081**

In examining the results in Table 22 it is obvious that the largest contributor of uncertainty to the final computed response is uncertainty in the thickness of the activation foil. Upon inspection this result makes physical sense because the amount of activation present can be directly related to the amount of foil present to be activated. The next largest contributor to the model uncertainty is the total number of fissions, which contributes a flat 4 percent uncertainty to all of the activation rates computed.

It is also worth noting that even though the density of the PPB9 had the same associated uncertainty as the thickness of the foils, its overall contribution to uncertainty in the final estimate was less than that contributed by the thickness of the foils, which is due to the fact that the final computed response was almost insensitive to changes in the PPB9 density. Uncertainty in the ^{235}U number density was practically a non-contributor to the final uncertainty estimate due to its contribution being two orders of magnitude less than that contributed by the foil thickness parameter or the PPB9 density parameter.

The total uncertainty in the computed activation due to unknowns in the model inputs can be seen to range from a low of 4.2 percent for the Iron foil to a high of 8.9 percent for the cobalt foil. By comparison, the Monte Carlo uncertainty associated with the computed results is on the order of 1 percent. Clearly the unknowns from the experiment are the major driver to the overall uncertainty – not the computational method – which is the desired result.

5.5 Final Summary of Results

Now that an estimated response has been computed for each activation foil and an estimate of the total uncertainty of this result has also been computed the final step is to combine this information and perform one last comparison with the measured dosimetry.

Table 23 contains the final summary comparison of results. The simplified calculated response for each foil is reported. The Monte Carlo (calculated) uncertainty and the benchmark uncertainty calculated in the previous section are reported and are used to compute the total uncertainty associated with each foil's calculated result. The measured results for each foil are also reported and a final C/E is computed for each foil. Since both the measured and the calculated values of response have an associated uncertainty, the final C/E also has an associated uncertainty and propagation of error was used to compute this value as shown below.

We can define a function, R as the ratio of the computed response to the experimental response as follows:

(5- 5)

$$R \pm \sigma_R = \frac{C \pm \sigma_c}{E \pm \sigma_E}$$

The uncertainty for R, σ_R can be computed using propagation of error as follows.

(5- 6)

$$\sigma_R = \sqrt{\left(\frac{\partial R}{\partial C}\sigma_c\right)^2 + \left(\frac{\partial R}{\partial E}\sigma_E\right)^2}$$

The partial derivatives of R with respect to the independent variables C and E are computed as shown in equations (5-7) and (5-8).

(5- 7)

$$\frac{\partial R}{\partial C} = \frac{\partial}{\partial C}\left(\frac{C}{E}\right) = \frac{1}{E}$$

(5- 8)

$$\frac{\partial R}{\partial E} = \frac{\partial}{\partial E}\left(\frac{C}{E}\right) = \frac{-C}{E^2}$$

Substituting equations (5-7) and (5-8) into (5-6) we obtain the following expression.

(5- 9)

$$\sigma_R = \sqrt{\left(\frac{1}{E}\sigma_c\right)^2 + \left(\frac{-C}{E^2}\sigma_E\right)^2}$$

Some slight simplifications in equation (5-9) yield the following equation.

(5- 10)

$$\sigma_R = \sqrt{\left(\frac{\sigma_c}{E}\right)^2 + \left(\frac{C\sigma_E}{E^2}\right)^2}$$

Equation (5-10) was used to compute the uncertainty associated with the C/E ratio for each of the foil responses. As noted earlier, the final results are summarized in Table 23. The final results are also shown graphically in Figure 36 with two sigma error bars applied. Because the Gold foil measured response data was deemed inaccurate, there is no final computation of a C/E for this reaction. Note that since the benchmark uncertainty for the threshold foils was a constant 4.0 percent due to the uncertainty on the number of fissions that the total uncertainty for these foils is less than for the thermal foils.

The final estimates of response from the simplified computational model are all in excellent agreement with the measured results provided by the French. The only real exception to this is the thermal indium reaction with a relative error of 28 percent. However, as has been stated earlier this result is still judged usable based on a review of existing shielding benchmarks in the handbook.

Table 23: Final Results Summary for Activation Foils

Foil	Simplified Calculated Response [Bq/g]	Calculated Uncertainty (± %σ)	Benchmark Uncertainty (± %σ)	Total Uncertainty (± %σ)	Measured Response [Bq/g]	Measured Uncertainty (± %σ)	C/E	C/E Uncertainty (± %σ)
Threshold Foils								
Ni	13.325	0.9094	4.0	4.1021	14.360	1.5320	0.9279	4.3788
Fe-54	0.2039	0.9294	4.0	4.1066	0.2062	1.9884	0.9888	4.5627
Fe-56[1]	122.57	1.1259	4.0	4.1554	N/A	N/A	N/A	N/A
Mg	66.134	1.0343	4.0	4.1316	61.100	1.8822	1.0824	4.5401
In	7402.1	1.1193	4.0	4.1537	8030	1.5567	0.9218	4.4357
Thermal Foils								
Au	7.7183×10^{4}	1.0518	8.1908	8.2581	1.812×10^{5}	1.5728	N/A	N/A
Co	69.614	1.0069	8.9053	8.9620	66.1	1.2859	1.0532	9.0538
In	1.1708×10^{7}	1.0196	5.9415	6.0284	9.11×10^{6}	1.9210	1.2852	6.3271
Fe-56[2]	2.2501×10^{3}	1.1397	4.2081	4.3597	N/A	N/A	N/A	N/A
Thermal + Threshold								
Fe-56 (1 + 2)	2372.67	1.0153	5.8059	5.8940	2310.00	1.3203	1.0271	6.0401

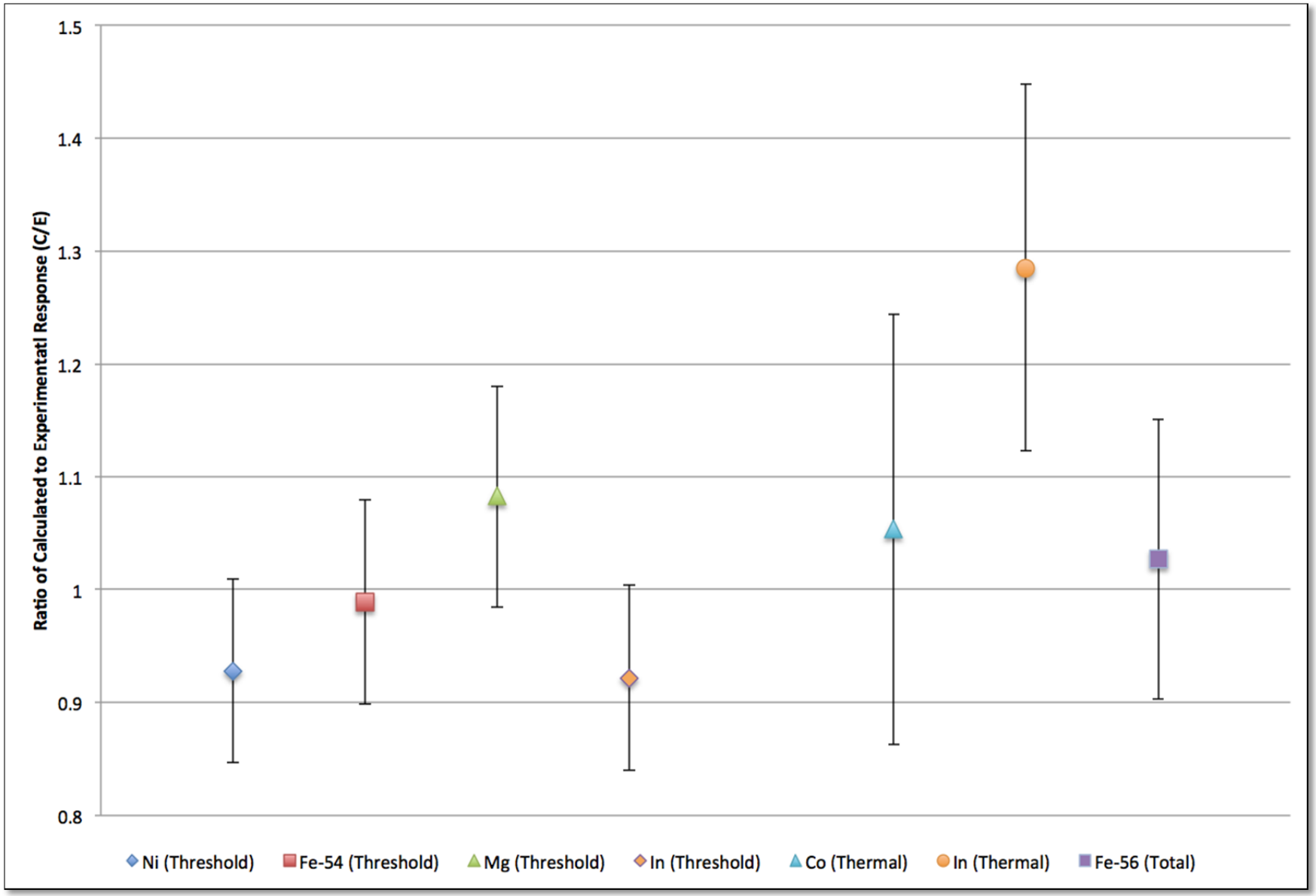


Figure 36: Final C/E Ratio for Activation Foils

Conclusions and Future Work

Both the high fidelity 3-D model and the simplified 3-D model generated computational results that compared very well with the measured results provided by the French. The only exception to this was the thermal gold foil response and this discrepancy was tied to bad measurement data rather than bad modeling. The computed results were generally within 10% agreement with the measurements and none of the computed results was more than 29% different from the measurements, which is acceptable according to current standards for shielding benchmarks.

For the threshold reactions the floor of the reactor cell was required to be part of the model in order to ensure that accurate estimates of response were obtained for the Indium and Nickel foils. The results for the Iron and Magnesium threshold reactions were statistically the same between the high fidelity model and the model with only SILENE and collimator box A. The final simplified model for the threshold foils included SILENE, a simplified model of the box portion of collimator box A, and a simplified model of the reactor cell (floor, walls, and ceiling). The threshold foil reactions proved to be essentially insensitive to any of the uncertainties given in reference 24. With the exception of the effect of scattering from the floor none of the other direct perturbations made to the high fidelity model resulted in statistically significant differences in the computed activations. Therefore, the 4% uncertainty on the total number of fissions was the only benchmark uncertainty carried forward for the threshold reactions. The final simplified model generated estimates of response that were in good agreement with the measured dosimetry for all of the threshold foil reactions. The Nickel foil's C/E was 0.93 and at 7 percent was the maximum relative error seen in the computed threshold foil results. The Iron-54 reaction had a C/E of 0.989 or about 1 percent relative error. All of the threshold foil C/E estimates are statistically equivalent to 1.0 when the two-sigma error bars are applied

For the thermal foils, the thickness of the foil proved to be the largest sensitivity, which was not an unexpected result in retrospect. Changing the amount of ^{235}U in the fuel did produce a measureable effect – but only after the amount of ^{235}U in the model was decreased by 25%. This result indicates that small variations in the ^{235}U content due to model uncertainties will not have an effect on the final answer. The same is true for the density of the PPB9. Increasing the density of the PPB9 had no effect on the computed answer for any of the thermal foils. The density of the PPB9 had to be reduced 50% before a significant change in the computed response was seen. Again, this indicates that small variations in the computational model due to having to make assumptions from the input technical data had no impact on the final computed answer. The uncertainty associated with the total number of fissions reported for pulse one was about 4 percent and was a large contributor to the final total uncertainty values computed for the thermal foils. The C/E values for the thermal foils ranged from a worst case agreement of 1.2852 (28.52 percent relative error) to a low of 1.0271 (2 percent relative error) indicating that the final simplified model of the experiment is producing results in good agreement with the experimentally measured values. Finally, the computed answers were insensitive to altering the impurity levels in the foils or in the aluminum surrounding them (the foil holder). In both cases when all of the impurities were removed leaving behind only the pure materials, the computed responses were statistically the same.

The results in this dissertation indicate that the MAVRIC computational sequence in the SCALE code package did in fact reproduce the experiment quite well. The computational uncertainties associated with the results are far lower than the uncertainties carried forward due to the uncertainties in the input technical parameters. SCALE now has the capability of solving large CAAS related shielding problems that previously were not solvable. In this case the variance reduction was automatic (as designed) and allowed the simulations to be run to conclusion in a reasonable amount of time.

The data produced in the pulse 1 experiment for Collimator Box A can be used as an effective CAAS/shielding benchmark.

Future work should start with completing the evaluation of pulse 1. There are activation foils located in Collimator Box B, the Scattering Box, and in the Free Field Location. The high fidelity geometry model can be taken and the simplification process and subsequent evaluation of sensitivity and uncertainty can be done for all of these foil locations. TLDs were also positioned at each of the above locations. The simplified model for each location should be taken and used to produce computed estimates of response for both the neutron activation foils and the TLD gamma dose for all the pulse 1 locations. One aspect of evaluation that should be added to the sensitivity study is the composition of the collimator box materials. Since the responses turned out to be only slightly sensitive to the composition of the PPB9 a study of the other box materials seems to be in order. This would involve studying the effects of the lead, copper and stainless steel layers around the PPB9. Once the evaluation of Pulse 1 is complete, the evaluation of pulse 2 and pulse 3 should be conducted in the same manner as the evaluation of pulse 1. Together, the three evaluations of neutron and gamma responses should then be taken and published as shielding benchmarks in the ICSBEP handbook.

Further experiments should also be designed and conducted to compliment the data produced by this experiment. The SILENE reactor produces a thermal spectrum due to its being fueled by liquid uranyl nitrate. A second series of measurements should be conducted using a reactor that produces a fast spectrum – such as CALIBAN (in France) or GODIVA (in the U.S.). Also, the intermediate energy spectrum has not been evaluated as yet in this process although experiments to study this portion of the spectrum would involve the design of a source or modification of a fast spectrum source since no reactors exist which produce this sort of spectrum. Finally, further testing of the CAAS detectors themselves could be conducted. This experiment was concerned simply with whether or not the CAAS detectors would alarm as designed when exposed to the radiation field in the pulse. Follow-on experiments could be conducted in which the CAAS detectors measurement of dose could be captured and then further MAVRIC/Monaco simulations run to try and match the measured doses.

Works Cited

1. Barbry, F. Y. (1993). A Review of the SILENE Criticality Excursions Experiments. *Topical Meeting on Physics & Methods in Criticality Safety* (pp. 34-40). Nashville, TN: American Nuclear Society.
2. Barbry, F., Fouillaud, P., & Verrey, B. (1999). Uses and Performances of the SILENE Reactor. *International Conference on Nuclear Criticality.* Versailles: ICNC' 99.
3. Bellamy, S. J., & Cooper, A. (2005). Radiation Tolerance Assessment of CIDAS MkX Criticality Incident Detection and Alarm System. *NCSD Topical Meeting on Integrating Criticality Safety into the Resurgence of Nuclear Power* (p. 13). LaGrange Park: American Nuclear Society.
4. Briggs, J. B. (2012). *International Handbook of Evaluated Crticality Safety Benchmark Experiments.* Idaho Falls, ID, USA: Idaho National Laboratory.
5. Chateauvieux, H., & Piot, J. M. (6/16/2011). *CAAS Test Dosimetry Report, Pulse 1.* Centre de Valduc, Direction des applications militaires. Valduc: CEA Valduc.
6. Chateauvieux, H., & Piot, J. M. (5/24/2012). *CAAS Test Dosimetry Report, Pulse 2.* Centre de Valduc, Direction des applications militaires. Valduc: CEA Valduc.
7. Chateauvieux, H., & Piot, J. M. (5/31/2012). *CAAS Test Dosimetry Report, Pulse 3.* Centre de Valduc, Direction des applications militaires. Valduc: CEA Valduc.
8. Chilton, A. B., Shultis, J. K., & Faw, R. E. (1984). *Principles of Radiation Shielding.* Englewood Cliffs, NJ, USA: Prentice Hall.
9. Dean, V. F. (September 2008). *ICSBEP Guide to the Expression of Uncertainties.* Idaho Falls, ID: Idaho National Laboratory.
10. Duderstadt, J. J., & Hamilton, L. J. (1976). *Nuclear Reactor Analysis.* New York: John Wiley & Sons.
11. Haghighat, A., & Wagner, J. C. (2003). Monte Carlo Variance Reduction with Deterministic Importance Functions. *Progress in Nuclear Energy , 42* (1), 25-53.
12. Hamon, K. (2004). *Calibration of SILENE Reactor.* Commissariat a l Energie Atomique - Centre d etudes de Valduc, Department de recherche en Neutronique et Criticite. Valduc: CEA Valduc.
13. Hunter, R. (August 2010). *Construction Details of CIDAS Detectors.* Babcock International. Babcock International.
14. Kalos, M. H., & Whitlock, P. A. (1986). *Monte Carlo Methods Volume I: Basics.* New York, USA: John Wiley and Sons.
15. Kim, S., & Heinrichs, D. (June 2009). *Rocky Flats CAAS System, Recalibrated, Retested, and Analyzed to Install in the Criticality Experiments Facility at the Nevada Test Site.* Lawrence Livermore National Laboratory. Livermore: Lawrence Livermore National Laboratory.
16. Lewis, E. E., & Miller, Jr., W. F. (1993). *Computational Methods of Neutron Transport.* La Grange Park, Illinois, USA: American Nuclear Society, Inc.
17. McMahan, K. L. (April 2010). *Technical Basis for the Oak Ridge National Laboratory External Dosimetry Program.* Oak RIdge National Laboratory, Nuclear and radiological Protection Division. Oak Ridge: Oak Ridge National Laboratory.

18. MIller, T. M., & Reynolds, K. H. (September 2011). 2010 Criticality Accident Alarm System Benchmark Experiments at the CEA Valduc SILENE Facility. *International Conference on Nuclear Criticality.* Edinburgh: ICNC 2011.
19. Miller, T. M., & Reynolds, K. H. (November 2011). SILENE Benchmark Critical Experiments for Criticality Accident Alarm Systems. *American Nuclear Society Transactions. 105*, pp. 609-610. LaGrange Park: American Nuclear Society.
20. Oak Ridge National Laboratory. (June 2011). *SCALE: A Comprehensive Modeling and Simulation Suite for Nuclear Safety Analysis and Design.* Oak Ridge, TN: Radiation Safety Information Computational Center.
21. Peplow, D. E. (2011). Monte Carlo Shielding Analysis Capabilities with MAVRIC. *Nuclear Technology , 174*, 289-313.
22. Peplow, D. E., & Petrie, L. M. (2010). Modeling Criticality Accident Alarm Systems with SCALE 6.1. *Transactions of the American Nuclear Society. 102*, p. 297. LaGrange Park: American Nuclear Society.
23. Peplow, D. E., Mosher, S. W., & Evans, T. M. (August 2012). *Consistent Adjoint Driven Importance Sampling using Space, Energy, and Angle.* Oak Ridge National Laboratory. Oak Ridge: Oak Ridge National Laboratory.
24. Piot, J. (June 2011). *2010 CAAS Test on the SILENE Reactor: Data for CAAS Experiment Modeling.* Centre de Valduc, Direction des applications militaires. Valduc: CEA Valduc.
25. Stacey, W. M. (2001). *Nuclear Reactor Physics.* New York, NY, USA: John Wiley and Sons.
26. Wagner, J. C., Peplow, D. E., & Mosher, S. W. (2013). FW-CADIS Method for Global and Regional Variance Reduction of Monte Carlo Radiation Transport Calculations. *Nuclear Science and Engineering* .
27. X-5 Monte Carlo Team. (2/1/2008). *MCNP - A General Monte Carlo N-Particle Trasnport Code, Version 5.* Los Alamos National Laboratory, X-5 Monte Carlo Team. Los Alamos: Los Alamos National Laboratory.

Appendices

Appendix A

The following tables contain the benchmark material specifications for each of the activation foils used in Collimator Box A. (Piot, June 2011)

Table 24: Benchmark Material Specification for Iron Foil

Element	ZAID	Number Density [atoms/b-cm]	Element	ZAID	Number Density [atoms/b-cm]
al-27	13027	4.313632E-05	si-28	14028	1.987331E-05
si-29	14029	1.009580E-06	si-30	14030	6.663010E-07
ca-40	20040	5.630423E-06	ca-42	20042	3.757836E-08
ca-43	20043	7.840926E-09	ca-44	20044	1.211568E-07
ca-46	20046	2.323237E-10	ca-48	20048	1.086113E-08
fe-54	26054	4.852518E-03	fe-56	26056	7.617416E-02
fe-57	26057	1.759193E-03	fe-58	26058	2.341163E-04
mn-55	25055	2.626989E-04	p-31	15031	1.352753E-05
s-32	16032	1.103340E-05	s-33	16033	8.711497E-08
s-34	16034	4.936515E-07	s-36	16036	1.161533E-09
ni-58	28058	2.159935E-06	ni-60	28060	8.320031E-07
ni-61	28061	3.616660E-08	ni-62	28062	1.153149E-07
ni-64	28064	2.936732E-08	cr-50	24050	2.723244E-07
cr-52	24052	5.251506E-06	cr-53	24053	5.954785E-07
cr-54	24054	1.482272E-07	cd-106	48106	5.176890E-09
cd-108	48108	3.685945E-09	cd-110	48110	5.172748E-08
cd-111	48111	5.301135E-08	cd-112	48112	9.993467E-08
cd-113	48113	5.060927E-08	cd-114	48114	1.189856E-07
cd-116	48116	3.101992E-08	mg-24	12024	1.513023E-06
mg-25	12025	1.915461E-07	mg-26	12026	2.108923E-07
ti-46	22046	8.023980E-08	ti-47	22047	7.236172E-08
ti-48	22048	7.170034E-07	ti-49	22049	5.261785E-08
ti-50	22050	5.038087E-08	v	23000	9.138988E-07
co-59	27059	1.579937E-06	cu-63	29063	3.039658E-06
cu-65	29065	1.356088E-06	zn	30000	7.120738E-07
as-75	33075	1.242776E-06	zr-90	40090	2.625717E-07
zr-91	40091	5.726052E-08	zr-92	40092	8.752387E-08
zr-94	40094	8.869766E-08	zr-96	40096	1.428961E-08
mo-92	42092	7.167399E-08	mo-94	42094	4.479017E-08
mo-95	42095	7.715750E-08	mo-96	42096	8.094258E-08
mo-97	42097	4.639156E-08	mo-98	42098	1.173862E-07
mo-100	42100	4.692535E-08	ag-107	47107	2.237347E-07
ag-109	47109	2.078606E-07	sn-112	50112	1.902059E-08
sn-114	50114	1.294184E-08	sn-115	50115	6.667010E-09
sn-116	50116	2.851127E-07	sn-117	50117	1.505960E-07
sn-118	50118	4.749263E-07	sn-119	50119	1.684400E-07
sn-120	50120	6.388564E-07	sn-122	50122	9.078898E-08
sn-124	50124	1.135352E-07	ba-130	56130	3.593521E-10
ba-132	56132	3.424015E-10	ba-134	56134	8.193905E-09
ba-135	56135	2.234763E-08	ba-136	56136	2.662595E-08
ba-137	56137	3.807776E-08	ba-138	56138	2.430644E-07
pb-204	82204	3.145377E-09	pb-206	82206	5.414542E-08
pb-207	82207	4.965202E-08	pb-208	82208	1.177270E-07
be-9	4009	5.165828E-06	ga-69	31069	4.013523E-07
ga-71	31071	2.663663E-07	k-39	19039	1.110449E-06

Table 24 (Continued)

Element	ZAID	Number Density [atoms/b-cm]	Element	ZAID	Number Density [atoms/b-cm]
k-40	19040	1.393150E-10	k-41	19041	8.013826E-08
li-6	3006	5.091551E-07	li-7	3007	6.199080E-06
na-23	11023	2.025047E-06	nb-93	41093	5.010999E-07
se-74	34074	5.247544E-09	se-76	34076	5.524662E-08
se-77	34077	4.498738E-08	se-78	34078	1.401507E-07
se-80	34080	2.925064E-07	se-82	34082	5.147310E-08
pd-102	46102	4.462373E-09	pd-104	46104	4.873610E-08
pd-105	46105	9.769097E-08	pd-106	46106	1.195653E-07
pd-108	46108	1.157592E-07	pd-110	46110	5.127354E-08

Table 25: Benchmark Material Specification for Magnesium Foil

Element	ZAID	Number Density [atoms/b-cm]	Element	ZAID	Number Density [atoms/b-cm]
b-10	5010	1.924805E-07	al-27	13027	1.937778E-06
si-28	14028	2.060199E-06	si-29	14029	1.046597E-07
si-30	14030	6.907315E-08	ca-40	20040	2.529310E-07
ca-42	20042	1.688103E-09	ca-43	20043	3.522316E-10
ca-44	20044	5.442630E-09	ca-46	20046	1.043649E-11
ca-48	20048	4.879060E-10	fe-54	26054	3.283380E-08
fe-56	26056	5.154204E-07	fe-57	26057	1.190330E-08
fe-58	26058	1.584111E-09	mn-55	25055	6.090846E-06
p-31	15031	3.376035E-07	ni-58	28058	1.212863E-07
ni-60	28060	4.671926E-08	ni-61	28061	2.030854E-09
ni-62	28062	6.475251E-09	ni-64	28064	1.649056E-09
cr-50	24050	8.738151E-09	cr-52	24052	1.685065E-07
cr-53	24053	1.910729E-08	cr-54	24054	4.756209E-09
cd-106	48106	1.162786E-09	cd-108	48108	8.279037E-10
cd-110	48110	1.161856E-08	cd-111	48111	1.190693E-08
cd-112	48112	2.244643E-08	cd-113	48113	1.136740E-08
cd-114	48114	2.672548E-08	cd-116	48116	6.967414E-09
b-11	5011	7.747581E-07	mg-24	12024	3.395866E-02
mg-25	25055	4.299108E-03	mg-26	12026	4.733319E-03
ti-46	22046	1.802274E-08	ti-47	22047	1.625324E-08
ti-48	22048	1.610468E-07	ti-49	22049	1.181855E-08
ti-50	22050	1.131610E-08	v	23000	2.052717E-07
co-59	27059	1.774356E-07	cu-63	29063	2.275802E-07
cu-65	29065	1.015307E-07	zn	30000	3.198791E-07
as-75	33075	1.395705E-07	zr-90	40090	5.897648E-08
zr-91	40091	1.286134E-08	zr-92	40092	1.965882E-08
zr-94	40094	1.992247E-08	zr-96	40096	3.209603E-09
mo-92	42092	1.609876E-08	mo-94	42094	1.006036E-08
mo-95	42095	1.733042E-08	mo-96	42096	1.818059E-08
mo-97	42097	1.042005E-08	mo-98	42098	2.636622E-08
mo-100	42100	1.053995E-08	ag-107	47107	5.025326E-08
ag-109	47109	4.668777E-08	sn-112	50112	8.544465E-10
sn-114	50114	5.813759E-10	sn-115	50115	2.994967E-10
sn-116	50116	1.280789E-08	sn-117	50117	6.765102E-09
sn-118	50118	2.133473E-08	sn-119	50119	7.566697E-09
sn-120	50120	2.869883E-08	sn-122	50122	4.078441E-09
sn-124	50124	5.100253E-09	sb-121	51121	4.913251E-08
sb-123	51123	3.674847E-08	ba-130	56130	8.071441E-11
ba-132	56132	7.690713E-11	ba-134	56134	1.840441E-09
ba-135	56135	5.019523E-09	ba-136	56136	5.980481E-09
ba-137	56137	8.552682E-09	ba-138	56138	5.459493E-08
bi-209	83209	5.003746E-08	pb-204	82204	1.412972E-09
pb-206	82206	2.432331E-08	pb-207	82207	2.230478E-08
pb-208	82208	5.288553E-08	be-9	4009	1.160302E-06
k-39	19039	2.494190E-07	k-40	19040	3.129167E-11

Table 25 (Continued)

Element	ZAID	Number Density [atoms/b-cm]	Element	ZAID	Number Density [atoms/b-cm]
k-41	19041	1.799993E-08	na-23	11023	4.548479E-07
nb-93	41093	1.125525E-07	w-182	74182	1.494261E-08
w-183	74183	8.001951E-09	w-184	74184	1.762221E-08
w-186	74186	1.630769E-08	y-89	39089	1.176171E-07

Table 26: Benchmark Material Specification for Cobalt Foil

Element	ZAID	Number Density [atoms/b-cm]	Element	ZAID	Number Density [atoms/b-cm]
b-10	5010	1.025554E-06	al-27	13027	1.032466E-05
si-28	14028	9.147440E-06	si-29	14029	4.646971E-07
si-30	14030	3.066901E-07	ca-40	20040	1.078112E-05
ca-42	20042	7.195494E-08	ca-43	20043	1.501378E-08
ca-44	20044	2.319907E-07	ca-46	20046	4.448528E-10
ca-48	20048	2.079687E-08	fe-54	26054	1.749415E-07
fe-56	25056	2.746207E-06	fe-57	26057	6.342191E-08
fe-58	26058	8.440292E-09	mn-55	25055	1.014143E-06
p-31	15031	1.798783E-06	ni-58	28058	6.462245E-07
ni-60	28060	2.489246E-07	ni-61	28061	1.082058E-08
ni-62	28062	3.450074E-08	ni-64	28064	8.786321E-09
cr-50	24050	4.655767E-08	cr-52	24052	8.978184E-07
cr-53	24053	1.018054E-07	cr-54	24054	2.534152E-08
cd-106	48106	6.195433E-09	cd-108	48108	4.411148E-09
cd-110	48110	6.190476E-08	cd-111	48111	6.344123E-08
cd-112	48112	1.195966E-07	cd-113	48113	6.056655E-08
cd-114	48114	1.423958E-07	cd-116	48116	3.712303E-08
b-11	5011	4.127983E-06	mg-24	12024	1.810707E-06
mg-25	12025	2.292324E-07	mg-26	12026	2.523849E-07
ti-46	22046	9.602682E-08	ti-47	22047	8.659875E-08
ti-48	22048	8.580725E-07	ti-49	22049	6.297032E-08
ti-50	22050	6.029320E-08	v	23000	1.093707E-06
co-59	27059	9.449491E-02	cu-63	29063	6.062843E-07
cu-65	29065	2.704826E-07	zn	30000	8.521729E-07
as-75	33075	7.436448E-07	zr-90	40090	3.142321E-07
zr-91	40091	6.852641E-08	zr-92	40092	1.047440E-07
zr-94	40094	1.061487E-07	zr-96	40096	1.710107E-08
mo-92	42092	8.577570E-08	mo-94	42094	5.360255E-08
mo-95	42095	9.233810E-08	mo-96	42096	9.686789E-08
mo-97	42097	5.551901E-08	mo-98	42098	1.404817E-07
mo-100	42100	5.615782E-08	ag-107	47107	2.677540E-07
ag-109	47109	2.487567E-07	sn-112	50112	4.552570E-09
sn-114	50114	3.097625E-09	sn-115	50115	1.595746E-09
sn-116	50116	6.824162E-08	sn-117	50117	3.604509E-08
sn-118	50118	1.136734E-07	sn-119	50119	4.031606E-08
sn-120	50120	1.529100E-07	sn-122	50122	2.173031E-08
sn-124	50124	2.717462E-08	sb-121	51121	2.617826E-07
sb-123	51123	1.957993E-07	ba-130	56130	4.300539E-10
ba-132	56132	4.097683E-10	ba-134	56134	9.806040E-09
ba-135	56135	2.674448E-08	ba-136	56136	3.186456E-08
ba-137	56137	4.556948E-08	ba-138	56138	2.908868E-07
bi-209	83209	2.666042E-07	pb-204	82204	3.764224E-09
pb-206	82206	6.479842E-08	pb-207	82207	5.942096E-08
pb-208	82208	1.408895E-07	be-9	4009	6.182195E-06

Table 26 (Continued)

Element	ZAID	Number Density [atoms/b-cm]	Element	ZAID	Number Density [atoms/b-cm]
k-39	19039	1.328927E-06	k-40	19040	1.667249E-10
k-41	19041	9.590531E-08	na-23	11023	2.423472E-06
nb-93	41093	5.996903E-07	sr-84	38084	3.561017E-09
sr-86	38086	6.269933E-08	sr-87	38087	4.451271E-08
sr-88	38088	5.251229E-07	ta-181	73181	3.079065E-07

Table 27: Benchmark Material Specification for Nickel Foil

Element	ZAID	Number Density [atoms/b-cm]	Element	ZAID	Number Density [atoms/b-cm]
b-10	5010	1.024667E-06	al-27	13027	2.682091E-05
si-28	14028	6.397672E-05	si-29	14029	3.250067E-06
si-30	14030	2.144975E-06	ca-40	20040	1.077180E-05
ca-42	20042	7.189271E-08	ca-43	20043	1.500080E-08
ca-44	20044	2.317901E-07	ca-46	20046	4.444681E-10
ca-48	20048	2.077888E-08	fe-54	26054	3.262751E-06
fe-56	56056	5.121821E-05	fe-57	26057	1.182852E-06
fe-58	56058	1.574159E-07	mn-55	25055	1.013266E-04
p-31	15031	1.797227E-06	ni-58	28058	6.436447E-02
ni-60	28060	2.479308E-02	ni-61	28061	1.077738E-03
ni-62	28062	3.436300E-03	ni-64	28064	8.751245E-04
cr-50	24050	1.395522E-07	cr-52	24052	2.691126E-06
cr-53	24053	3.051521E-07	cr-54	24054	7.595881E-08
cd-106	48106	6.190075E-09	cd-108	48108	4.407333E-09
cd-110	48110	6.185122E-08	cd-111	48111	6.338637E-08
cd-112	48112	1.194932E-07	cd-113	48113	6.051418E-08
cd-114	48114	1.422727E-07	cd-116	48116	3.709093E-08
b-11	5011	4.124413E-06	mg-24	12024	2.351883E-05
mg-25	12025	2.977444E-06	mg-26	12026	3.278166E-06
ti-46	22046	2.782370E-06	ti-47	22047	2.509192E-06
ti-48	22048	2.486258E-05	ti-49	22049	1.824560E-06
ti-50	22050	1.746991E-06	v	23000	1.092761E-06
co-59	27059	3.211558E-05	cu-63	29063	1.817280E-06
cu-65	29065	8.107459E-07	zn	30000	8.514359E-07
as-75	33075	7.430017E-07	zr-90	40090	3.139604E-07
zr-91	40091	6.846715E-08	zr-92	40092	1.046535E-07
zr-94	40094	1.060570E-07	zr-96	40096	1.708628E-08
mo-92	42092	8.570152E-08	mo-94	42094	5.355619E-08
mo-95	42095	9.225824E-08	mo-96	42096	9.678411E-08
mo-97	42097	5.547099E-08	mo-98	42098	1.403602E-07
mo-100	42100	5.610925E-08	ag-107	47107	2.675225E-07
ag-109	47109	2.485416E-07	sn-112	50112	4.548633E-09
sn-114	50114	3.094946E-09	sn-115	50115	1.594366E-09
sn-116	50116	6.818260E-08	sn-117	50117	3.601392E-08
sn-118	50118	1.135751E-07	sn-119	50119	4.028119E-08
sn-120	50120	1.527778E-07	sn-122	50122	2.171152E-08
sn-124	50124	2.715112E-08	ba-130	56130	4.296820E-10
ba-132	56132	4.094140E-10	ba-134	56134	9.797561E-09
ba-135	56135	2.672135E-08	ba-136	56136	3.183700E-08
ba-137	56137	4.553008E-08	ba-138	56138	2.906353E-07
bi-209	83209	2.663737E-07	pb-204	82204	3.760968E-09
pb-206	82206	6.474239E-08	pb-207	82207	5.936957E-08
pb-208	82208	1.407677E-07	be-9	4009	6.176849E-06
k-39	19039	1.327778E-06	k-40	19040	1.665807E-10
k-41	19041	9.582237E-08	na-23	11023	2.421376E-06

Table 27 (Continued)

Element	ZAID	Number Density [atoms/b-cm]	Element	ZAID	Number Density [atoms/b-cm]
nb-93	41093	5.991718E-07	w-182	74182	7.954675E-08
w-183	74183	4.259827E-08	w-184	74184	9.381160E-08
w-186	74186	8.681373E-08	sr-84	38084	3.557937E-09
sr-86	38086	6.264511E-08	sr-87	38087	4.447421E-08
sr-88	38088	5.246687E-07			

Table 28: Benchmark Material Specification for Gold Foil

Element	ZAID	Number Density [atoms/b-cm]
cu-63	29063	1.161709E-06
cu-65	29065	5.182749E-07
na-23	12023	1.547882E-06
au-197	79197	6.022151E-02
rh-103	45103	4.610760E-07

Table 29: Benchmark Material Specification for Indium Foil

Element	ZAID	Number Density [atoms/b-cm]	Element	ZAID	Number Density [atoms/b-cm]
b-10	5010	8.214340E-07	al-27	13027	8.269705E-06
si-28	14028	7.326791E-06	si-29	14029	3.722067E-07
si-30	14030	2.456485E-07	ca-40	20040	1.079414E-06
ca-42	20042	7.204185E-09	ca-43	20043	1.503192E-09
ca-44	20044	2.322709E-08	ca-46	20046	4.453901E-11
ca-48	20048	2.082199E-09	fe-54	26054	4.670742E-08
fe-56	26056	7.332066E-07	fe-57	26057	1.693294E-08
fe-58	26058	2.253463E-09	mn-55	25055	8.122946E-07
p-31	15031	1.440764E-06	ni-58	28058	5.176040E-07
ni-60	28060	1.993802E-07	ni-61	28061	8.666918E-09
ni-62	28062	2.763393E-08	ni-64	28064	7.037547E-09
cr-50	24050	3.729112E-08	cr-52	24052	7.191222E-07
cr-53	24053	8.154269E-08	cr-54	24054	2.029770E-08
cd-106	48106	4.962333E-09	cd-108	48108	3.533181E-09
cd-110	48110	4.958362E-08	cd-111	48111	5.081428E-08
cd-112	48112	9.579286E-08	cd-113	48113	4.851177E-08
cd-114	48114	1.140542E-07	cd-116	48116	2.973429E-08
b-11	5011	3.306375E-06	mg-24	12024	1.450315E-06
mg-25	12025	1.836074E-07	mg-26	12026	2.021518E-07
ti-46	22046	7.691424E-08	ti-47	22047	6.936267E-08
ti-48	22048	6.872871E-07	ti-49	22049	5.043710E-08
ti-50	22050	4.829282E-08	v	23000	8.760221E-07
co-59	27059	7.572282E-07	cu-63	29063	4.856133E-07
cu-65	29065	2.166474E-07	zn	30000	6.825617E-07
as-75	33075	5.956344E-07	mo-92	42092	6.870344E-08
mo-94	42094	4.293383E-08	mo-95	42095	7.395970E-08
mo-96	42096	7.758791E-08	mo-97	42097	4.446885E-08
mo-98	42098	1.125211E-07	mo-100	42100	4.498052E-08
ag-107	47107	2.144619E-07	ag-109	47109	1.992457E-07
sn-112	50112	7.292910E-09	sn-114	50114	4.962186E-09
sn-115	50115	2.556278E-09	sn-116	50116	1.093185E-07
sn-117	50117	5.774180E-08	sn-118	50118	1.820972E-07
sn-119	50119	6.458360E-08	sn-120	50120	2.449516E-07
sn-122	50122	3.481049E-08	sn-124	50124	4.353191E-08
sb-121	51121	2.096790E-07	sb-123	51123	1.568286E-07
ba-130	56130	3.444586E-10	ba-132	56132	3.282106E-10
ba-134	56134	7.854307E-09	ba-135	56135	2.142143E-08
ba-136	56136	2.552244E-08	ba-137	56137	3.649961E-08
ba-138	56138	2.329905E-07	pb-204	82204	3.015016E-09
pb-206	82206	5.190135E-08	pb-207	82207	4.759418E-08
pb-208	82208	1.128477E-07	be-9	4009	4.951730E-06
ga-69	31069	3.847182E-07	ga-71	31071	2.553267E-07
k-39	19039	1.064426E-06	k-40	19040	1.335410E-10
k-41	19041	7.681691E-08	li-6	3006	4.880530E-07

Table 29 (Continued)

Element	ZAID	Number Density [atoms/b-cm]	Element	ZAID	Number Density [atoms/b-cm]
li-7	3007	5.942159E-06	na-23	11023	1.941119E-06
nb-93	41093	4.803317E-07	in-113	49113	1.666743E-03
in-115	49115	3.718508E-02			

Appendix B

Table 30: Gold Foil Thermal Calculated Response Results

Case Name	Brief Case Description	Calculated Response (R) [Bq/g]	Calculated σ
Base	High Fidelity Model	7.64910E+04	804.50
DP1	SILENE and Collimator Box A only (no floor)	5.75100E+04	528.00
DP2	Same as dp1 except 40 cm thick floor now included as inscribed by boundary around SILENE and Collimator Box A	6.00350E+04	524.00
DP3	Same as dp1 except 40 cm thick floor now extends full y-dimension for reactor cell	6.14600E+04	536.50
DP4	Same as dp1 except 40 cm thick floor now extends 1/2 of x-dimension for reactor cell	6.37850E+04	546.00
DP5	Same as dp1 except 40 cm thick floor now extends full x and y dimensions of reactor cell	6.81970E+04	685.50
DP6	Same as dp1 except rear wall (+y dimension) now added	6.01140E+04	915.00
DP7	Same as dp1 except ceiling (+z dimension) now added	5.81010E+04	541.00
DP8	Same as dp1 except scattering box added	5.76380E+04	504.00
DP9	Same as dp1 except collimator box B added	5.85450E+04	540.00
DP10	Same as dp1 except Diagnostic Stand A added	5.84120E+04	570.50
DP11	Same as dp1 except Diagnostic Stand B added	5.83990E+04	550.50
DP12	Same as dp5 except rear wall (+y dimension) now added	7.03900E+04	714.50
DP13	Same as dp5 except ceiling (+z dimension) now added	Case failed to converge	
DP14	Same as dp5 except scattering box added	6.76250E+04	614.00
DP15	Same as dp5 except collimator box B added	6.81540E+04	661.50
DP16	Same as dp5 except Diagnostic Stand A added	6.73040E+04	677.50
DP17	Same as dp5 except Diagnostic Stand B added	6.77470E+04	625.00
DP18	same as dp1 except the room has been included in the global model (no door included as part of wall behind collimator box	7.57940E+04	850.50
DP19	same as dp18 except no frame and no equipment included in collimator box (i.e. foils only)	7.91040E+04	910.50
DP20	same as dp19 except now the roof (+z dimension) has been simplified to remove concrete rail system details from global unit	7.71170E+04	859.50
Final.1	Final revised input deck based upon dp20. This run uses revised input deck but old importance map and old source mesh	7.68820E+04	810.50
Final.2	Final revised input deck based upon dp20. This run uses revised input deck, new importance map based on re-running DENOVO with final input deck and old source mesh.	7.67630E+04	809.00
Final.3	Final revised input deck based upon dp20. This run uses all new files generated using the simplified input deck (source, DENOVO and MONACO).	7.71830E+04	867.00
foilthick.up	Final revised input deck based upon dp20. Increases the thickness of all the foils 2%.	7.76210E+04	872.00
foilthick.down	Final revised input deck based upon dp20. Decreases the thickness of all the foils 2%.	7.68180E+04	862.00
foilthick.up.max	Final revised input deck based upon dp20. All foils increased thickness to max of 0.33 cm (physical problem limit) except GOLD which was increased by factor of 3 to 0.075cm.	5.80610E+04	621.50
foilthick.down.max	Final revised input deck based upon dp20. Thickness of all foils was decreased by half.	9.01250E+04	1166.5

Table 30 (Continued)

Case Name	Brief Case Description	Calculated Response (R) [Bq/g]	Calculated σ
fueliso.up	Final revised input deck based upon dp20. U-235 number density in the fuel was increased 2%.	7.83170E+04	894.50
fueliso.down	Final revised input deck based upon dp20. U-235 number density in the fuel was decreased 2%.	7.82500E+04	860.50
fueliso.up.10%	Final revised input deck based upon dp20. U-235 number density in the fuel was increased 10%.	7.72020E+04	841.50
fueliso.down.10%	Final revised input deck based upon dp20. U-235 number density in the fuel was decreased 10%.	7.94030E+04	896.50
fueliso.up.20%	Final revised input deck based upon dp20. U-235 number density in the fuel was increased 20%.	7.25780E+04	762.50
fueliso.down.20%	Final revised input deck based upon dp20. U-235 number density in the fuel was decreased 20%.	8.33720E+04	947.50
fueliso.up.25%	Final revised input deck based upon dp20. U-235 number density in the fuel was increased 25%.	7.38860E+04	788.00
fueliso.down.25%	Final revised input deck based upon dp20. U-235 number density in the fuel was decreased 25%.	8.19900E+04	796.50
poly.density.up.5%	Final revised input deck based upon dp20. Density of PPB9 was increased 5% (all number densities changed).	7.69810E+04	870.50
poly.density.down.5%	Final revised input deck based upon dp20. Density of PPB9 was decreased 5% (all number densities changed).	7.79380E+04	852.50
poly.density.up.10%	Final revised input deck based upon dp20. Density of PPB9 was increased 10% (all number densities changed).	7.61220E+04	828.00
poly.density.down.10%	Final revised input deck based upon dp20. Density of PPB9 was decreased 10% (all number densities changed).	7.75770E+04	849.50
poly.density.up.15%	Final revised input deck based upon dp20. Density of PPB9 was increased 15% (all number densities changed).	7.64350E+04	849.50
poly.density.down.15%	Final revised input deck based upon dp20. Density of PPB9 was decreased 15% (all number densities changed).	7.72220E+04	863.50
poly.density.up.25%	Final revised input deck based upon dp20. Density of PPB9 was increased 25% (all number densities changed).	7.57270E+04	849.00
poly.density.down.25%	Final revised input deck based upon dp20. Density of PPB9 was decreased 25% (all number densities changed).	7.91400E+04	932.00
poly.density.up.50%	Final revised input deck based upon dp20. Density of PPB9 was increased 50% (all number densities changed).	7.65880E+04	865.50
poly.density.down.50%	Final revised input deck based upon dp20. Density of PPB9 was decreased 50% (all number densities changed).	8.54880E+04	871.50
poly.density.up.75%	Final revised input deck based upon dp20. Density of PPB9 was increased 75% (all number densities changed).	7.63410E+04	828.00
poly.density.down.75%	Final revised input deck based upon dp20. Density of PPB9 was decreased 75% (all number densities changed).	8.31030E+04	885.50
poly.density.up.100%	Final revised input deck based upon dp20. Density of PPB9 was increased 100% (all number densities changed).	7.64240E+04	917.50
foil.pure.gold	Final revised input deck based upon dp20. Gold foil now pure gold - no contaminants.	7.71230E+04	861.50
pure.aluminum.gold	Final revised input deck based upon dp20. Frame holding foils now pure aluminum (no contaminants). Gold Tally.	7.76700E+04	867.50

Table 31: Iron-56 Thermal Calculated Response Results

Case Name	Brief Case Description	Calculated Response (R) [Bq/g]	Calculated σ
Base	High Fidelity Model	2.20230E+03	25.10
DP1	SILENE and Collimator Box A only (no floor)	1.60510E+03	13.95
DP2	Same as dp1 except 40 cm thick floor now included as inscribed by boundary around SILENE and Collimator Box A	1.61760E+03	11.50
DP3	Same as dp1 except 40 cm thick floor now extends full y-dimension for reactor cell	1.68740E+03	13.00
DP4	Same as dp1 except 40 cm thick floor now extends 1/2 of x-dimension for reactor cell	1.75110E+03	13.10
DP5	Same as dp1 except 40 cm thick floor now extends full x and y dimensions of reactor cell	1.86360E+03	14.70
DP6	Same as dp1 except rear wall (+y dimension) now added	1.62450E+03	15.20
DP7	Same as dp1 except ceiling (+z dimension) now added	1.58880E+03	13.25
DP8	Same as dp1 except scattering box added	1.58150E+03	18.30
DP9	Same as dp1 except collimator box B added	1.60040E+03	12.50
DP10	Same as dp1 except Diagnostic Stand A added	1.60110E+03	15.80
DP11	Same as dp1 except Diagnostic Stand B added	1.59680E+03	13.60
DP12	Same as dp5 except rear wall (+y dimension) now added	1.95640E+03	22.70
DP13	Same as dp5 except ceiling (+z dimension) now added	Case failed to converge	
DP14	Same as dp5 except scattering box added	1.89750E+03	15.20
DP15	Same as dp5 except collimator box B added	1.89420E+03	16.15
DP16	Same as dp5 except Diagnostic Stand A added	1.87100E+03	15.65
DP17	Same as dp5 except Diagnostic Stand B added	1.86370E+03	15.60
DP18	same as dp1 except the room has been included in the global model (no door included as part of wall behind collimator box)	2.18230E+03	21.60
DP19	same as dp18 except no frame and no equipment included in collimator box (i.e. foils only)	2.25420E+03	24.25
DP20	same as dp19 except now the roof (+z dimension) has been simplified to remove concrete rail system details from global unit	2.22920E+03	23.05
Final.1	Final revised input deck based upon dp20. This run uses revised input deck but old importance map and old source mesh	2.20890E+03	24.20
Final.2	Final revised input deck based upon dp20. This run uses revised input deck, new importance map based on re-running DENOVO with final input deck and old source mesh.	2.19880E+03	23.50
Final.3	Final revised input deck based upon dp20. This run uses all new files generated using the simplified input deck (source, DENOVO and MONACO).	2.25010E+03	24.05
foilthick.up	Final revised input deck based upon dp20. Increases the thickness of all the foils 2%.	2.25340E+03	24.25
foilthick.down	Final revised input deck based upon dp20. Decreases the thickness of all the foils 2%.	2.25550E+03	24.15
foilthick.up.max	Final revised input deck based upon dp20. All foils increased thickness to max of 0.33 cm (physical problem limit) except GOLD which was increased by factor of 3 to 0.075cm.	2.24300E+03	25.25

Table 31 (Continued)

Case Name	Brief Case Description	Calculated Response (R) [Bq/g]	Calculated σ
foilthick.down.max	Final revised input deck based upon dp20. Thickness of all foils was decreased by half.	2.26770E+03	24.20
fueliso.up	Final revised input deck based upon dp20. U-235 number density in the fuel was increased 2%.	2.21330E+03	24.45
fueliso.down	Final revised input deck based upon dp20. U-235 number density in the fuel was decreased 2%.	2.25530E+03	26.50
fueliso.up.10%	Final revised input deck based upon dp20. U-235 number density in the fuel was increased 10%.	2.17650E+03	26.15
fueliso.down.10%	Final revised input deck based upon dp20. U-235 number density in the fuel was decreased 10%.	2.28390E+03	22.60
fueliso.up.20%	Final revised input deck based upon dp20. U-235 number density in the fuel was increased 20%.	2.07330E+03	22.30
fueliso.down.20%	Final revised input deck based upon dp20. U-235 number density in the fuel was decreased 20%.	2.36770E+03	22.40
fueliso.up.25%	Final revised input deck based upon dp20. U-235 number density in the fuel was increased 25%.	2.04710E+03	20.15
fueliso.down.25%	Final revised input deck based upon dp20. U-235 number density in the fuel was decreased 25%.	2.38630E+03	21.60
poly.density.up.5%	Final revised input deck based upon dp20. Density of PPB9 was increased 5% (all number densities changed).	2.23130E+03	23.75
poly.density.down.5%	Final revised input deck based upon dp20. Density of PPB9 was decreased 5% (all number densities changed).	2.24330E+03	23.40
poly.density.up.10%	Final revised input deck based upon dp20. Density of PPB9 was increased 10% (all number densities changed).	2.20420E+03	21.80
poly.density.down.10%	Final revised input deck based upon dp20. Density of PPB9 was decreased 10% (all number densities changed).	2.20060E+03	21.15
poly.density.up.15%	Final revised input deck based upon dp20. Density of PPB9 was increased 15% (all number densities changed).	2.23950E+03	24.05
poly.density.down.15%	Final revised input deck based upon dp20. Density of PPB9 was decreased 15% (all number densities changed).	2.25500E+03	23.75
poly.density.up.25%	Final revised input deck based upon dp20. Density of PPB9 was increased 25% (all number densities changed).	2.21260E+03	23.65
poly.density.down.25%	Final revised input deck based upon dp20. Density of PPB9 was decreased 25% (all number densities changed).	2.24070E+03	22.40
poly.density.up.50%	Final revised input deck based upon dp20. Density of PPB9 was increased 50% (all number densities changed).	2.20290E+03	23.80
poly.density.down.50%	Final revised input deck based upon dp20. Density of PPB9 was decreased 50% (all number densities changed).	2.39710E+03	22.05
poly.density.up.75%	Final revised input deck based upon dp20. Density of PPB9 was increased 75% (all number densities changed).	2.16010E+03	20.70
poly.density.down.75%	Final revised input deck based upon dp20. Density of PPB9 was decreased 75% (all number densities changed).	2.36090E+03	23.45
poly.density.up.100%	Final revised input deck based upon dp20. Density of PPB9 was increased 100% (all number densities changed).	2.19000E+03	21.80
foil.pure.iron	Final revised input deck based upon dp20. Iron foil now pure iron - no contaminants except 0.3 percent Mn	2.23760E+03	22.90
pure.aluminum.iron56	Final revised input deck based upon dp20. Frame holding foils now pure aluminum (no contaminants). Iron-56 Tally.	2.24480E+03	26.35

Table 32: Cobalt Foil Thermal Calculated Response Results

Case Name	Brief Case Description	Calculated Response (R) [Bq/g]	Calculated σ
Base	High Fidelity Model	7.10130E+01	0.71
DP1	SILENE and Collimator Box A only (no floor)	5.19430E+01	0.39
DP2	Same as dp1 except 40 cm thick floor now included as inscribed by boundary around SILENE and Collimator Box A	5.37480E+01	0.37
DP3	Same as dp1 except 40 cm thick floor now extends full y-dimension for reactor cell	5.54320E+01	0.43
DP4	Same as dp1 except 40 cm thick floor now extends 1/2 of x-dimension for reactor cell	5.70200E+01	0.42
DP5	Same as dp1 except 40 cm thick floor now extends full x and y dimensions of reactor cell	6.03430E+01	0.45
DP6	Same as dp1 except rear wall (+y dimension) now added	5.20050E+01	0.40
DP7	Same as dp1 except ceiling (+z dimension) now added	5.18570E+01	0.41
DP8	Same as dp1 except scattering box added	5.18140E+01	0.38
DP9	Same as dp1 except collimator box B added	5.27360E+01	0.50
DP10	Same as dp1 except Diagnostic Stand A added	5.20290E+01	0.38
DP11	Same as dp1 except Diagnostic Stand B added	5.22510E+01	0.41
DP12	Same as dp5 except rear wall (+y dimension) now added	6.29510E+01	0.54
DP13	Same as dp5 except ceiling (+z dimension) now added	Case failed to converge	
DP14	Same as dp5 except scattering box added	6.10010E+01	0.48
DP15	Same as dp5 except collimator box B added	6.14920E+01	0.51
DP16	Same as dp5 except Diagnostic Stand A added	6.10590E+01	0.54
DP17	Same as dp5 except Diagnostic Stand B added	6.09670E+01	0.46
DP18	same as dp1 except the room has been included in the global model (no door included as part of wall behind collimator box)	7.08950E+01	0.71
DP19	same as dp18 except no frame and no equipment included in collimator box (i.e. foils only)	7.09100E+01	0.74
DP20	same as dp19 except now the roof (+z dimension) has been simplified to remove concrete rail system details from global unit	7.07900E+01	0.69
Final.1	Final revised input deck based upon dp20. This run uses revised input deck but old importance map and old source mesh	7.15360E+01	0.70
Final.2	Final revised input deck based upon dp20. This run uses revised input deck, new importance map based on re-running DENOVO with final input deck and old source mesh.	7.16330E+01	0.70
Final.3	Final revised input deck based upon dp20. This run uses all new files generated using the simplified input deck (source, DENOVO and MONACO).	6.96140E+01	0.64
foilthick.up	Final revised input deck based upon dp20. Increases the thickness of all the foils 2%.	6.90120E+01	0.63
foilthick.down	Final revised input deck based upon dp20. Decreases the thickness of all the foils 2%.	7.00010E+01	0.65
foilthick.up.max	Final revised input deck based upon dp20. All foils increased thickness to max of 0.33 cm (physical problem limit) except GOLD which was increased by factor of 3 to 0.075cm.	6.00580E+01	0.53

Table 32 (Continued)

Case Name	Brief Case Description	Calculated Response (R) [Bq/g]	Calculated σ
foil.thick.down.max	Final revised input deck based upon dp20. Thickness of all foils was decreased by half.	8.11640E+01	0.76
fueliso.up	Final revised input deck based upon dp20. U-235 number density in the fuel was increased 2%.	7.06300E+01	0.70
fueliso.down	Final revised input deck based upon dp20. U-235 number density in the fuel was decreased 2%.	7.07030E+01	0.66
fueliso.up.10%	Final revised input deck based upon dp20. U-235 number density in the fuel was increased 10%.	7.02770E+01	0.69
fueliso.down.10%	Final revised input deck based upon dp20. U-235 number density in the fuel was decreased 10%.	7.30410E+01	0.74
fueliso.up.20%	Final revised input deck based upon dp20. U-235 number density in the fuel was increased 20%.	6.87410E+01	0.69
fueliso.down.20%	Final revised input deck based upon dp20. U-235 number density in the fuel was decreased 20%.	7.68310E+01	0.70
fueliso.up.25%	Final revised input deck based upon dp20. U-235 number density in the fuel was increased 25%.	6.71560E+01	0.70
fueliso.down.25%	Final revised input deck based upon dp20. U-235 number density in the fuel was decreased 25%.	7.89450E+01	0.76
poly.density.up.5%	Final revised input deck based upon dp20. Density of PPB9 was increased 5% (all number densities changed).	7.16240E+01	0.67
poly.density.down.5%	Final revised input deck based upon dp20. Density of PPB9 was decreased 5% (all number densities changed).	7.17350E+01	0.66
poly.density.up.10%	Final revised input deck based upon dp20. Density of PPB9 was increased 10% (all number densities changed).	7.18010E+01	0.70
poly.density.down.10%	Final revised input deck based upon dp20. Density of PPB9 was decreased 10% (all number densities changed).	7.17390E+01	0.64
poly.density.up.15%	Final revised input deck based upon dp20. Density of PPB9 was increased 15% (all number densities changed).	7.10180E+01	0.68
poly.density.down.15%	Final revised input deck based upon dp20. Density of PPB9 was decreased 15% (all number densities changed).	7.31030E+01	0.70
poly.density.up.25%	Final revised input deck based upon dp20. Density of PPB9 was increased 25% (all number densities changed).	7.04200E+01	0.71
poly.density.down.25%	Final revised input deck based upon dp20. Density of PPB9 was decreased 25% (all number densities changed).	7.27480E+01	0.69
poly.density.up.50%	Final revised input deck based upon dp20. Density of PPB9 was increased 50% (all number densities changed).	6.98780E+01	0.69
poly.density.down.50%	Final revised input deck based upon dp20. Density of PPB9 was decreased 50% (all number densities changed).	7.90370E+01	0.74
poly.density.up.75%	Final revised input deck based upon dp20. Density of PPB9 was increased 75% (all number densities changed).	7.08360E+01	0.68
poly.density.down.75%	Final revised input deck based upon dp20. Density of PPB9 was decreased 75% (all number densities changed).	7.72440E+01	0.73
poly.density.up.100%	Final revised input deck based upon dp20. Density of PPB9 was increased 100% (all number densities changed).	7.00040E+01	0.63
foil.pure.cobalt	Final revised input deck based upon dp20. Cobalt foil now pure cobalt - no contaminants	6.94200E+01	0.63
pure.aluminum.cobalt	Final revised input deck based upon dp20. Frame holding foils now pure aluminum (no contaminants). Cobalt Tally.	7.01250E+01	0.64

Table 33: Indium Foil Thermal Calculated Response Results

Case Name	Brief Case Description	Calculated Response (R) [Bq/g]	Calculated σ
Base	High Fidelity Model	1.1720E+07	1.19500E+05
DP1	SILENE and Collimator Box A only (no floor)	8.6431E+06	8.48500E+04
DP2	Same as dp1 except 40 cm thick floor now included as inscribed by boundary around SILENE and Collimator Box A	8.9781E+06	6.44000E+04
DP3	Same as dp1 except 40 cm thick floor now extends full y-dimension for reactor cell	9.1107E+06	6.63000E+04
DP4	Same as dp1 except 40 cm thick floor now extends 1/2 of x-dimension for reactor cell	9.4262E+06	6.94500E+04
DP5	Same as dp1 except 40 cm thick floor now extends full x and y dimensions of reactor cell	1.0129E+07	8.20000E+04
DP6	Same as dp1 except rear wall (+y dimension) now added	8.9082E+06	7.82500E+04
DP7	Same as dp1 except ceiling (+z dimension) now added	8.6645E+06	6.74500E+04
DP8	Same as dp1 except scattering box added	8.4802E+06	6.72500E+04
DP9	Same as dp1 except collimator box B added	8.6288E+06	6.81500E+04
DP10	Same as dp1 except Diagnostic Stand A added	8.5982E+06	7.03500E+04
DP11	Same as dp1 except Diagnostic Stand B added	8.6261E+06	6.53500E+04
DP12	Same as dp5 except rear wall (+y dimension) now added	1.0554E+07	1.05500E+05
DP13	Same as dp5 except ceiling (+z dimension) now added	Case failed to converge	
DP14	Same as dp5 except scattering box added	1.0149E+07	8.21500E+04
DP15	Same as dp5 except collimator box B added	1.0311E+07	9.05000E+04
DP16	Same as dp5 except Diagnostic Stand A added	1.0233E+07	8.50000E+04
DP17	Same as dp5 except Diagnostic Stand B added	1.0232E+07	9.25000E+04
DP18	same as dp1 except the room has been included in the global model (no door included as part of wall behind collimator box)	1.1447E+07	1.35000E+05
DP19	same as dp18 except no frame and no equipment included in collimator box (i.e. foils only)	1.1604E+07	1.14000E+05
DP20	same as dp19 except now the roof (+z dimension) has been simplified to remove concrete rail system details from global unit	1.1726E+07	1.17500E+05
Final.1	Final revised input deck based upon dp20. This run uses revised input deck, old importance map and old source mesh	1.1662E+07	1.13500E+05
Final.2	Final revised input deck based upon dp20. This run uses revised input deck, new importance map based on re-running DENOVO with final input deck and old source mesh.	1.1677E+07	1.14000E+05
Final.3	Final revised input deck based upon dp20. This run uses all new files generated using the simplified input deck (source, DENOVO and MONACO).	1.1708E+07	1.10000E+05
foilthick.up	Final revised input deck based upon dp20. Increases the thickness of all the foils 2%.	1.16110E+07	1.08500E+05
foilthick.down	Final revised input deck based upon dp20. Decreases the thickness of all the foils 2%.	1.17820E+07	1.09000E+05

Table 33 (Continued)

Case Name	Brief Case Description	Calculated Response (R) [Bq/g]	Calculated σ
foilthick.up.max	Final revised input deck based upon dp20. All foils increased thickness to max of 0.33 cm (physical problem limit) except GOLD which was increased by factor of 3 to 0.075cm.	6.47970E+06	5.96500E+04
foil.thick.down.max	Final revised input deck based upon dp20. Thickness of all foils was decreased by half.	1.51400E+07	1.46000E+05
fueliso.up	Final revised input deck based upon dp20. U-235 number density in the fuel was increased 2%.	1.16810E+07	1.59500E+05
fueliso.down	Final revised input deck based upon dp20. U-235 number density in the fuel was decreased 2%.	1.17170E+07	1.12000E+05
fueliso.up.10%	Final revised input deck based upon dp20. U-235 number density in the fuel was increased 10%.	1.15240E+07	1.21500E+05
fueliso.down.10%	Final revised input deck based upon dp20. U-235 number density in the fuel was decreased 10%.	1.20330E+07	1.23500E+05
fueliso.up.20%	Final revised input deck based upon dp20. U-235 number density in the fuel was increased 20%.	1.12130E+07	1.11000E+05
fueliso.down.20%	Final revised input deck based upon dp20. U-235 number density in the fuel was decreased 20%.	1.22810E+07	1.10500E+05
fueliso.up.25%	Final revised input deck based upon dp20. U-235 number density in the fuel was increased 25%.	1.10580E+07	1.11500E+05
fueliso.down.25%	Final revised input deck based upon dp20. U-235 number density in the fuel was decreased 25%.	1.23500E+07	1.14000E+05
poly.density.up.5%	Final revised input deck based upon dp20. Density of PPB9 was increased 5% (all number densities changed).	1.19100E+07	1.29000E+05
poly.density.down.5%	Final revised input deck based upon dp20. Density of PPB9 was decreased 5% (all number densities changed).	1.16270E+07	1.16000E+05
poly.density.up.10%	Final revised input deck based upon dp20. Density of PPB9 was increased 10% (all number densities changed).	1.14790E+07	1.10500E+05
poly.density.down.10%	Final revised input deck based upon dp20. Density of PPB9 was decreased 10% (all number densities changed).	1.18000E+07	1.11000E+05
poly.density.up.15%	Final revised input deck based upon dp20. Density of PPB9 was increased 15% (all number densities changed).	1.15430E+07	1.07000E+05
poly.density.down.15%	Final revised input deck based upon dp20. Density of PPB9 was decreased 15% (all number densities changed).	1.18640E+07	1.19500E+05
poly.density.up.25%	Final revised input deck based upon dp20. Density of PPB9 was increased 25% (all number densities changed).	1.13860E+07	1.10500E+05
poly.density.down.25%	Final revised input deck based upon dp20. Density of PPB9 was decreased 25% (all number densities changed).	1.16670E+07	1.12500E+05
poly.density.up.50%	Final revised input deck based upon dp20. Density of PPB9 was increased 50% (all number densities changed).	1.14630E+07	1.06000E+05
poly.density.down.50%	Final revised input deck based upon dp20. Density of PPB9 was decreased 50% (all number densities changed).	1.22630E+07	1.21500E+05

Table 33 (Continued)

Case Name	Brief Case Description	Calculated Response (R) [Bq/g]	Calculated σ
poly.density.up.75%	Final revised input deck based upon dp20. Density of PPB9 was increased 75% (all number densities changed).	1.13250E+07	1.07500E+05
poly.density.down.75%	Final revised input deck based upon dp20. Density of PPB9 was decreased 75% (all number densities changed).	1.23650E+07	1.24000E+05
poly.density.up.100%	Final revised input deck based upon dp20. Density of PPB9 was increased 100% (all number densities changed).	1.13210E+07	1.08000E+05
foil.pure.indium	Final revised input deck based upon dp20. Indium foil now pure indium - no contaminants	1.17300E+07	1.10500E+05
pure.aluminum.indium	Final revised input deck based upon dp20. Frame holding foils now pure aluminum (no contaminants). Indium Tally.	1.16210E+07	1.04500E+05

Table 34: Nickel Foil Threshold Calculated Response Results

Case Name	Brief Case Description	Calculated Response (R) [Bq/g]	Calculated σ
Base	High Fidelity Model	1.35920E+01	1.2100E-01
DP1	SILENE and Collimator Box A only (no floor)	1.28410E+01	1.0900E-01
DP2	Same as dp1 except 40 cm thick floor now included as inscribed by boundary around SILENE and Collimator Box A	1.31560E+01	1.1000E-01
DP3	Same as dp1 except 40 cm thick floor now extends full y-dimension for reactor cell	1.30720E+01	1.1000E-01
DP4	Same as dp1 except 40 cm thick floor now extends 1/2 of x-dimension for reactor cell	1.32050E+01	1.1550E-01
DP5	Same as dp1 except 40 cm thick floor now extends full x and y dimensions of reactor cell	1.33800E+01	1.1700E-01
DP12	Same as dp5 except rear wall (+y dimension) added	1.29260E+01	1.1500E-01
DP13	Same as dp5 except ceiling (+z dimension) added	1.29030E+01	1.1050E-01
DP14	Same as dp5 except scattering box added	1.28760E+01	1.1550E-01
DP15	Same as dp5 except collimator box B added	1.34010E+01	1.1800E-01
DP16	Same as dp5 except Diagnostic Stand A added	1.33240E+01	1.2050E-01
DP16A	Same as dp16 except run with a different random number	7.40210E+03	1.2150E-01
Final.1	Final revised input deck based upon dp20. This run uses revised input deck, old importance map and old source mesh	1.33190E+01	1.2050E-01
Final.2	Final revised input deck based upon dp20. This run uses revised input deck, new importance map based on re-running DENOVO with final input deck and old source mesh.	1.33160E+01	1.2050E-01
Final.3	Final revised input deck based upon dp20. This run uses all new files generated using the simplified input deck (source, DENOVO and MONACO).	1.33250E+01	1.2050E-01
foilthick.up	Direct perturbation of final input (final.test3). Foil thickness increased 2%	1.33220E+01	1.2000E-01
foilthick.down	Direct perturbation of final input (final.test3). Foil thickness decreased 2%	1.33490E+01	1.2100E-01
foilthick.up.max	Direct perturbation of final input (final.test3). Foil thickness increased to problem's physical max of 0.33 cm.	1.32200E+01	1.1850E-01
fueliso.up	Direct perturbation of final input (final.test3). Number density of U-235 in fuel increased by 2%.	1.33760E+01	1.2200E-01
fueliso.down	Direct perturbation of final input (final.test3). Number density of U-235 in fuel decreased by 2%.	1.33060E+01	1.2000E-01
fueliso.up.10%	Direct perturbation of final input (final.test3). Number density of U-235 in fuel increased by 10%	1.32330E+01	1.2100E-01
fueliso.down.10%	Direct perturbation of final input (final.test3). Number density of U-235 in fuel decreased by 10%.	1.30410E+01	1.2000E-01
poly.density.up.5%	Direct perturbation of final input (final.test3). Density of PPB9 increased by 5% (all number densities changed).	1.33470E+01	1.2000E-01
poly.density.down.5%	Direct perturbation of final input (final.test3). PPB(density decreased 5% (all number densities changed).	1.34060E+01	1.2000E-01

Table 35: Iron-54 Foil Threshold Calculated Response Results

Case Name	Brief Case Description	Calculated Response (R) [Bq/g]	Calculated σ
Base	High Fidelity Model	2.0415E-01	1.935E-03
DP1	SILENE and Collimator Box A only (no floor)	1.9763E-01	1.790E-03
DP2	Same as dp1 except 40 cm thick floor now included as inscribed by boundary around SILENE & Collimator Box A	1.9624E-01	1.790E-03
DP3	Same as dp1 except 40 cm thick floor now extends full y-dimension for reactor cell	1.9612E-01	1.790E-03
DP4	Same as dp1 except 40 cm thick floor now extends 1/2 of x-dimension for reactor cell	1.9917E-01	1.800E-03
DP5	Same as dp1 except 40 cm thick floor now extends full x and y dimensions of reactor cell	2.0064E-01	1.825E-03
DP12	Same as dp1 except the frame for Collimator Box A has been removed from the model	1.9565E-01	1.780E-03
DP13	Same as dp1 except the equipment interior to Collimator Box A has been removed from the model	1.9905E-01	1.815E-03
DP14	Combines cases dp12 and dp13 so that only the collimator box & foils inside the aluminum frame are modeled with SILENE	1.9587E-01	1.795E-03
DP15	Same as dp14 except the floor is now included in global unit	2.0134E-01	1.860E-03
DP16	Same as dp1 except now the entire room is included in the global unit (walls, no door behind coll box and simplified ceiling) NOTE THAT THIS IS THE SAME GEOMETRY AS IS USED IN P1THERM.DP20.INP	2.0418E-01	1.900E-03
DP16A	Same as dp16 except run with a different random number	2.0115E-01	1.890E-03
Final.1	Final revised input deck based upon dp20. This run uses revised input deck, old importance map and old source mesh	2.0417E-01	1.900E-03
Final.2	Final revised input deck based upon dp20. This run uses revised input deck, new importance map based on re-running DENOVO with final input deck & old source mesh.	2.0417E-01	1.900E-03
Final.3	Final revised input deck based upon dp20. This run uses all new files generated using the simplified input deck (source, DENOVO and MONACO).	2.0394E-01	1.895E-03
foilthick.up	Direct perturbation of final input (final.test3). Foil thickness increased 2%	2.0393E-01	1.895E-03
foilthick.down	Direct perturbation of final input (final.test3). Foil thickness decreased 2%	2.0401E-01	1.895E-03
foilthick.up.max	Direct perturbation of final input (final.test3). Foil thickness increased to problem's physical max of 0.33 cm.	2.0390E-01	1.910E-03
fueliso.up	Direct perturbation of final input (final.test3). Number density of U-235 in fuel increased by 2%.	2.0259E-01	1.915E-03
fueliso.down	Direct perturbation of final input (final.test3). Number density of U-235 in fuel decreased by 2%.	2.0441E-01	1.910E-03
fueliso.up.10%	Direct perturbation of final input (final.test3). Number density of U-235 in fuel increased by 10%	2.0275E-01	1.920E-03
fueliso.down.10%	Direct perturbation of final input (final.test3). Number density of U-235 in fuel decreased by 10%.	2.0296E-01	1.935E-03
poly.density.up.5%	Direct perturbation of final input (final.test3). Density of PPB9 increased by 5% (all number densities changed).	2.0367E-01	1.915E-03
poly.density.down.5%	Direct perturbation of final input (final.test3). PPB(density decreased 5% (all number densities changed).	2.0532E-01	1.9200E-03

Table 36: Iron-56 Foil Threshold Calculated Response Results

Case Name	Brief Case Description	Calculated Response (R) [Bq/g]	Calculated σ
Base	High Fidelity Model	1.20300E+02	1.3950
DP1	SILENE and Collimator Box A only (no floor)	1.18210E+02	1.3150
DP2	Same as dp1 except 40 cm thick floor now included as inscribed by boundary around SILENE & Collimator Box A	1.19090E+02	1.3650
DP3	Same as dp1 except 40 cm thick floor now extends full y-dimension for reactor cell	1.18090E+02	1.3000
DP4	Same as dp1 except 40 cm thick floor now extends 1/2 of x-dimension for reactor cell	1.18690E+02	1.3400
DP5	Same as dp1 except 40 cm thick floor now extends full x and y dimensions of reactor cell	1.20380E+02	1.3550
DP12	Same as dp1 except the frame for Collimator Box A has been removed from the model	1.18170E+02	1.3500
DP13	Same as dp1 except the equipment interior to Collimator Box A has been removed from the model	1.18410E+02	1.3300
DP14	Combines cases dp12 and dp13 so that only the collimator box and foils inside the aluminum frame are modeled with SILENE	1.18170E+02	1.3450
DP15	Same as dp14 except floor is now included in the global unit	1.19600E+02	1.3550
DP16	Same as dp1 except now the entire room is included in the global unit (walls, no door behind coll box and simplified ceiling) NOTE THAT THIS IS THE SAME GEOMETRY AS IS USED IN P1THERM.DP20.INP	1.21220E+02	1.3450
DP16A	Same as dp16 except run with a different random number	1.19760E+02	1.3550
Final.1	Final revised input deck based upon dp20. This run uses revised input deck, old importance map and old source mesh	1.21240E+02	1.3450
Final.2	Final revised input deck based upon dp20. This run uses revised input deck, new importance map based on re-running DENOVO with final input deck and old source mesh.	1.21230E+02	1.3450
Final.3	Final revised input deck based upon dp20. This run uses all new files generated using the simplified input deck (source, DENOVO and MONACO).	1.22570E+02	1.3750
foilthick.up	Direct perturbation of final input (final.test3). Foil thickness increased 2%	1.22550E+02	1.3700
foilthick.down	Direct perturbation of final input (final.test3). Foil thickness decreased 2%	1.22470E+02	1.3700
foilthick.up.max	Direct perturbation of final input (final.test3). Foil thickness increased to problem's physical max of 0.33 cm.	1.22600E+02	1.3800
fueliso.up	Direct perturbation of final input (final.test3). Number density of U-235 in fuel increased by 2%.	1.20760E+02	1.3550
fueliso.down	Direct perturbation of final input (final.test3). Number density of U-235 in fuel decreased by 2%.	1.20970E+02	1.3600
fueliso.up.10%	Direct perturbation of final input (final.test3). Number density of U-235 in fuel increased by 10%	1.20020E+02	1.3850
fueliso.down.10%	Direct perturbation of final input (final.test3). Number density of U-235 in fuel decreased by 10%.	1.20230E+02	1.3900
poly.density.up.5%	Direct perturbation of final input (final.test3). Density of PPB9 increased by 5% (all number densities changed).	1.21810E+02	1.4100
poly.density.down.5%	Direct perturbation of final input (final.test3). PPB(density decreased 5% (all number densities changed).	1.23550E+02	1.4050

Table 37: Magnesium Foil Threshold Calculated Response Results

Case Name	Brief Case Description	Calculated Response (R) [Bq/g]	Calculated σ
Base	High Fidelity Model	6.67800E+01	7.0950E-01
DP1	SILENE and Collimator Box A only (no floor)	6.62870E+01	7.0650E-01
DP2	Same as dp1 except 40 cm thick floor included as inscribed by boundary around SILENE & Collimator Box A	6.74110E+01	7.1150E-01
DP3	Same as dp1 except 40 cm thick floor now extends full y-dimension for reactor cell	6.62090E+01	6.9900E-01
DP4	Same as dp1 except 40 cm thick floor now extends 1/2 of x-dimension for reactor cell	6.56100E+01	6.9650E-01
DP5	Same as dp1 except 40 cm thick floor now extends full x and y dimensions of reactor cell	6.78110E+01	7.1250E-01
DP12	Same as dp1 except the frame for Collimator Box A has been removed from the model	6.48450E+01	6.9150E-01
DP13	Same as dp1 except the equipment interior to Collimator Box A has been removed from the model	6.64520E+01	7.1100E-01
DP14	Combines cases dp12 and dp13 so that only the collimator box and foils inside the aluminum frame are modeled with SILENE	6.51750E+01	6.9350E-01
DP15	Same as dp14 except floor now included in the global unit	6.82980E+01	7.0100E-01
DP16	Same as dp1 except now the entire room is included in the global unit (walls, no door behind coll box and simplified ceiling) NOTE THAT THIS IS THE SAME GEOMETRY AS IS USED IN P1THERM.DP20.INP	6.58950E+01	6.8400E-01
DP16A	Same as dp16 except run with a different random number	6.71490E+01	6.9800E-01
Final.1	Final revised input deck based upon dp20. This run uses revised input deck, old importance map & old source mesh	6.59100E+01	6.8350E-01
Final.2	Final revised input deck based upon dp20. This run uses revised input deck, new importance map based on re-running DENOVO with final input deck & old source mesh.	6.59100E+01	6.8400E-01
Final.3	Final revised input deck based upon dp20. This run uses all new files generated using the simplified input deck (source, DENOVO and MONACO).	6.61340E+01	6.8400E-01
foilthick.up	Direct perturbation of final input (final.test3). Foil thickness increased 2%	6.60960E+01	6.8500E-01
foilthick.down	Direct perturbation of final input (final.test3). Foil thickness decreased 2%	6.60770E+01	6.8300E-01
foilthick.up.max	Direct perturbation of final input (final.test3). Foil thickness increased to problem's physical max of 0.33 cm.	6.60460E+01	6.8350E-01
fueliso.up	Direct perturbation of final input (final.test3). Number density of U-235 in fuel increased by 2%.	6.75200E+01	6.9150E-01
fueliso.down	Direct perturbation of final input (final.test3). Number density of U-235 in fuel decreased by 2%.	6.62230E+01	6.8400E-01
fueliso.up.10%	Direct perturbation of final input (final.test3). Number density of U-235 in fuel increased by 10%	6.73040E+01	7.0150E-01
fueliso.down.10%	Direct perturbation of final input (final.test3). Number density of U-235 in fuel decreased by 10%.	6.69600E+01	6.9550E-01
poly.density.up.5%	Direct perturbation of final input (final.test3). Density of PPB9 increased by 5% (all number densities changed).	6.67030E+01	6.8700E-01
poly.density.down.5%	Direct perturbation of final input (final.test3). PPB(density decreased 5% (all number densities changed).	6.66000E+01	6.9250E-01

Table 38: Indium Foil Threshold Calculated Response Results

Case Name	Brief Case Description	Calculated Response (R) [Bq/g]	Calculated σ
Base	High Fidelity Model	7.59200E+03	8.8000E+01
DP1	SILENE and Collimator Box A only (no floor)	7.06140E+03	7.3150E+01
DP2	Same as dp1 except 40 cm thick floor now included as inscribed by boundary around SILENE & Collimator Box A	7.17740E+03	7.3200E+01
DP3	Same as dp1 except 40 cm thick floor now extends full y-dimension for reactor cell	7.12600E+03	7.2450E+01
DP4	Same as dp1 except 40 cm thick floor now extends 1/2 of x-dimension for reactor cell	7.23430E+03	7.6150E+01
DP5	Same as dp1 except 40 cm thick floor now extends full x and y dimensions of reactor cell	7.42070E+03	7.9950E+01
DP12	Same as dp1 except the frame for Collimator Box A has been removed from the model	7.04500E+03	7.2550E+01
DP13	Same as dp1 except the equipment interior to Collimator Box A has been removed from the model	7.02130E+03	7.1400E+01
DP14	Combines cases dp12 and dp13 so that only the collimator box and foils inside the aluminum frame are modeled with SILENE	6.99300E+03	7.2350E+01
DP15	Same as dp14 except floor is now included in the global unit	7.36000E+03	8.0150E+01
DP16	Same as dp1 except now the entire room is included in the global unit (walls, no door behind coll box and simplified ceiling) NOTE THAT THIS IS THE SAME GEOMETRY AS IS USED IN P1THERM.DP20.INP	7.20420E+03	7.8500E+01
DP16A	Same as dp16 except run with a different random number	7.40210E+03	8.2850E+01
Final.1	Final revised input deck based upon dp20. This run uses revised input deck, old importance map & old source mesh	7.21250E+03	7.8650E+01
Final.2	Final revised input deck based upon dp20. This run uses revised input deck, new importance map based on re-running DENOVO with final input deck & old source mesh.	7.21290E+03	7.8650E+01
Final.3	Final revised input deck based upon dp20. This run uses all new files generated using the simplified input deck (source, DENOVO and MONACO).	7.21840E+03	7.9300E+01
foilthick.up	Direct perturbation of final input (final.test3). Foil thickness increased 2%	7.21480E+03	7.8950E+01
foilthick.down	Direct perturbation of final input (final.test3). Foil thickness decreased 2%	7.22310E+03	7.9950E+01
foilthick.up.max	Direct perturbation of final input (final.test3). Foil thickness increased to problem's physical max of 0.33 cm.	7.19620E+03	7.8500E+01
fueliso.up	Direct perturbation of final input (final.test3). Number density of U-235 in fuel increased by 2%.	7.35080E+03	8.6350E+01
fueliso.down	Direct perturbation of final input (final.test3). Number density of U-235 in fuel decreased by 2%.	7.29900E+03	8.0300E+01
fueliso.up.10%	Direct perturbation of final input (final.test3). Number density of U-235 in fuel increased by 10%	7.26640E+03	8.2650E+01
fueliso.down.10%	Direct perturbation of final input (final.test3). Number density of U-235 in fuel decreased by 10%.	7.28950E+03	8.1150E+01
poly.density.up.5%	Direct perturbation of final input (final.test3). Density of PPB9 increased by 5% (all number densities changed).	7.25200E+03	8.1250E+01
poly.density.down.5%	Direct perturbation of final input (final.test3). PPB(density decreased 5% (all number densities changed).	7.25330E+03	8.0800E+01

Appendix C

The uncertainties listed below all come from the French technical report on the experimental setup. (Piot, June 2011) The uncertainties studied as part of this dissertation have already been identified in Section 5.3. The remaining uncertainties may be examined as part of future modeling efforts. However, it is worth noting that the uncertainties not studied are all likely not to produce model sensitivities due their either being so small or due to their not impacting the activation foils directly (or both).

FUEL ISOTOPICS
234-U 0.5891 atom % ± 0.0010
235-U 92.6857 atom % ± 0.0200
236-U 0.2519 atom % ± 0.0010
238-U 6.4733 atom % ± 0.0050

FUEL CONCENTRATION
70.36 g/l ± 0.05 g/l

FUEL DENSITY
1.15624 g/cm^3 ± 0.00003 g/cm^3

DIMENSIONS ON CONCRETE SHIELDS
(z) Height = 103.0 cm ± 0.5 cm
Width = 103.0 cm ± 0.5 cm
Thickness = 20.0 cm ± 0.5 cm
Concrete width = 100.0 cm ± 0.5 cm

MASS OF CONCRETE SHIELD
Standard concrete = 535 kg ± 1 kg
Magnetite concrete = 845.5 kg ± 1 kg
Baryte concrete = 806.0 kg ± 1 kg

POSITION OF FOILS ON PLATE IN SCATTERING BOX
In both the vertical and horizontal directions the center to center spacing of the foils is reported as 2.5 cm ± 1 cm

LOCATION OF SILENE IN REACTOR CELL
Looking down on the room:
11.32 m from the West Wall
7.77 m from the East Wall
5.87 m from the South Wall
6.24 m from the North Wall

All dimensions are given in meters with an uncertainty of ±0.01 m

COMPOSITION OF Z3-CN.1810 STEEL
Ni 9.0 – 11.0 w/o
Cr 17.0 – 19.0 w/o
C 0.03 w/o MAX
Mn 2.0 w/o MAX
Fe will also be uncertain since it is specified as "balance" (i.e. add the w/o values of all the given constituents, subtract it from 100 w/o and assign the value as the Fe w/o.)

COMPOSTION OF A42 STEEL
C 0.18 – 0.25 w/o
P 0.040 – 0.075 w/o
S 0.040 – 0.062 w/o
N 0.007 – 0.009 w/o
Fe will have uncertainty due it being specified as "balance".

SIZE OF GAPS BETWEEN SHIELD BLOCKS IN THE SCATTERING BOX
(see figures on pp 42-43 of the French Source Document for details)
There is no reported uncertainty on the measurement of the gaps themselves. However, the size of the gaps does vary from the bottom to the top of the concrete shield blocks. The modeling assumption being made is that the gaps are uniform.

HEIGHT OF SCATTERING BOX PANELS ABOVE THE FLOOR
H= 728 mm (min) to 736 mm (max)
Again – there is no uncertainty given to the measured value of height only a range within which this number varies depending on WHERE it was measured.

HEIGHT OF COLLIMATOR BOX A FROM THE FLOOR
H= 723 mm (min) to 730 mm (max)

HEIGHT OF COLLIMATOR BOX B FROM THE FLOOR
H= 723 mm (min) to 730 mm (max)

COMPOSTION OF ALUMINUM FOR FOIL FRAMES
Mg 2.6 – 3.6 w/o
Cr < 0.3 w/o
Ti < 0.15 w/o
Zn < 0.2 w/o
Mn < 0.5 w/o
Cu < 0.1 w/o
Si < 0.4 w/o
Fe < 0.4 w/o
Aluminum will also be "uncertain" since it has been specified as "balance". Once again note that there are no uncertainties given on the actual measurements of weight percent only a range within which the measured value may vary.

COMPOSTION OF Al2O3 POWDER FOR CEA TLD

Mass = 432 mg ± 30 mg (2σ)

Volume = 214 mm^3

This is the only time an uncertainty value has been reported as 2-sigma. I am assuming in the absence of a statement like this that all uncertainties are reported as 1-sigma.

COMPOSTION OF ALUMINUM ALLOY FOR CEA TLD FRAME

Mg 0.4 – 1.0 w/o
Mn 0.3 – 0.8 w/o
Cu 3.5 – 3.7 w/o
Si 0.3 – 0.8 w/o
Cr ≤ 0.1 w/o
Ti + Zr ≤0.2 w/o
Zn ≤ 0.2 w/o
Fe ≤ 0.5 w/o

The Al w/o value will be uncertain as well since it has been specified as "balance".

COMPOSTION OF PPB9

There is 1.29 w/o of this material listed as "other" with no details on what the actual materials are. The model herein assumes that this unknown is not in the model and the remaining constituent w/o values are re-normalized to 100w/o.

COMPOSTION OF S235JR STEEL

C ≤ 0.17 w/o
Mn ≤ 1.4 w/o
P ≤ 0.035 w/o
S ≤ 0.035 w/o
N ≤ 0.012 w/o
Cu ≤ 0.55 w/o

Fe will also vary and be uncertain due to its being specified as "balance".

COMPOSTION OF BARYTE CONCRETE MIXTURE FOR CONCRETE SHIELDS

Cl ≤ 0.01 w/o
B < 0.1 w/o

Remainder of the material is assumed to be Oxygen and so it will vary due to it being specified as "balance.

DIMENSIONS OF ACTIVATION FOILS

Gold: Thickness = 0.25 mm ± 10.0%; Diameter = 20.0 mm ± 0.2 mm
Nickel: Thickness = 2.0 mm ± 10.0%; Diameter = 20.0 mm ± 0.5 mm
Indium: Thickness = 1.0 mm ± 10.0%; Diameter = 20.0 mm ± 0.5 mm
Iron: Thickness = 3.0 mm ± 10.0%; Diameter = 20.0 mm ± 0.5 mm
Magnesium: Thickness = 2.0 mm ± 10.0%; Diameter = 20.0 mm ± 0.5 mm
Cobalt: Thickness = 2.0 mm ± 10.0%; Diameter = 20.0 mm ± 0.2 mm

MASS OF ACTIVATION FOILS

Gold: M = ± 0.2%
Nickel: M = ± 0.2%
Indium: M = ± 0.2%
Iron: M = ± 0.2%
Magnesium: M = ± 0.2%
Cobalt: M = ± 0.2%

VITA

Kevin Reynolds was born in Manhattan, Kansas to Roger and Victoria Reynolds. He has one younger brother John and one younger sister Kathryn. Kevin moved to Mississippi at an early age when his father got a teaching job at Mississippi State University in Starkville. Kevin graduated from Warren Central High School in Vicksburg, Mississippi. After graduation he attended Mississippi State University and received his bachelor of Science Degree in Nuclear Engineering with a Minor in Mathematics. After receiving his bachelor's degree, Kevin continued his education by attending The University of Tennessee at Knoxville. Kevin graduated with a Master of Science Degree in Nuclear Engineering in 1990 and went on to serve in the United States Navy for 3 years. Kevin began his professional career after his military service in Denver, Colorado where he worked as a Nuclear Criticality Safety Engineer for 2 years. In 1995 Kevin moved back to Tennessee and continued his work as a Nuclear Criticality Safety Engineer for the U.S. Department of Energy at the Y-12 National Security Complex where he is currently employed. He was granted a sabbatical from his job to attend the University of Tennessee at Knoxville to complete his education. Kevin graduated from the University of Tennessee with a Doctor of Philosophy degree in Nuclear Engineering in May 2013 and returned to work at Y-12.